9-19-2019

An Experimental Investigation of Tank Pressure Oscillations during Filling with a Bi-Stable Load Switched Supersonic Fluidic Oscillator

Chris Peirone
University of Windsor

An Experimental Investigation of Tank Pressure Oscillations during Filling

with a Bi-Stable Load Switched Supersonic Fluidic Oscillator

by

Chris Peirone

A Thesis
Submitted to the Faculty of Graduate Studies
through the Department of
Mechanical, Automotive and Materials Engineering
in Partial Fulfillment of the Requirements for
the Degree of Master of Applied Science
at the University of Windsor

Windsor, Ontario, Canada

2019

An Experimental Investigation of Tank Pressure Oscillations during Filling

with a Bi-Stable Load Switched Supersonic Fluidic Oscillator

By:
Chris Peirone

APPROVED BY:

_____

D. Green
Department of Mechanical Automotive and Materials Engineering

_____

O. Jianu
Department of Mechanical Automotive and Materials Engineering

_____

G. Rankin, Advisor
Department of Mechanical Automotive and Materials Engineering

Sept 19, 2019

Declaration of Originality

I hereby certify that I am the sole author of this thesis and that no part of this thesis has been published or submitted for publication.

I certify that, to the best of my knowledge, my thesis does not infringe upon anyone's copyright nor violate any proprietary rights and that any ideas, techniques, quotations, or any other material from the work of other people included in my thesis, published or otherwise, are fully acknowledged in accordance with the standard referencing practices. Furthermore, to the extent that I have included copyrighted material that surpasses the bounds of fair dealing within the meaning of the Canada Copyright Act.

I declare that this is a true copy of my thesis, including any final revisions, as approved by my thesis committee and the Graduate Studies office, and that this thesis has not been submitted for a higher degree to any other University or Institution.

Abstract

Preliminary testing shows that providing pressure pulsations during the super plastic forming process has proven to increase the total elongation of the material and is thus, likely to improve product design flexibility. A bi-stable load switched supersonic fluidic oscillator is the preferred device used to promote these pressure fluctuations during the superplastic forming process due to the absence of moving mechanical parts and resulting reliability. This thesis includes the design, construction and use of a supersonic fluidic oscillator. This apparatus can be used to validate available numerical results and identify any consistent trends over a range of operating conditions. The results of interest in this experiment are the forming pressure fluctuation amplitudes and frequencies during the filling of a chamber similar to that found in the superplastic forming process. The experimental results agree with the numerical results in trends, however, are significantly different regarding the magnitudes. Consistent trends in the relationships between dimensionless variables are shown to exist over a range of operating conditions.

Dedication

I would like to dedicate this thesis to my parents, Terri and Joseph Peirone who have always believed in me and have inspired me to succeed. The positive upbringing and support that they have provided me with is a big part in making this possible and will never go unappreciated.

Furthermore, I would like to dedicate this work to my supervising professor, Dr. Gary Rankin, for his patience and guidance during my academic study. It has been a great experience working under a professor as knowledgeable a prestigious as Dr. Rankin.

Acknowledgements

I would first like to thank Dr. Gary Rankin, for his support and continued involvement throughout this project.

I would also like to thank the industrial partners, Mr. Eugene Ryzer and Mr. Sam Leong from AEM Power Systems. Their guidance, insight, support and contributions in conjunction with an Ontario Centers of Excellence VIP II grant has made the designing and procurement of the necessary equipment and materials to make this test facility possible and are greatly appreciated.

I would like to thank my committee members; Dr. Ofelia Jianu and Dr. Daniel Green for their guidance during my thesis proposal which helped me foresee important aspects which needed to be included in my thesis.

Furthermore, I would like to thank the following individuals for their contributions throughout my research: Andrew Jenner for his guidance and procurement of materials, Bruce Durfy for water-jetting the gasket, Kevin Harkai for machining the SFO blocks, Ramadan Barakat for everything electrical, Sichang Xu for passing down his valuable knowledge and Lovepreet Singh Sidhu for his numeral results.

I'd also like to thank Mr. Brandon Sookram for encouraging me to further my education.

Thank you all very much. Without your contributions, this experiment would not have been a success.

Table of Contents

List of Figures

List of Tables

Nomenclature

T_o	Absolute total temperature; $K, {}^\circ\mathrm{C}$
P_b	Back pressure; $kPa\ (psig)$
A^*	Critical throat area for C-D nozzle; m^2
f_c	Cut-off frequency; Hz
τ_c	Discharge time constant; s
T_m	Fluid medium temperature (absolute); K
f	Frequency; Hz
f_{Fb}	Frequency in the feedback tanks; Hz
f_{EC}	Frequency in the SPF chambers; Hz
R	Gas constant; $J/kg \cdot K$
f_{HC}	High cut-off frequency; Hz
Ma	Mach number
$\dot{m}$	Mass flow rate; kg/s
Fb_{mean}	Mean feedback tank pressures; kPa
P_r	Non-dimensional back pressure
$\wp_{Fb}$	Non-dimensional feedback tank amplitudes
$\mathcal{F}$	Non-dimensional frequency
$\overline{\wp}_{Fb}$	Non-dimensional mean feedback pressure
$\overline{\wp}_{EC}$	Non-dimensional mean SPF chamber pressure
$\wp_{amp}$	Non-dimensional SPF chamber pressure amplitudes
$\mathcal{T}$	Non-dimensional time
β	Leak constant; s^{-1}
f_{LC}	Low cut-off frequency; Hz
P	Pressure; kPa (psig)
∇P	Pressure gradient; kPa (psig)
γ	Ratio of specific heats
a	Sonic speed; m/s
P_{amp}	SPF chamber pressure amplitudes; Pa
T_{EC}	SPF chamber temperatures; ${}^\circ\mathrm{C}$

α_s	Splitter angle; °
$\dot{\gamma}$	Strain rate; s^{-1}
P_s	Supply pressure; kPa (psig)
T_s	Supply temperature; K
t_s	Switching time; s
A_t	Throat area; m^2
τ_c	Time constant; s
t_t	Transmission time; s
v	Velocity; m/s
V_{EC}	Volume of SPF chambers; m^3
V_{FB}	Volume of feedback tanks; m^3
V_{SFO}	Volume of the SFO; m^3

Chapter 1: Introduction

1.1: Motivation

The motivation of this work is to investigate the use of fluidics to improve the superplastic forming process (SPF). Superplastic forming is a process in which a gas, usually air, is used to apply a continuous load on a thin sheet of metal that is heated to relatively high temperatures; approximately 450℃ for aluminum [1]. These high temperatures allow the material to be deformed to levels of strain that would otherwise cause ruptures of the sheet. Nevertheless, significant limits remain in the strain rate capabilities of these materials, even at these elevated temperatures. Due to the strain rate limitations, cycle times for forming are relatively high which result in low to medium production rates [1]. The SPF process compared to other forming processes such as press-forming, produce more complex shaped products. These intricate shapes often lead to quality issues. In an attempt to reduce production time and increase product quality, research into introducing pressure fluctuations in the air during the SPF process has not only revealed attractive preliminary test results in regard to increasing the formability capabilities of these materials, but is also expected to lead to higher quality parts [2]. Figure 1.1 (a) is a schematic diagram of the SPF process setup while a graph of the chamber pressure increase during the SPF filling process without fluctuations is given in Figure 1.1 (b) and with pressure fluctuations in Figure 1.1 (c).

Conventional devices for generating pressure fluctuations, such as rotary valves, are not reliable in extreme environmental conditions due to the presence of moving mechanical parts and seals. A more robust device is necessary to produce these pressure fluctuations during the SPF process. Fluidic devices provide accurate flow control and

oscillations for a steady input flow without the use of moving mechanical components [3] making them ideal devices to produce pressure fluctuations during the SPF process.
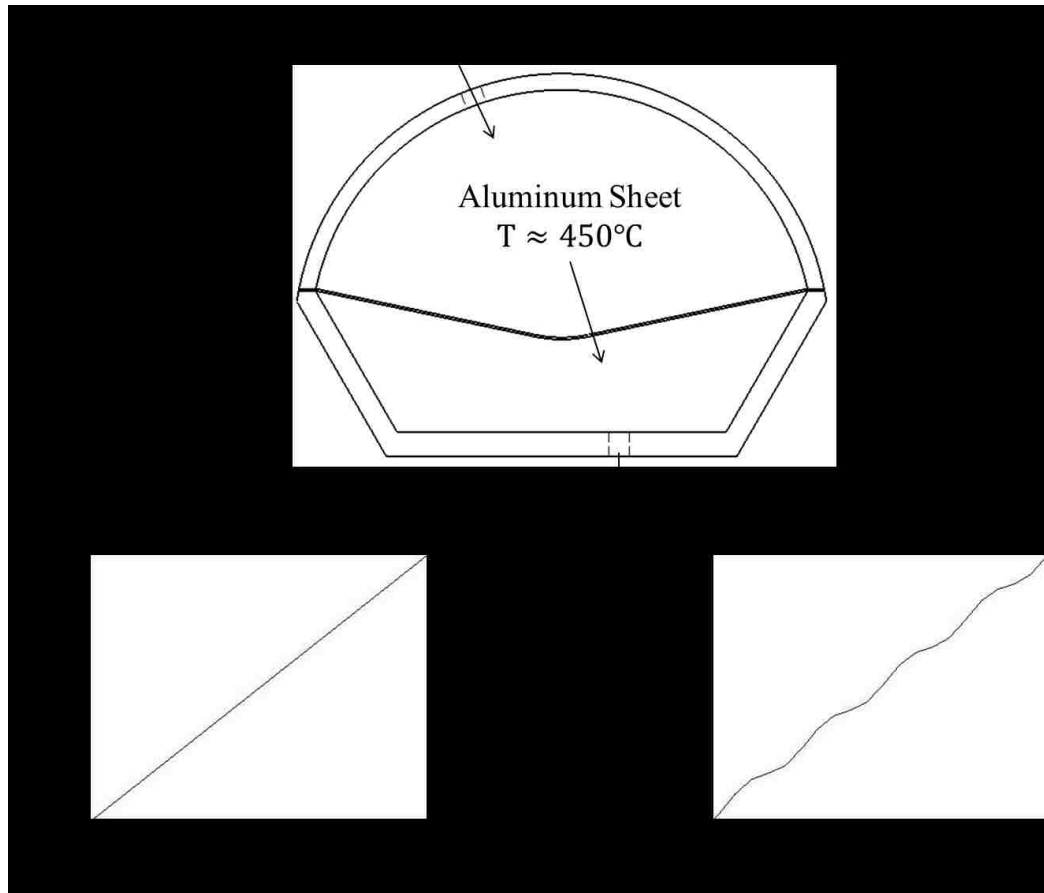
Figure 1.1: SPF process (a) without (b) and with (c) pressure fluctuations

1.2: Fluidic Devices

In 1959, a group of scientists at the U.S Army Harry Diamond Laboratories discovered fluidics, the first devices being fluid amplifiers [3]. One of their first applications was, for safety reasons, the replacement of electronic devices for controlling the pneumatic components used in the production of armaments involving explosives. They soon were being used in other applications to replace electronic devices but the advent of transistors and integrated electronic circuits proved superior in most control

system applications. The use of these devices eventually reached its peak in the mid-1960s. Since the 1970's, extensive research has led to the realization of the true benefits of these devices in specialized applications [3]. Recently, fluidic devices utilizing gasses or liquids as the working fluid, have found numerous applications at the micro-level in drug administration and lab-on-a-chip devices [4]. Bi-stable Fluidic Oscillators are fluidic devices which provide oscillatory flow outputs for steady flow inputs. One class of oscillator makes use of a jet wall-attachment phenomenon known as the Coanda Effect; in addition to several types of flow switching mechanisms

1.3: Wall-Attachment Theory (Coanda Effect):

A fluidic switch, shown in Figure 1.2, contains a jet nozzle (converging-diverging section at bottom), in addition to a splitter which separates the flow into two channels. Under certain steady input flow conditions, the jet exiting the nozzle attaches itself to one of the two channels due to a phenomenon known as the Coanda Effect.
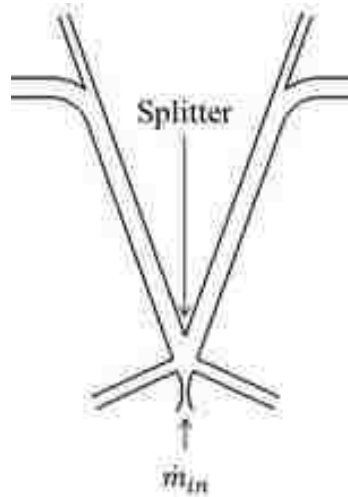
Figure 1.2: Sketch of a fluidic oscillator

The Coanda Effect occurs when a jet flow exits a nozzle and, the high velocity flow interacts with surrounding stagnant ambient fluid molecules as shown in Figure 1.3.

Due to viscous effects, the surrounding fluid is made to follow a similar path [5]; this is known as flow entrainment shown as dashed lines.
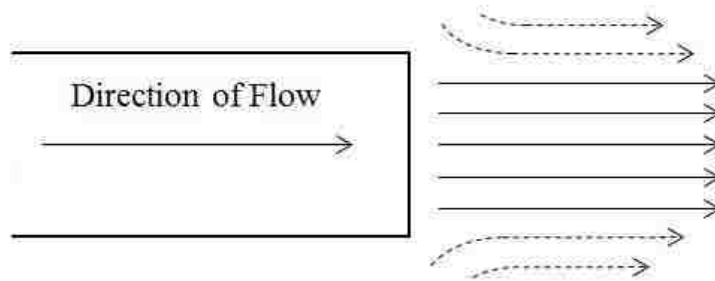
Figure 1.3: Flow entrainment of a jet exiting a nozzle

When a wall is introduced on one side near the exiting jet flow, it restricts the flow entrainment which creates a low (vacuum) pressure region as some mass is removed without being replaced by entrainment. The side of the flow without a wall does not experience a lower pressure and therefore the flow attaches to the nearby wall [5], as shown in Figure 1.4. The location downstream where the jet flow reattaches to the wall is dependent on the proximity of the wall as well as the exiting jet velocity. Even if the wall is at an angle relative to the jet flow direction or curved, the wall-attachment can still occur [5]. If two walls are present and symmetrically located with respect to the axis of the exiting jet flow, the jet will attach to one of the two walls since the jet is not in stable equilibrium when equally divided between the two channels and small changes in either the flow or geometry triggers the instability. Once the flow is attached to one of the two channels, without the presence of a switching mechanism, the flow will remain attached to that channel.
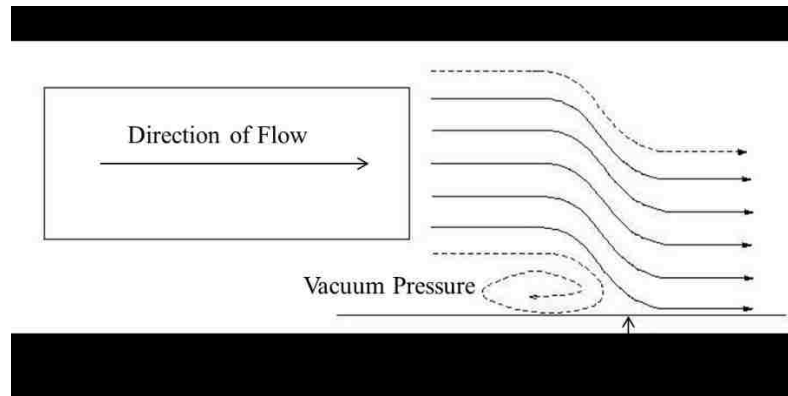
Figure 1.4: Jet flow attaching to a nearby wall due to the Coanda Effect

1.4: Switching Mechanisms

For the fluidic device shown in Figure 1.2 to operate as an oscillator, a switching mechanism must exist to move the flow from the attached channel side to the opposite channel and back, continuously repeating. Three possible types of switching mechanism are: (1) momentum switching, (2) pressure (recirculation) switching and (3) load switching.

1.4.1: The Momentum Switching Mechanism

Figure 1.5 shows a fluidic oscillator in which, due to the Coanda Effect, the main jet flow is attached to the bottom channel, shown as a dotted line in the channel. In this figure, the flow travelling through the bottom channel enters a flow dividing region in which some of the flow enters the straight narrow channel and the remainder enters the curved channel. If a direct path exists for the flow exiting through the curved channel to pass into the control channel, noted by returning mass flow rate, the returned mass flow rate in the control channel impinges on the main jet flow and the momentum causes the main jet to switch to the upper channel. This is known as momentum switching and requires that the returning mass flow rate must have a sufficiently high momentum.
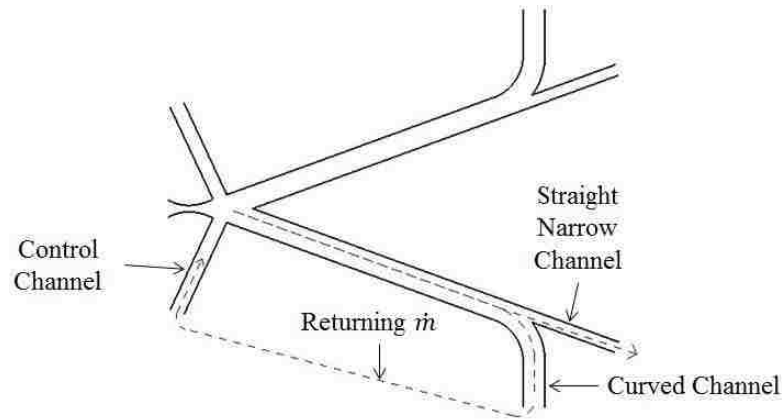
Figure 1.5: Momentum switching

1.4.2: The Pressure (Recirculation) Switching Mechanism

This switching mechanism is similar to the momentum switching in that it also involves the returning mass flow rate to the control channel. In this case, the returning flow has a lower momentum. Figure 1.6 shows the returning mass flow rate in the control channel in addition to a recirculation region, which is present just upstream of the wall attachment location. This returning mass flow rate does not have a high enough momentum to directly impinge on the jet flow however, the flow feeds the recirculation region providing the flow needed for entrainment on the wall side of the jet and increasing the pressure, which causes the jet to bend less towards the wall resulting in a growth of the recirculation region. A further increase eventually causes the jet to switch to the upper channel. The same series of events occurs on the opposite side and this process repeats over and over causing oscillation.
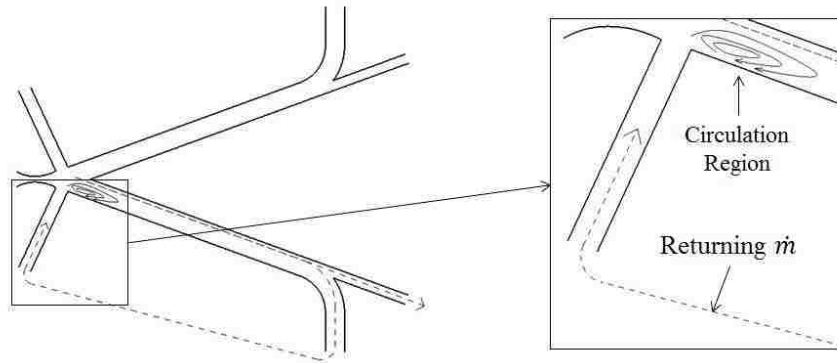
Figure 1.6: Recirculation switching

1.4.3: The Load Switching Mechanism

The load switching mechanism does not require a return path for the mass flow rate like the two previous switching mechanisms. Figure 1.7 shows a similar profile to the device shown in Figure 1.2 however, in this case, there are tanks, referred to as feedback tanks, at the exit of the straight narrow channel [6]. As the flow travels through the straight narrow path, the tanks fill which results in an increase in pressure that propagates upstream towards the jet exit. When the pressure at the splitter tip reaches a sufficiently high value, the jet switches to the upper channel. This process then repeats with the upper feedback tank, causing oscillation.
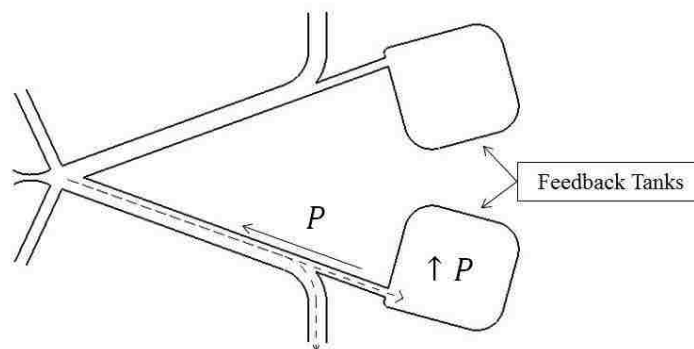
Figure 1.7: Load switching

Since the 1970's, extensive research has provided a great deal of information regarding how these fluidic oscillators behave in regards to their type [3], as well as their geometries and scaling. The following chapter discusses important findings of the research.

Chapter 2: Literature Review and Research Objectives

The literature discussed in this thesis is selected due to its relevance to the current experimental investigation and hence is restricted to experimental studies in the following two areas:

- Sonic and subsonic fluidic oscillators

- Supersonic fluidic oscillators.

The chapter concludes with a description of the objectives of the current research

2.1: Subsonic and sonic fluidic oscillators

Bobusch et al. [7] conducted an experimental investigation of the internal flow characteristics of a feedback loop type oscillator with a mixing chamber using water as the working fluid. A sketch of Bobusch's experimental oscillator is shown in Figure 2.1 to provide further explanation of how this device operates.
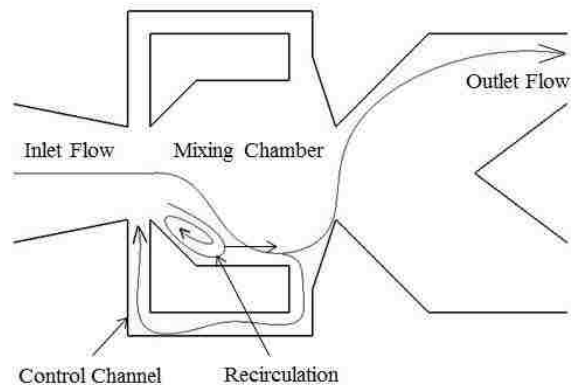
Figure 2.1: Sketch of Bobusch's oscillator

As the inlet flow attaches to the lower surface of the mixing chamber due to the Coanda Effect, a recirculation region develops just upstream of the attachment location. A portion of the flow splits and is fed back through the control channel and impinges on the

recirculation region causing it to grow and propagate downstream. The effect of this is that flow separating from the bottom surface is then forced to the upper surface of the mixing chamber and attaches to the upper surface due to the Coanda Effect. The portion of flow which does not return through the feedback channel is directed to the outlet, as shown in Figure 2.1. This switching mechanism is similar to the pressure switching case discussed in Chapter 1.3.2. Likely due to the low velocities of the water, momentum switching is not considered to be the main mechanism promoting oscillation. Further investigation, using a higher velocity inlet, may show the momentum playing a larger role in switching [7]. Bobusch's interest is the frequency of oscillation in relation to the Reynolds number. The results of this experiment revealed a direct linear relationship of the frequency of oscillation versus the Reynolds number in the turbulent, incompressible flow regime.

Raghu [8] published a paper which focused on fluidic oscillators with feedback channels (feedback type oscillators). Similar to the device shown in Figure 2.1, the oscillator uses a converging nozzle, a mixing chamber, two feedback channels and two diverging output nozzles. The oscillator behaves similar to the one Bobusch et al. investigated. Similar to Guyot et al. [9] and Gregory et al. [10], who found that the oscillation frequency is independent of the fluid's incompressibility, they noticed a linear relationship with the flow rates (Reynolds Number) and frequency, like Bobusch's findings. Raghu noted that Gregory et al. [10] had studied these trends in a device operating in the incompressible flow regime and further investigated the trends in the compressible flow regime. Raghu investigated meso-scale oscillators (supply nozzle sizes ranging from 200μm to 1mm) and studied oscillation frequency changes with geometric

scaling. It was found that for low mass flow rates in the order of 1 g/s, the frequency of

oscillations for these devices is in the range of 1 kHz to 10 kHz [8,10]. Raghu

investigated the effect of supply pressure on oscillator frequency for an oscillator with a

1mm size nozzle. A linear relationship between the supply pressure and frequency is

observed, but only in the incompressible flow regime. The trend is non-linear beyond that

range and shows a decrease in the rate of increase in frequency with supply pressure. It is

concluded that the frequency of oscillation is more sensitive to supply pressure in the

incompressible flow regime. Raghu [8] also studied the effect of geometric scaling on the

oscillation frequency using three scaling factors: 1.0, 1.5 and 2.0. Although it was noted

that these comparisons did not consist of exact scaling aspect ratios due to slightly

different geometries, it was concluded that for these feedback type oscillators, upscaling

by a factor of 2 resulted in an overall decrease in frequency by a factor of 4 [8].

Simoes et al. [11] conducted an experimental study of a "microfluidic oscillator

for gas flow control and measurement". A feedback loop oscillator was studied, similar to

the one in Figure 2.1 with a few major differences. Figure 2.2 provides a sketch of his

oscillator to identify these differences. The region in which the feedback flow enters the

interaction region is converging, causing an acceleration of the flow prior to interacting

with the main jet. This oscillator also contains a splitter, located between the inlet and

outlets of the feedback loop, similar to the one in Figure 1.2. It was found that the time

for the jet to move from one channel to the other consists of two values: the transmission

time (t_t) and the switching time (t_s) and hence, the frequency of oscillation for gases is

given by Equation 1.

$$f \approx \frac{1}{2(t_t + t_s)} \tag{1}$$

The transmission time is a function of the feedback loop length over the wave speed propagating in the feedback loop and the switching time is directly proportional to the length between the nozzle and the splitter, labelled L in Figure 2.2, divided by the jet velocity. Since the transmission time depends on the wave propagation speed in the feedback loop relative to the main jet velocity in the interaction region, this is the smallest term for liquids since the velocities are much lower than the wave propagation speed and is neglected. However, for gases, the main jet flow velocity can be large compared to the wave propagating through the feedback loop and the transmission time is a significant factor [11].
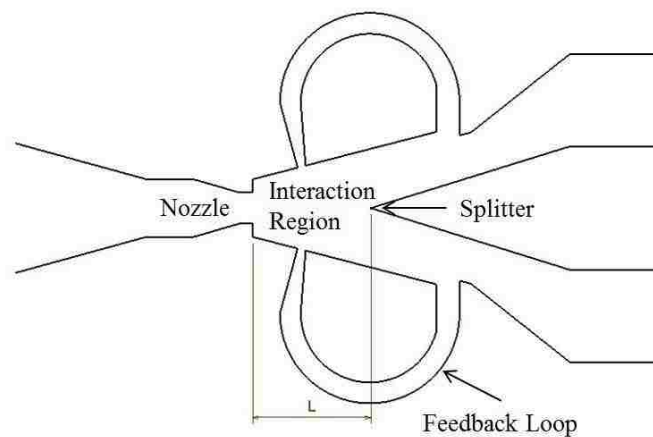
Figure 2.2: Sketch of Simoes' oscillator

Simoes investigated the effects of the feedback loop length on the overall oscillation frequency for three different gases: Nitrogen (N_2), Argon (Ar) and Carbon Dioxide (CO_2). In all cases of feedback loop lengths, N_2 experiences the highest frequency, Ar the second highest and CO_2 the minimum frequency, as expected. The study also concludes that the smaller (shorter) the feedback loop, the higher the frequency, which is in agreement with Raghu [8].

2.2: Supersonic fluidic oscillators (SFO)

A supersonic oscillator requires a converging-diverging inlet nozzle to achieve supersonic flow in the interaction region [12].

R.V Thompson et al. [13] conducted an extensive study of the effects of geometry on the performance of bi-stable load switched supersonic fluidic oscillators. Figure 2.3 provides a definition of the geometric parameters that Thompson investigated: the splitter angle (α_s), the control channel width (W_c), control channel location (CCL), main channel length (MCL) as well as the position of the splitter in relation to the throat location (L_s). Locations for both the attached and unattached sides of the jet, the reattachment location and its distance from the nozzle throat (L_{rl}) is shown in Figure 2.4.
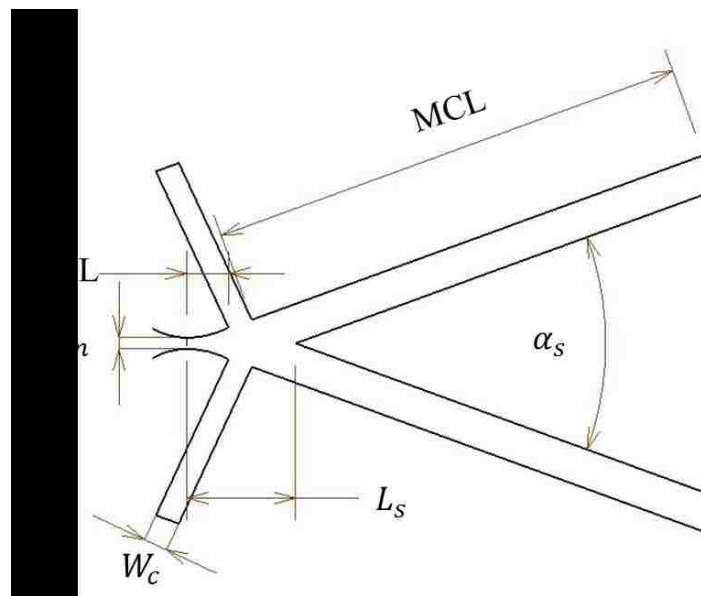
Figure 2.3: Geometric parameters investigated by Thompson et al. [13]
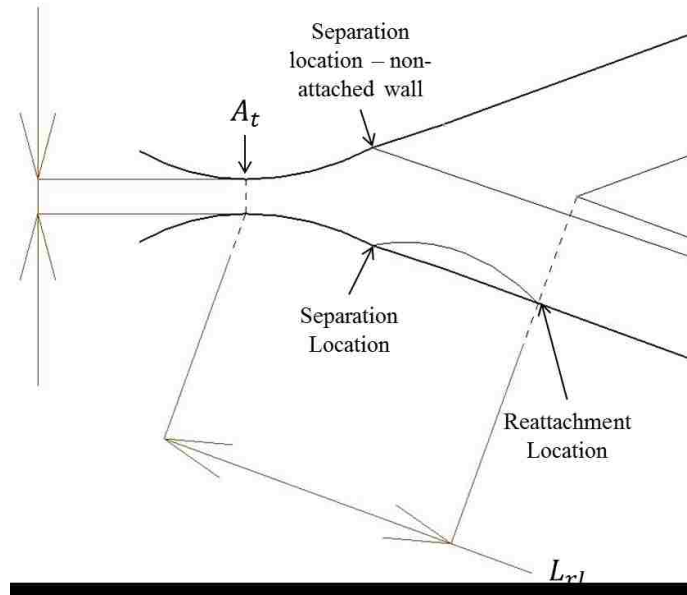
Figure 2.4: Flow features investigated by Thompson et al. [13]

The most important findings of Thompson's research may be summarized as follows:

1. A splitter angle of 40º is found to be optimum in that it produces the minimum adverse pressure gradient in the attached boundary layer on the outer side walls resulting in the greatest stability of the reattachment point.

2. The reattachment length is found to be independent of the splitter angle and dependent on the non-dimensional back pressure $\left(P_b/P_s\right)$ and the throat area (A_t).

3. Qualitatively, the channel length must exceed 20% of the reattachment distance to provide stable jet attachment.

4. The control channel must be positioned between the flow separation and the reattachment locations of the jet; the exact location seemed to have little effect on the performance of oscillations.

5. A minimum control channel width of 0.085 inches (aspect ratio of 8.8) must be attained to allow for switching.

14

6. The minimum location of the splitter is downstream from the separation location in which the flow is reattached for the highest supply pressure.

7. Flow visualization indicated that the separated flow on the non-attached wall may be assumed to travel parallel to the attached wall side.

8. Provided the main channel width is greater than the perpendicular distance of the non-attached wall separated flow and the attached wall, the splitter will not interact with the main jet flow.

Hiroki et al. [14] adopted the design criteria developed by Thompson et al. [13] and conducted both analytical and experimental investigations of the oscillation frequencies from a bi-stable load switched supersonic fluidic oscillator for the application of material fatigue testing. Figure 2.5 shows the design of Hiroki's experimental device.
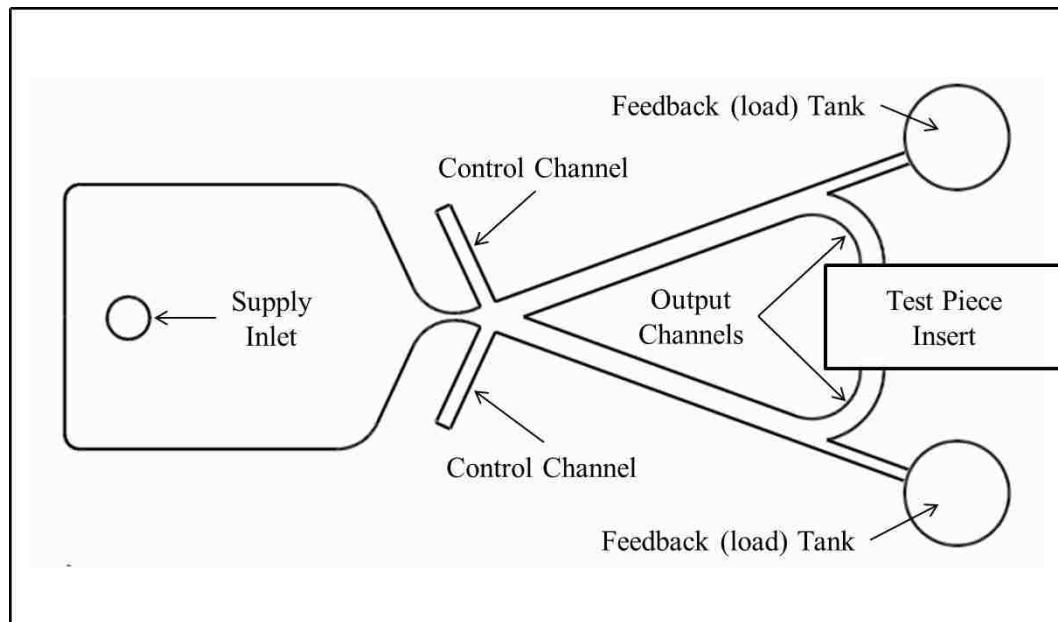
Figure 2.5: Top-view sketch of Hiroki's Oscillator [14]

Hiroki's design consists of a supply inlet, a converging-diverging nozzle to achieve supersonic flow in the interaction region, two main control channels, a flow splitter, two output channels directed inwards to the test piece insert port and two

feedback tanks which promote load switching. Hiroki placed a thin metal piece in the test

piece insert port and conducted bending fatigue tests based on the load and frequency

supplied by the output channels onto the test piece. Pressure measurements are obtained

for the supply pressure, control channel pressure and the feedback tank pressure. In

addition to the fatigue bending tests, Hiroki is also interested in the oscillation frequency

for various operating conditions. Important findings are that for the control channels fully

open (orifice size at its maximum) the oscillation frequency increased as the supply

pressure increased. Furthermore, as the supply pressure is increased, the peak pressure in

the feedback tanks also increases (load for switching increases with supply pressure). It is

also found that increasing the feedback tank volumes decreases the frequency for a given

supply pressure. This is logical since a larger tank volume corresponds to a longer filling

time and thus, a lower frequency.

Xu [15] implemented Hiroki's design but included an exhaust chamber in order to

determine the range of back pressure to supply pressure (back pressure ratios) which give

oscillations. Figure 2.6 is a dimensioned sketch of Xu's experimental oscillator with the

addition of an exhaust chamber; all dimensions presented are in mm [15].
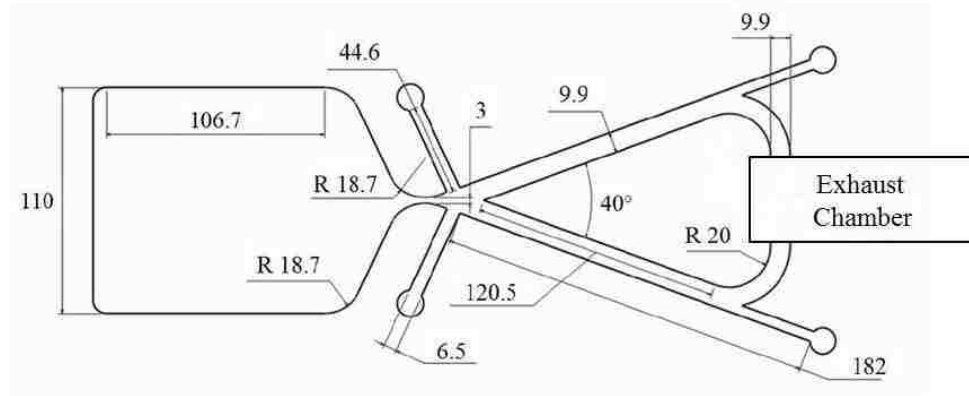
Figure 2.6: Dimensioned sketch of Xu's oscillator

Xu studied the effects that various operating conditions have on oscillation frequencies and oscillation pressure amplitudes in the single exhaust chamber and in both feedback tanks. Xu also determined the peak feedback tank pressures required to permit load switching for a given supply pressure. He obtained results from pressure transducers located in the supply chamber, the control channels, the feedback tanks and the exhaust chamber. Xu also used the Schlieren technique for flow visualization in order to capture shockwaves in the oscillator. These results are used to validate numerical results obtained using a 2-D oscillator and 0-D (lumped parameter) model for the feedback tanks and the exhaust chamber. Xu found that, for a constant exhaust control channel resistance (fixed orifice), the oscillation frequency increased with supply pressure which agrees with the results of Hiroki et al. [6]. He also found the useable oscillation range for a given supply pressure while varying the chamber pressure (back pressure). For a given supply pressure, the range of useable oscillation is defined by a minimum and maximum back pressure that provides stable oscillation, referred to the lower and upper limits of oscillation, respectively. An important finding of this paper is that the frequency of oscillation decreases as the average exhaust chamber pressure increases for a constant

supply pressure. Also, as the oscillation frequency decreases, the oscillation pressure amplitudes increase in the exhaust chamber. For a given supply pressure, there is a range of back pressures which provide stable oscillations; beyond this range an unstable oscillation or no oscillation occurs at all. If the supply pressure is too high, the large momentum of the main jet flow prevents the Coanda Effect from causing the flow to attach to a nearby wall and the main jet flow splits evenly between the two main channels. If the supply pressure is too low, the flow attaches itself to one of the two channels and remains there without switching. As the supply pressure is increased within the range of useful oscillation, the oscillation frequency increases.

2.3: Objectives of this Research

The objectives of this research are to:

1) Design, build and instrument a high pressure Supersonic Fluidic Oscillator (SFO)/Superplastic Forming (SPF) chamber experimental flow facility.

2) Conduct experiments using the facility mentioned in 1) over a wide range of supply pressure values to:

   a) Determine SFO facility performance data including pressure oscillation amplitudes and frequency as well as the variation of mean pressures and temperatures during the SPF chamber filling process for the case of an SFO simultaneously filling two separate super plastic forming chambers.

   b) Provide data necessary to validate the 2D-0D, 2D-3D numerical model of the facility operation.

   c) Identify consistent trends in the oscillation frequencies and amplitudes during the SPF chamber filling process.

Chapter 3: Experimental Setup

This chapter includes details of the design of the current SFO and a description of how it differs from the previous SFO design. The selection of the valves, fittings and devices used for sensing the pressures and temperatures are also described. Considerations regarding the instrument locations are presented and finally, the data acquisition system and LabVIEW program are described.

3.1: SFO Design and Modifications

Figure 3.1 (a) shows the original SFO design studied by Xu for application to the SPF process while Figure 3.1 (b) is the current version including modifications which, conceptually, are more ideal for the SPF process.
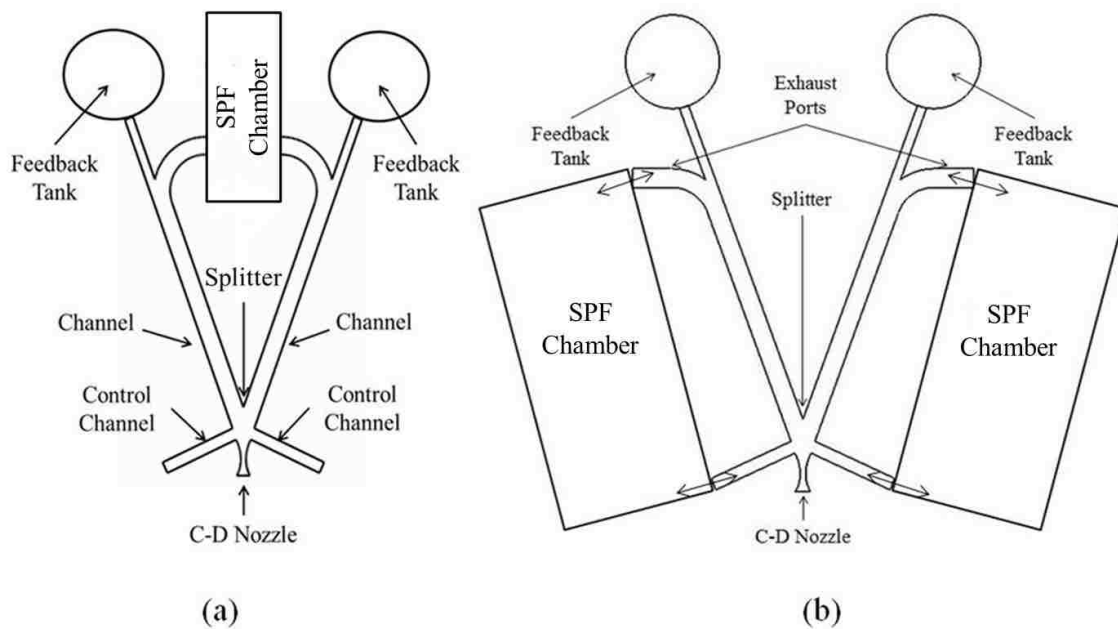
Figure 3.1: (a) Xu's oscillator and (b) new oscillator design

The SPF exhaust channels are directed outward instead of inward to allow filling of two SPF chambers instead of one. The main benefits of using two SPF chambers are: (1)

pressure amplitudes will increase due to the elimination of the pulsations from the two outputs being out of phase and partially cancelling out and (2) two SPF processes occur simultaneously, which increases the manufacturing production rate.

The SPF process involves the production of relatively large parts and hence SPF lengths are scaled by a factor of 3. A dimensioned sketch of the SFO is shown in Figure 3.2. All dimensions are in millimeters and the uniform thickness of the profile is 3.2 mm giving a throat cross-sectional area of $A_t = 3.2 \ mm^2$.

Figure 3.2: Dimensioned Sketch of SFO

By introducing this 1/3 scale, it is possible to non-dimensionally represent relatively large SPF chambers in relation to the size of the SFO using minimal laboratory space. The experiments however, are only an approximation to the real process as they are run at room temperature with constant volume SPF chambers, whereas the actual SPF process runs at high temperatures ($T \approx 450°C$) with varying volumes due to the deformation of the sheet metal during the SPF filling process.

The actual experimental design consists of two 6061 - T6 aluminum blocks with an overall thickness of 101.4 mm (4 inches) machined using a CNC machine which are fastened together to provide a closed system. Figure 3.3 shows the faces of the two blocks that are mounted together.
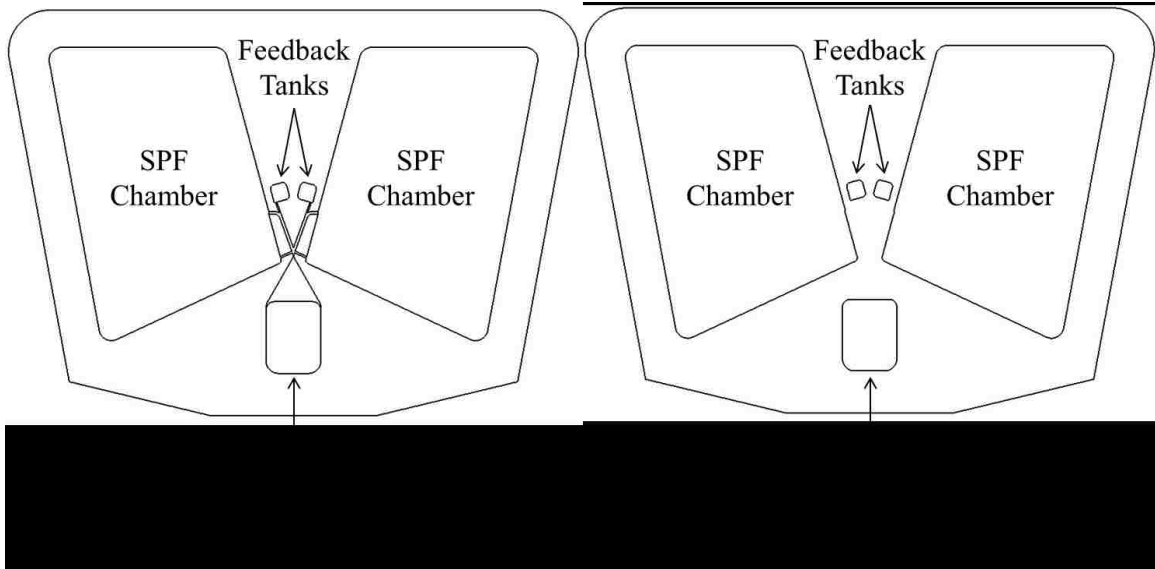
Figure 3.3: CAD files showing face views of the (a) top block and (b) bottom block

Both blocks include feedback tanks, SPF chambers and supply inlet tanks. The profile of the SFO is machined only on the top block, shown in Figure 3.3 (a), in addition to a converging section used to guide the flow into the converging-diverging nozzle from the supply chamber. The volume of the feedback tanks (V_{FB}) and SPF chambers (V_{EC}) are 22 cm^3 ($2.2x10^{-5}$ m^3) and 8 liters ($8x10^{-3}$ m^3), respectively. For symmetry in the depth dimension, the feedback tanks and SPF chambers have machined depths that are 3.2 mm greater than the ones in the bottom block. It is important to note that the volume of the feedback tanks is much smaller than the volume of the SPF chambers so that the SPF chamber capacities do not have a significant influence on the frequencies of oscillation.

The volume of the feedback tanks provides control of the frequency and amplitude of the pressure fluctuations during the SPF filling process. The two blocks are fastened together using 131, 3/8-16 4 ¾" UNC grade 8 bolts, torqued to 24.3 N-m (215 lb-in), with thru clearance holes as shown in Figure 3.4 (a) and 3/8-16x1" threads tapped in the block, shown in Figure 3.4 (b). The minimum wall thickness in the 6061 T6 aluminum is the thickness of the SPF chambers, 43.07 mm (1.696 in). The calculations performed to ensure a conservative design safety factor for the bolts and wall thickness are provided in Appendix A.1 and Appendix A.2. The two aluminum blocks are sealed together using an Oil-Resistant Aramid/Buna-N Gasket that is pre-compressed to a thickness of 0.397 mm (1/64") [16]. The gasket is pre-cut using a waterjet cutting machine with the edges of the gasket overlapping the profile shown in Figure 3.4 (a) and then trimmed to size with an X-ACTO® knife to match the profile. Also shown in the figure are two 8 mm dowel holes drilled in both blocks used for locating as well as six large bores to reduce the mass of the experimental blocks.
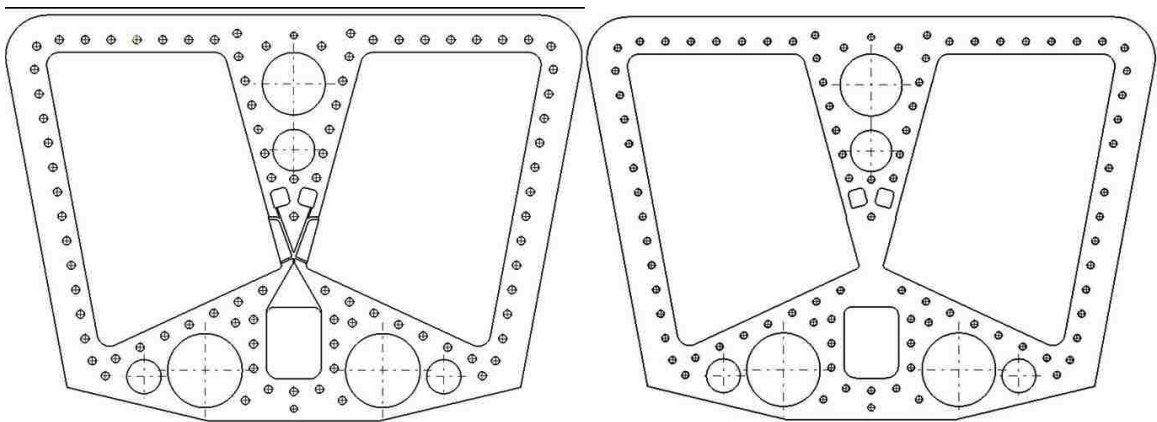
Figure 3.4: CAD views of SFO faces with the addition of bolt holes used for mounting

3.2: Selection of Measurement Devices

The measurements of interest during the SPF filling process are the supply pressure (P_s) and the variation with time, over the duration of the SPF chamber filling process of the following quantities: mean pressure in the feedback tanks (Fb_{mean}), the fluctuating pressure amplitudes in the feedback tanks (P_{FB}), the pulsation frequency measured in the feedback tanks (f_{Fb}), the mean SPF chamber pressure (P_b) and fluctuating pressure amplitudes (P_{amp}) and the frequencies measured in the SPF chambers (f_{EC}). The supply temperature (T_s) as well as the variation with time of the SPF chamber temperatures (T_{EC}) during the filling process are also measured to determine the temperature change during filling.

A 2-D/lumped parameter ANSYS Fluent CFD model [17], has been used to provide insight regarding the pressure fluctuation amplitudes and frequencies expected over the ranges of supply pressures and back pressures considered. The predicted SPF chamber pressure fluctuation amplitudes are in the range 137.9 Pa (0.02 psi) $\leq P_{amp} \leq$ 5171 Pa (0.75 psi). This information is used to select the devices to measure the pressure.

3.2.1: Selection of Pressure Measuring Devices

Since the supply pressure of interest has a maximum value of 3.971 MPa gauge (576 psig), a PX409-1.0kG5V-XL OMEGA™ piezoresistive pressure transducer is selected to measure the supply pressure. This pressure transducer has a 0-5V output reading, a full-scale pressure reading of 9.895 MPa (1000 psig) and a 0.03% full scale reading linearity [18]. In addition, it has an overall accuracy of 0.05% full scale reading and 0.08% repeatability. This also provides sufficient accuracy for capturing the pressure

fluctuation amplitudes and frequencies in the feedback tanks which are expected to be in the range $34\ kPa\ (5\ psi)\ \leq\ P_{Fb} \leq 310\ kPa\ (45\ psi)$ based on the CFD solution.

For a given supply pressure, the ranges of backpressure that provide stable oscillations have also been predicted in order to aid in the pressure transducer selection. For a maximum supply pressure of 3.971 MPa gauge (576 psig) the upper range of back pressure that is predicted for stable oscillation is approximately 1.724 MPa (250 psig). Based on this, it is decided to limit the maximum pressure in the SPF chambers to 3.103 MPa gauge (450 psig) using two PRV9434 PINK 450 PSI pressure relief valves. One relief valve is placed in each SPF chamber. The calculations made regarding the selection of this device are shown in Appendix A.3.

Since the expected maximum SPF pressure is 3.103 MPa gauge (450 psig), two PX409-500G5V-XL piezoresistive pressure transducers are selected to measure the transient SPF chamber pressures (P_b). Even with the high accuracy linearity option of 0.03%, the accuracy is still insufficient for measuring the expected low-pressure fluctuation amplitudes in the SPF chambers, based on the CFD model prediction. Additional devices are necessary for capturing the low-pressure fluctuation amplitudes expected in the SPF chambers.

The transducers in the supply pressure chamber and the SPF chambers are assembled with thru holes that are 37/64" in diameter with ¼ - 18 NPT tap threads that are 15.88 mm (5/8") in length. To avoid significantly increasing the volumes in the feedback tanks, 3.18 mm (1/8") diameter channels separate the two transducers from the feedback tanks, as shown in the auxiliary view in Figure 3.5. This figure shows all the relevant dimensions and a gap between the bottom face of the transducer and the bottom

of the bored surface that is 5.1 mm in length with a diameter of approximately 14.64 mm. This gap introduces a small volume between the channel and the transducer. In addition to the channel diameter of 3.18 mm, the figure also shows the channel length of 54.9 mm. It is important to show that the pressure fluctuation amplitude readings obtained from the pressure transducers in the feedback tanks are not altered by the filtering action caused by the channel and volume. This is shown in Appendix A.4. With a natural frequency calculated to be 646 Hz, the amplitudes measured are 0.15% greater than the true amplitudes for a frequency of 25Hz and for a frequency of 100 Hz, the amplitudes measured are 2.5% greater than the actual values.
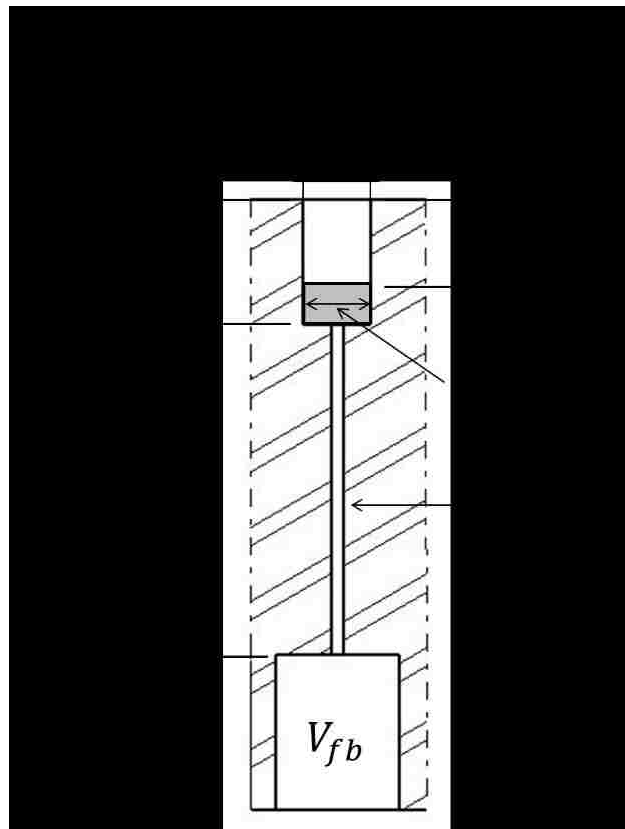
Figure 3.5: Non-flush mounted piezoresistive pressure transducers located in the feedback tanks

One PCB® 113B28 ICP® piezoelectric pressure sensor is selected to measure the pressure fluctuation amplitude in each of the SPF chambers. These pressure sensors do not sense steady increases in pressure (a characteristic of the piezoelectric crystals) and hence, are used only to measure dynamic pressure changes. The pressure sensors are connected to a PCB® 482C15 buffered signal conditioner with gain options of x1, x10 and x100 [19]. This signal conditioner - sensor system acts as a high-pass filter with a discharge time constant dependent on the sensor's time constant provided by the manufacturer's calibration data sheet [20]. The discharge time constant (τ_c), for both PCB 113B28 sensors used is 2.3 seconds. This time constant results in a low cut-off frequency $f_{LC} = 0.069\ Hz$ since

$$f_c = \frac{1}{2\pi\tau_c} \tag{5}$$

A 100 kΩ resistor is connected from the (+) terminal to ground to reduce noise fluctuations [21]. Since the frequencies of interest are $25\ Hz\ \leq f\ \leq 100\ Hz$, two model 477A03 plug-in low pass filters are used to eliminate any unwanted high frequency noise and turbulent pressure fluctuations prior to the signal reaching the A/D converter. These filters plug directly into the PCB® 482C15 signal conditioner. The filters selected have a high cut-off frequency $f_{Hc} = 500\ Hz$ at the -3dB cut-off point with cut-off slopes of -20 dB/decade. The buffered signal conditioner contains an isolation operational amplifier that isolates (buffers) the low and high pass filter in each channel. The result is an active band pass filter. Figure 3.6 qualitatively illustrates the measurement errors due to the filter [22].
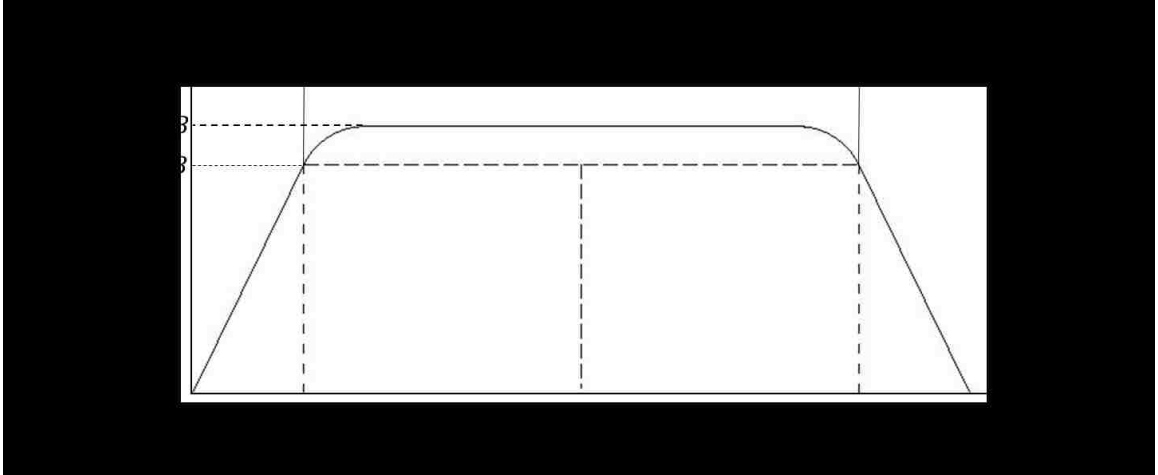
Figure 3.6: Transfer function of an active band pass filter

The signal losses due to the active band pass filter are dependent on the frequency measured. If the frequency measured is in the range $f_{LC} \leq f \leq (f_{LC} + f_{HC})/2$, Equation 6 is used and for $(f_{LC} + f_{HC})/2 \leq f \leq f_{HC}$, Equation 7 is used [22]. Since the expected maximum frequency is 100 Hz, Equation 6 is expected to be used for all cases. For the frequency range of 25 Hz to 100 Hz, the ratio of P_{out} over P_{in} range is approximately 0.9999 for all ranges using the low cut-off frequency of 0.069 Hz.

$$P_{out} = P_{in} \frac{\frac{f}{f_{LC}}}{\sqrt{1 + \left(\frac{f}{f_{LC}}\right)^2}} \tag{6}$$

$$P_{out} = P_{in} \frac{1}{\sqrt{\left(\frac{f}{f_{HC}}\right)^2 + 1}} \tag{7}$$

Figure 3.7 shows details of how the sensors are mounted onto the SFO's SPF chambers. There is a channel that has a diameter of 3 mm and a length of 24 mm. Unlike the piezoresistive pressure transducer mountied in the feedback tanks, there is negligible gap volume between the end of the channel and the face of the pressure sensor. This mounting acts as a closed end tube that exhibits a resonant frequency. As determined in

27

Appendix A.5, the fundamental frequency is 3648 Hz [23]. Since this frequency is much greater than the frequencies of interest, resonance effects will not occur and the arrangement is acceptable for capturing the oscillation frequencies of interest.
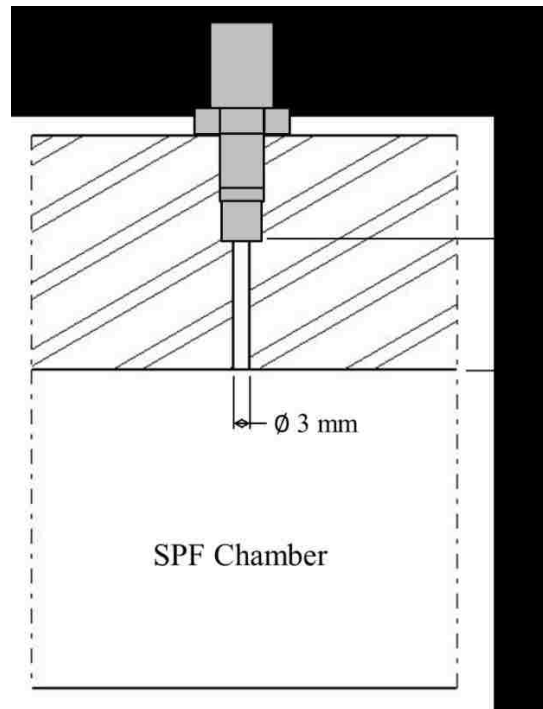
Figure 3.7: Non-flush mounting of PCB pressure sensors in the SPF chambers

3.2.2: Selection of Temperature Measuring Devices

Miniature T-Type thermocouples are used to measure the temperatures in the two SPF chambers and the supply pressure tank because of their accuracy in the temperature range of interest. The part number of these OMEGA_TM thermocouples is TMQSS-125E-6. The thermocouples have an accuracy of +/- 0.5 ºC [24,25] and have exposed junctions that are ideal for fast response times [26]. With a bare sheath diameter of 0.03", the time constant (τ_c) is approximately 1.7 seconds in air [27]. Further explanation of how the time constant is obtained is presented in Appendix A.6.

3.3: Location of Sensors and other Components Connected to the SFO/SPF Chamber Test Facility

Careful attention must be given to the placement of these sensors at locations that will capture the true values of interest and not be influenced by the inlets and exits. A 3-D numerical model, developed by Sidhu [17] is used to simulate the pressure filling in the SPF chambers and the feedback tanks. The feedback tank and SPF chamber wall pressure distributions from this solution are used to determine suitable locations. Figures 3.8 and 3.9 are CAD files that identify the locations in which the measuring devices and other important components are placed in the supply block and pressure block of the SFO, respectively.
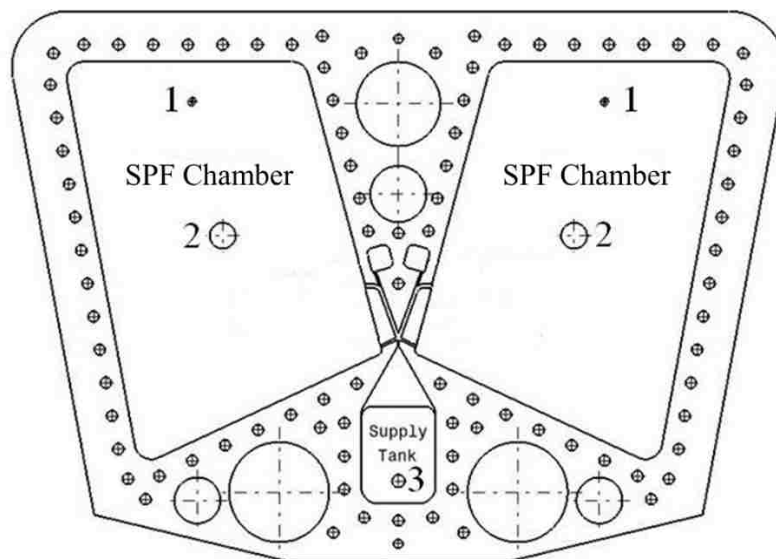
Figure 3.8: Supply block with the location of measuring devices

The locations labeled "1" in Figure 3.8 are the positions of the PCB® 113B28 piezoelectric pressure sensors. These locations are chosen to ensure that the jet flow exiting the exhaust channels does not affect the results. The "2" labels indicate the locations of the 2-position 2-way, normally open, pilot-operated, spring-returned

directional control valves. The location labelled "3" in Figure 3.8 represents the position where the N_2 enters the system, hence the title "Supply Block".

Labels "1" in Figure 3.9 are the locations of the piezoresistive pressure transducers used to measure the mean pressures in the SPF chambers. They are in the same positions as the piezoelectric pressure sensors only on the opposite block. Locations labelled "2" are the positions of the T-Type thermocouples used to measure the temperatures in the SPF chambers. The locations labelled "3" are the positions of the pressure relief valves used to limit the maximum pressure in the SPF chambers to 3.103 MPa gauge (450 psig), for safety reasons. Locations labelled "4" are where the piezoresistive pressure transducers used to measure the feedback tank pressure are located. Locations "5" and "6" are the positions of the pressure transducer and T-Type thermocouple used to measure the supply pressure and temperature, respectively.
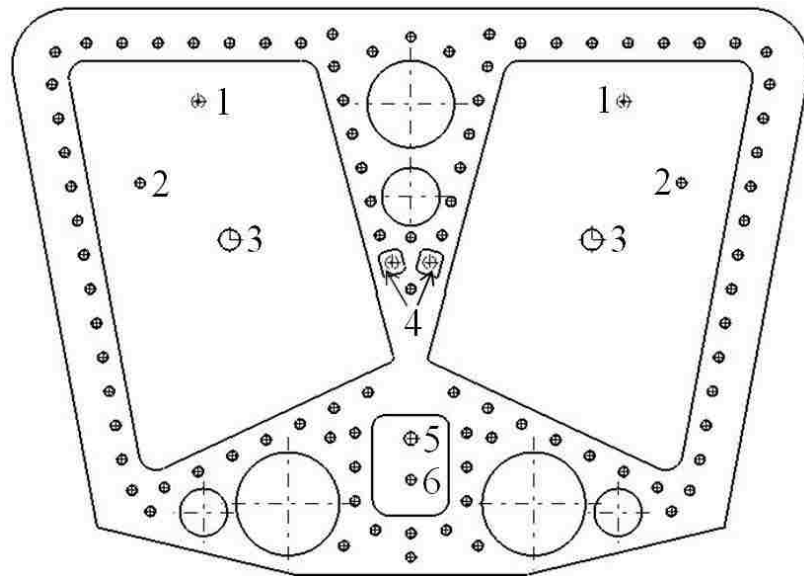
Figure 3.9: Pressure block with the locations of the measuring devices

Figure 3.10: Pressurized N_2 tanks

The supply chamber is fed from a manifold connected to a maximum of sixteen pressurized N_2 tanks at a maximum pressure of 31.0 MPa (4500 psi), shown in Figure 3.10, through a two-stage pressure regulation process (SR4J-680 high capacity pressure regulator). This provides a continuous flow and ensures the supply pressure remains constant in the supply chambers during the filling process. Figures 3.11 and 3.12 are photos of the SFO's supply block and pressure block, respectively, with attached components.
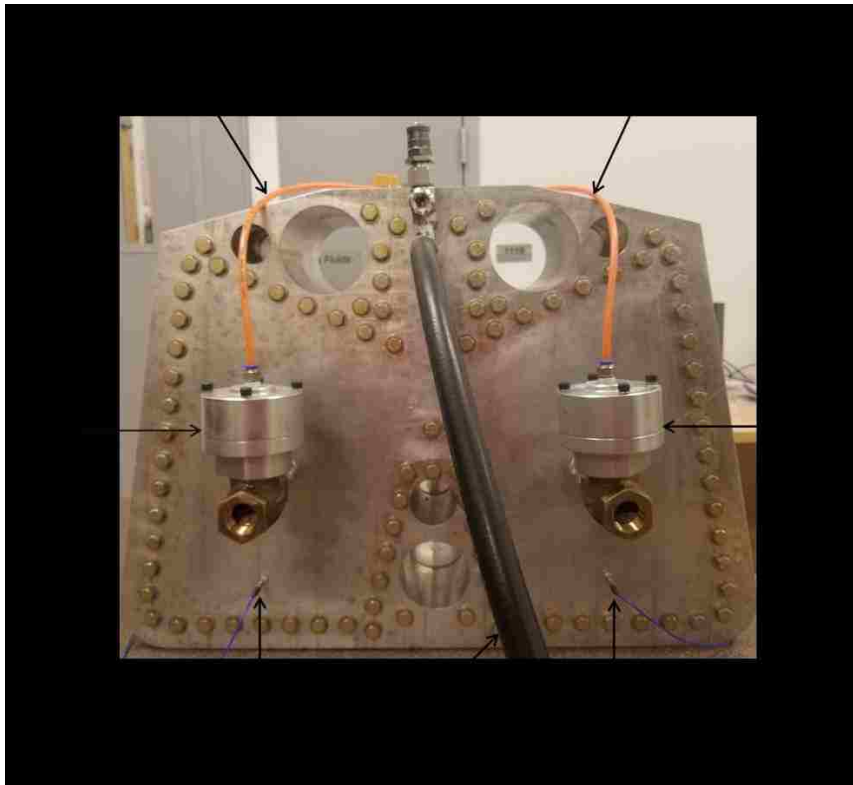
Figure 3.11: Photo of the supply block with components

Figure 3.12: Photo of pressure block with components

3.4: Experimental Control Equipment

To provide consistent and repeatable initial conditions in order to make a fair comparison with the numerical solutions performed by Sidhu [17], it is necessary that the SPF chambers of the SFO not begin to fill until the intended steady supply pressure is reached. In order to accomplish this, a two-position, two-way, externally pilot operated, spring returned normally open directional control valve (part #: LX325110) is placed in the wall of each of the two SPF chambers to initially 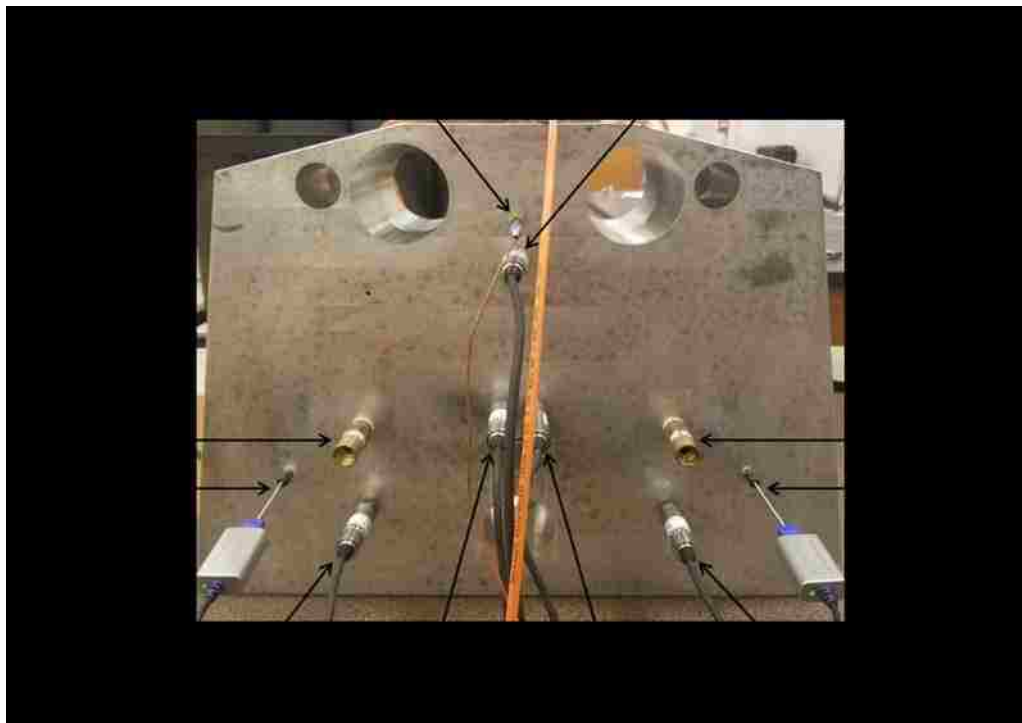allow flow to the atmosphere. The purpose of these valves (referred as "Pilot Valves") is to keep the SPF chamber pressures as low as possible while adjusting the supply pressure.

Figure 3.13 provides a schematic diagram of the pneumatic connections of the experimental equipment used to control the experiment. Compressed air for control of the pneumatic components is supplied from the shop air through a filter-regulator, referred to as "Pilot Pressure Regulator".

The pneumatic line supplying the normally open valves is split from a single line connected to two ball valves labelled "BV_1" and "BV_2". BV_1 is a two-way ball valve used to either allow or block the flow to the pilot valves and BV_2 is also a two-way ball valve connected to a tee splitter that is used to exhaust the pilot lines and release the pressure in the SFO after the process is complete. A photo of this valve arrangement is given in Figure 3.14.
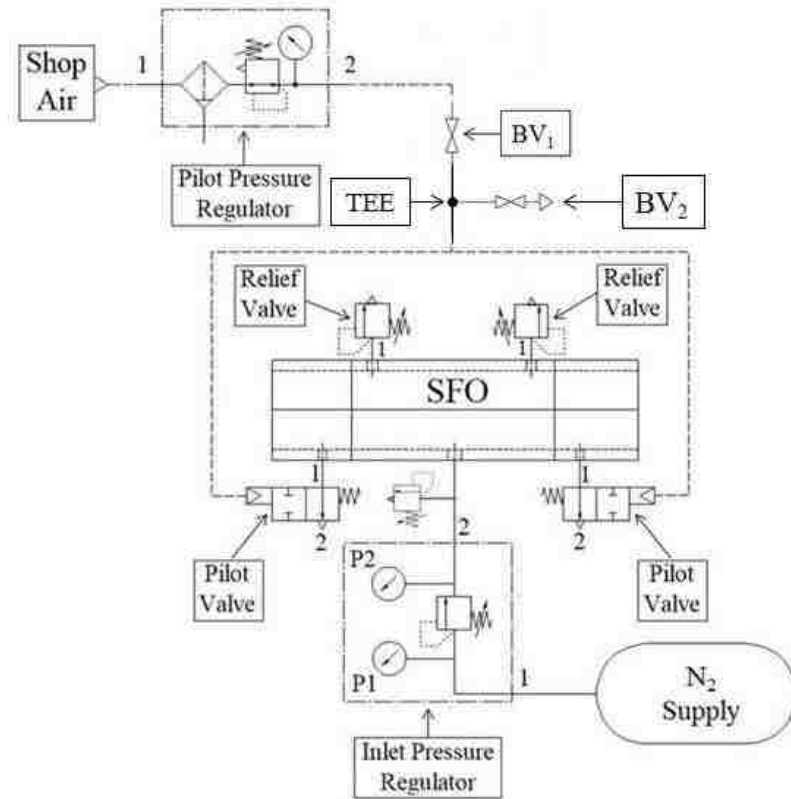
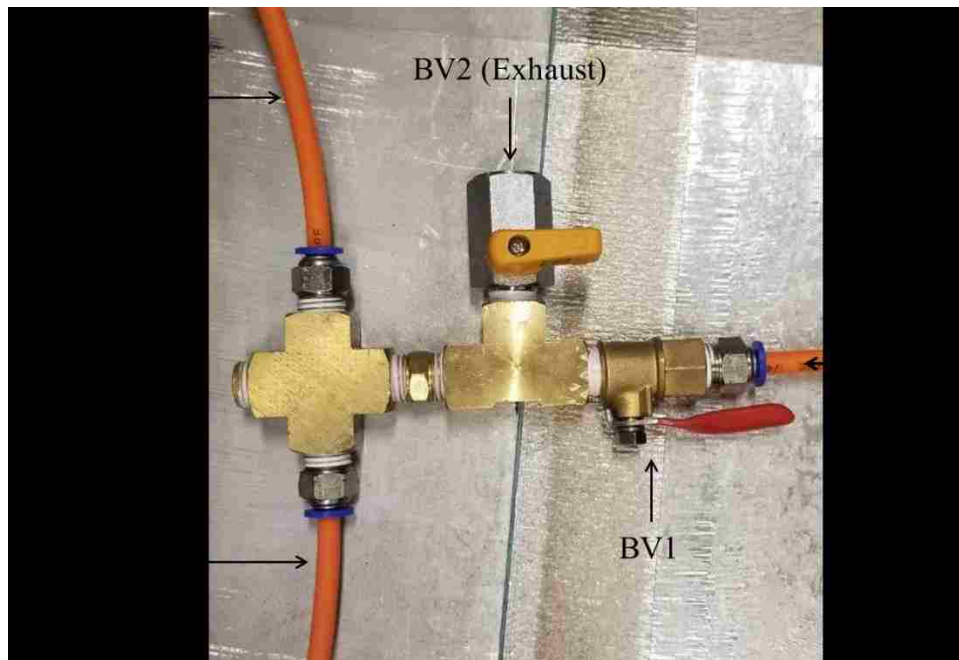Figure 3.13: Schematic diagram of pneumatic connections for the experimental setup

Figure 3.14: Photo of SFO ball valve arrangement

The normally opened pilot valves provide an external pilot-to-line pressure ratio of 8:1, which means that the external pilot pressure required keeping the normally opened pilot valves closed during the filling process is $1/8^{th}$ of the pressure in the SFO. This device is acceptable since the shop air is capable of providing a maximum pressure of 689 kPa (100 psig) with blocked flow, and the expected high pressure in the SFO's chambers is 3.103 MPa (450 psig). The N_2 supply for the SFO is directed through a pressure regulator connected to the N_2 tanks. For safety reasons, a relief valve is located between the inlet pressure regulator and the SFO to limit the maximum pressure into the SFO.

3.5: Data Acquisition System

All pressure measurements are obtained using a National Instrument 6356 series data acquisition system [28]. The thermocouple used to measure the supply temperature is also connected to the NI 6356 series Data Acquisition System with a 10 kΩ resistor inserted from the negative terminal to ground in order to reduce the electrical noise through the analog input terminal [21]. Figure 3.15 shows the NI 6356 A/D converter portion of the LabVIEW program in addition to the analog input assignments for each measurement device. Subscripts R and L identify right and left side measurements.
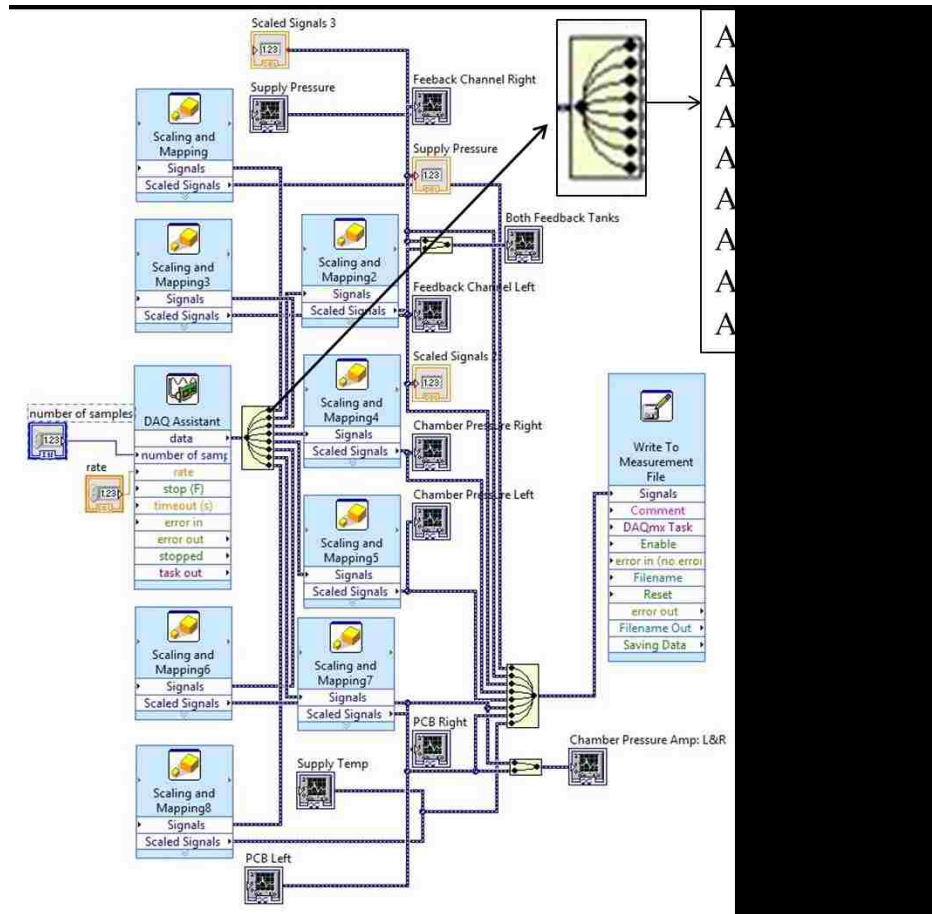
Figure 3.15: LabVIEW program for the NI 6356 series A/D converter

The T-Type thermocouples used to measure the temperature in the SPF chambers are each connected to a NI-USB-TC01 data acquisition system [29]. The NI-USB-TC01 A/D converter portion of the LabVIEW program is displayed in Figure 3.16.
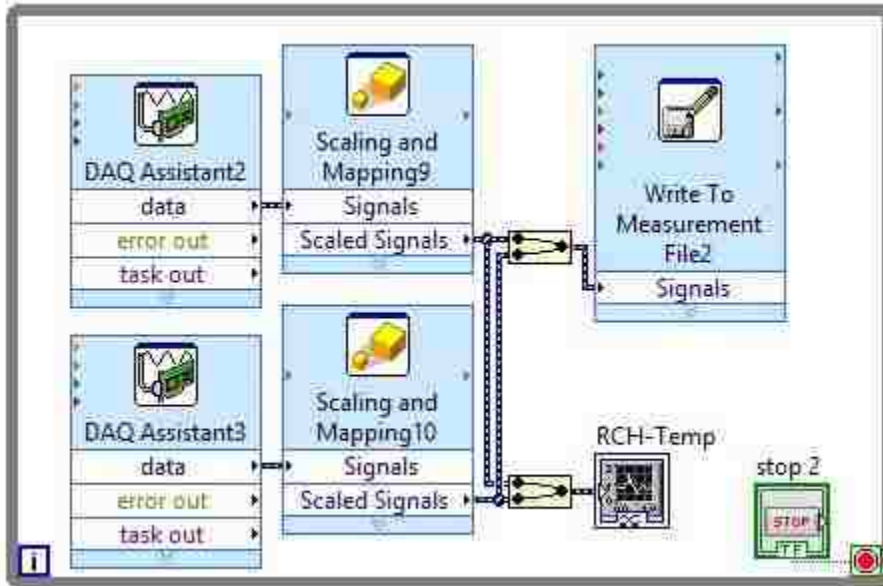
Figure 3.16: Portion of LabVIEW program for the two NI-USB-TC01 A/D Converters

Both LabVIEW sub-programs shown above are of the same overall LabVIEW program run in different while loops. The sampling frequency for the NI 6356 A/D converter used in all experiments is 2000 Hz and the sampling frequency for the NI-USB-TC01 A/D converters is 4.175 Hz; the default sampling frequency for the NI-USB-TC01 A/D converters.

The Virtual Instrument that appears on the computer screen that is used to monitor the readings during the experiments is shown in Figure 3.16. These graphs display the following quantities. The left column includes, from top to bottom, the left SPF chamber pressure amplitudes, the right SPF chamber pressure amplitudes, the supply pressure, the left feedback tank pressure and the left SPF chamber pressure (back pressure), while the right column includes the supply temperature, the left and right SPF chamber temperatures, the right feedback tank pressures, the right SPF chamber pressure (back pressure) and both feedback tank pressures. They are used to ensure that the intended supply pressure is reached as well as whether or not oscillation is present in the

system. When oscillation stops, the experiment is completed, and the N_2 supply is cut-off from the system.
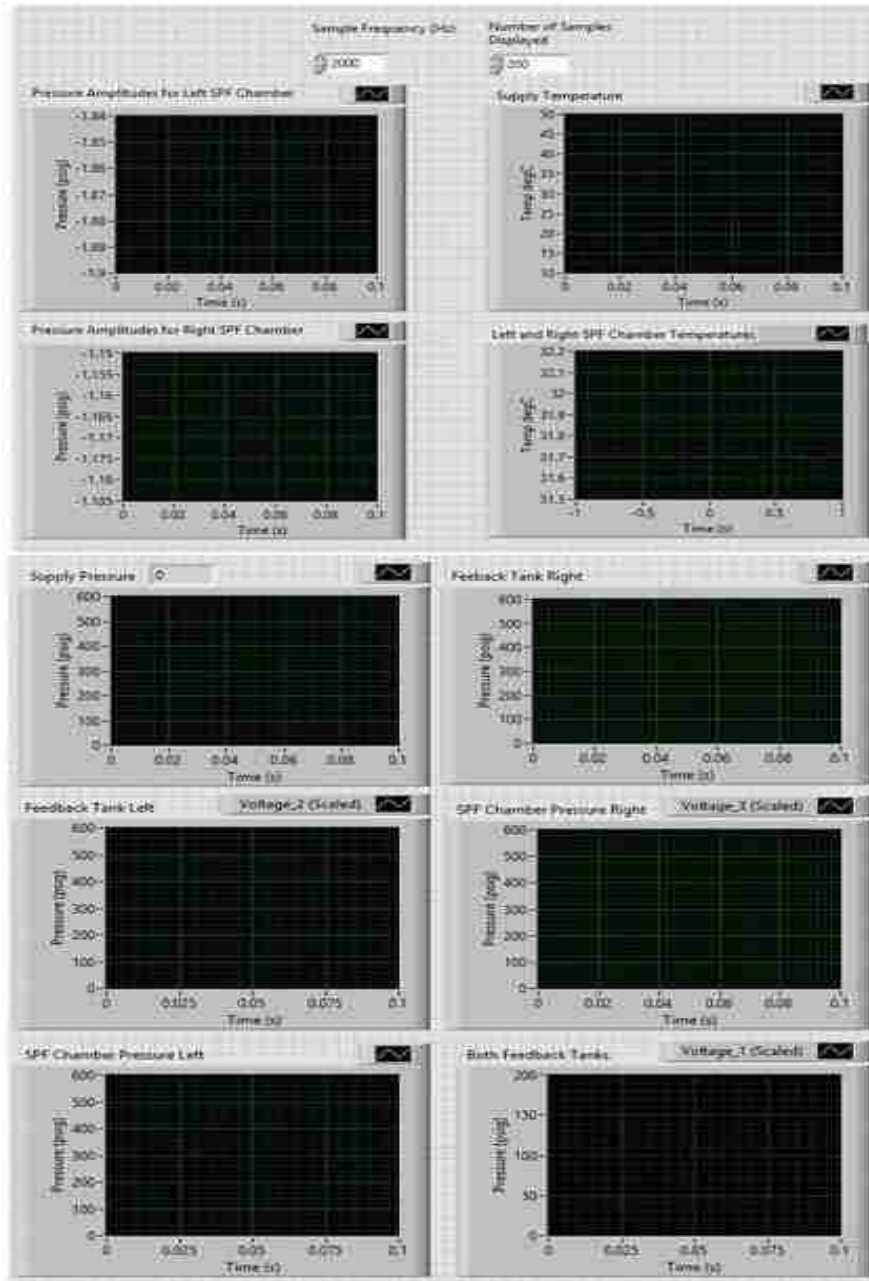

Figure 3.17: Block diagram for the LabVIEW program

Uncertainty analyses regarding the pressure measurements, frequencies and temperature measurements are presented in Appendix B.1 through Appendix B.5.

Chapter 4: Experimental Procedures and Data Processing

The leak test procedure to ensure a negligible leakage from the system is described in Section 4.1 followed, in Section 4.2, by the procedure used to acquire pressure measurements during SPF chamber filling. The methods of processing the raw data to extract the pressure fluctuation amplitudes and frequencies are also considered.

4.1: Leak Test

The leak test for this experiment is conducted at four SFO pressures: 0.731 MPa (106 psig), 1.338 MPa (194 psig), 2.082 MPa (302 psig) and 2.882 MPa (418 psig). For each pressure condition, the pilot valves in the SPF chambers are closed and the SFO is pressurized with N_2 to the steady pressure of interest and the pressure is then recorded versus time for durations ranging from 40 to 50 minutes using a sampling frequency of 2000 Hz. An exponential curve fit of the SFO pressure decrease with time is made using Equation 8. P_o is the initial absolute pressure in Pa and β is the leak constant in 1/s.

$$P(t) = P_o e^{\beta t} \tag{8}$$

Using the ideal gas law and the continuity equation it can be shown that the mass flow rate leaking from the SFO can be expressed as

$$\dot{m}_{leak} = \beta \frac{V_{SFO} \cdot P_o e^{\beta t}}{RT} \tag{9}$$

This value is then compared to the mass flow rate that enters the system for a supply pressure that equals the initial pressure of each leak test. A percent leakage can be defined for each pressure tested as

$$\% \, Leak = \frac{\dot{m}_{leak}}{\dot{m}_{in}} x 100\% \tag{10}$$

The results obtained in this way correspond to a worst-case scenario since it assumes the entire SFO is subjected to the high supply pressure. During the filling process, only the supply chamber, a small volume fraction of the SFO, is subjected to the supply pressure.

4.2: Tank Filling Experiments

The experiments are conducted at four different supply pressure. The lowest supply pressure considered is that which gives chamber oscillations large enough to accurately measure, 2.772 MPa gauge (402 psig). Values of 3.447 MPa gauge (500 psig) and 3.971 MPa gauge (576 psig) are also included.

As an aid in the description of the experimental procedure and for convenience, the schematic diagram of pneumatic connections for the experimental setup previously given is repeated in Figure 4.1.
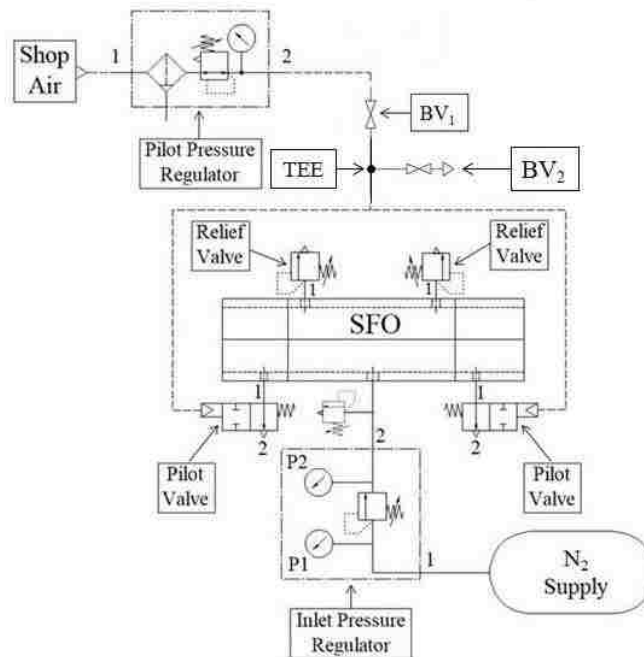

Figure 4.1: Schematic diagram of pneumatic connections for the experimental setup

For each supply pressure tested, the following steps must be completed. A steady flow of N_2 through the device, for each desired supply pressure, is obtained by:

1. closing valves BV_1 and BV_2,

2. fully opening the pilot pressure regulator, and

3. adjusting the supply regulator until the intended pressure in the supply chamber is reached as evidenced on the LabVIEW Virtual Instrument screen.

Instrument recording and the SPF chamber filling process is started by:

4. selecting the record button on the LabVIEW program, and

5. opening valve BV_1,

The filling process is stopped, and instrument recording ended by:

6. closing the N_2 regulator, when the flow is no longer choked as indicated by an increase in the supply pressure as indicated on the LabVIEW Virtual Instrument, and

7. selecting the stop button on the LabVIEW program.

The SFO and SPF chambers are depressurized by:

8. closing the BV_1 valve and opening the BV_2 valve.

4.3: Determination of Pressure Fluctuation Amplitudes and Frequencies

The methods for determining the pressure amplitudes and frequencies in the feedback tanks and the SPF chambers are explained. The examples using the MATLAB code are displayed in Appendix C.1. Additionally, a comparison of the right and left SPF chambers and feedback tanks are shown in Appendix C.2.

4.3.1: Feedback Tank Pressure Amplitudes and Frequencies

The objective of the procedure is to capture a number of complete cycles for a time interval of 0.1 seconds at selected points in the feedback tank filling pressure trace from which to determine the pressure fluctuation amplitude and frequency. The following is the step-by-step procedure for obtaining the feedback tank pressure amplitudes and frequencies for a given back pressure ratio (P_r):

1. The back pressure of interest is selected and the feedback tank pressure profile is plotted with time for the initial max peak points displayed in Figure 4.2. The time interval is 0.1 seconds for all cases with the back pressure of interest located at the mid-point.
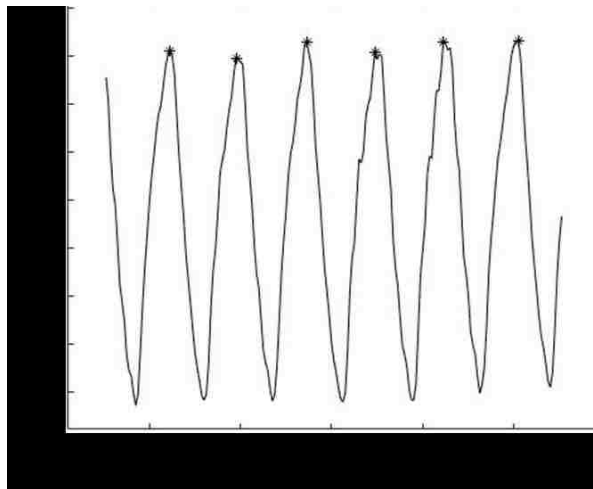

Figure 4.2: Feedback tank pressure with initial maximum peaks

2. Maximum peak points that can manually be seen as not contributing to complete cycles are eliminated.

3. Initial minimum peak pressure points are plotted and displayed in Figure 4.3
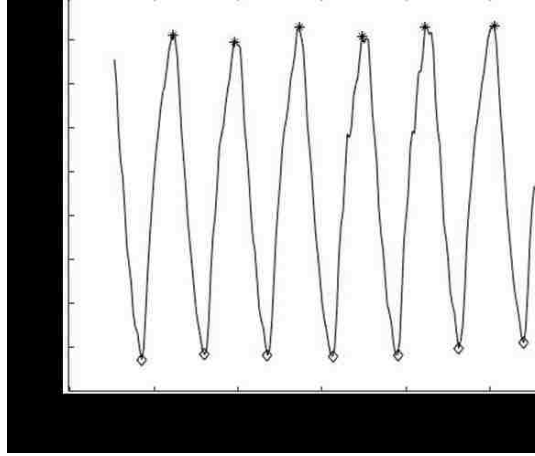
Figure 4.3: Feedback tank pressure with initial minimum peaks

4. Minimum peak points that can manually be seen as not contributing to complete cycles are eliminated as shown in Figure 4.4. The figure also identifies that two maximum peak points and one minimum peak point represents a single cycle.
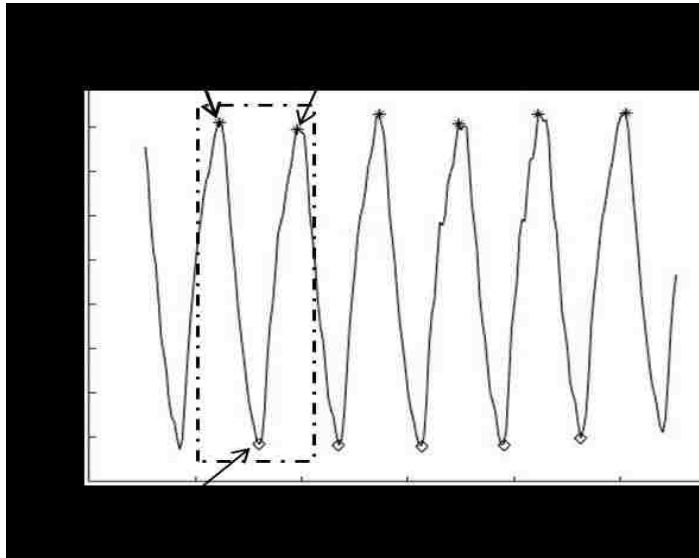

Figure 4.4: Final feedback peaks used for obtaining pressure amplitudes and frequencies

5. The pressure amplitude and frequency is determined for each cycle "k".

$$P_{Fb,k} = \frac{P_{max,i} - P_{min,i} + P_{max,i+1} - P_{min,i}}{2} \qquad (11)$$

$$f_k = \left(t_{P_{max,i+1}} - t_{P_{max,i}}\right)^{-1} \qquad (12)$$

6. The average pressure amplitudes frequencies are determined for "N" number of cycles.

$$P_{Fb} = \frac{\Sigma_{k=1}^{N} P_{Fb,k}}{N} \qquad (13)$$

$$f = \frac{\Sigma_{k=1}^{N} f_k}{N} \qquad (14)$$

The uncertainties are determined using the methods described in Appendix B.2 for Feedback Tank Amplitudes and Appendix B.4 for frequency.

4.3.2: SPF Chamber Pressure Amplitudes and Frequencies

The following is the step-by-step procedure for obtaining the SPF Chamber pressure amplitudes and frequencies for a given back pressure ratio (P_r):

1. The back pressure is selected and the SPF pressure is plotted with time as indicated in Figure 4.5. The black curve is the raw data and the red curve is smoothed using a three-point moving average.
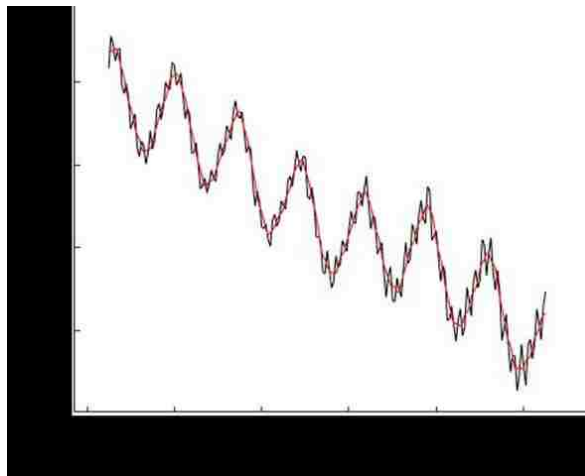

Figure 4.5: SPF chamber pressure with raw data (black) and smoothed data (red)

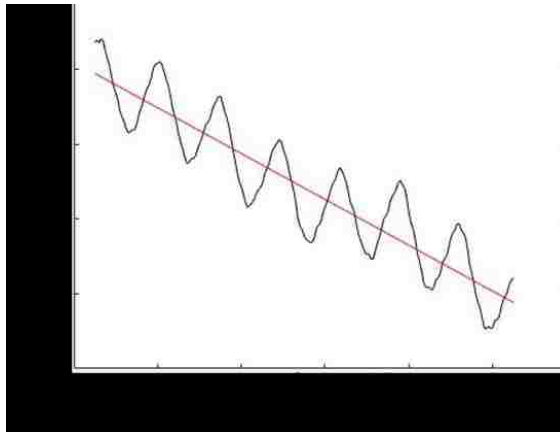2. A line-of-best-fit is plotted with the smoothed data in Figure 4.6.

Figure 4.6: SPF smoothed pressure and the line-of-best-fit

3. Each data point is subtracted from the equation of the line-of-best-fit for a mean
    fluctuation about zero in Figure 4.7. The figure also shows the maximum and
    minimum points used to determine the pressure amplitudes and frequencies. Using
    this data, the method is the same as the feedback tank pressure amplitudes and
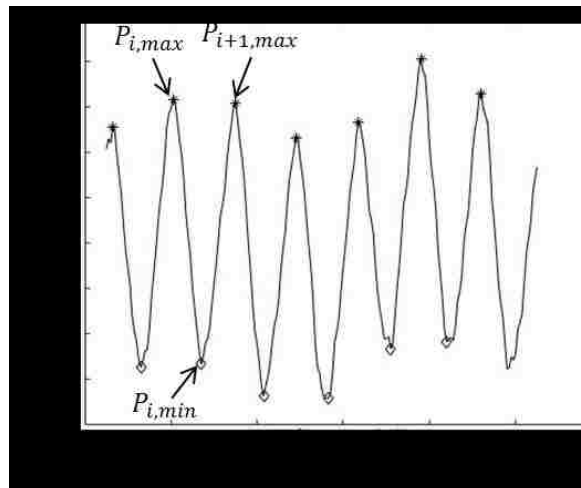   frequencies.

Figure 4.7: SPF chamber pressure fluctuation about mean zero pressure

The uncertainties are determined using the methods described in Appendix B.5.3
for feedback tank amplitudes and Appendix B.5.4 for frequency.

The piezoelectric pressure sensors used to measure the pressure amplitudes in the
SPF chambers experience a rapid voltage (pressure) increase when the filling process

45

begins. This is due to the inherent characteristic of piezoelectric transducers responding

to the pressure changes rather than the pressure values. The mean voltage values then

drop while the SPF chambers continue to fill, eventually giving a zero mean value. The

pressure fluctuations of interest are superimposed on this mean variation. This increase in

mean value caused a problem for accurate measurement of the pressure fluctuation

amplitudes in the SPF Chambers. For the greatest accuracy, a full scale reading of +/- 1

Volt is used for the A/D converter. For high SFO supply pressures, the voltage peaks

exceed the 1 Volt maximum resulting in signal "clipping", which results in the horizontal

line in Figure 4.8. Once the sensor mean values are below the 1 Volt maximum, pressure

amplitudes can be measured. As a result, some of the pressure amplitudes cannot be

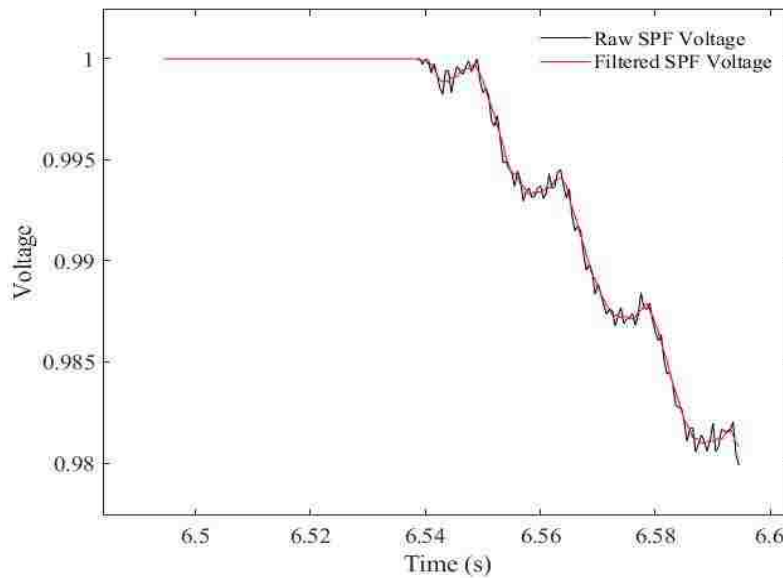measured at low back pressure ratios.

Figure 4.8: Voltage versus time above and below the 1 volt maximum

The SPF chamber and feedback tank pressure amplitudes and frequencies are

presented in the following chapter using the methods described above for all supply

pressures of interest. The change in temperature due to filling is also discussed.

Chapter 5: Experimental Results and Discussion

Results of the leak test, the SPF chamber temperature measurements results, the frequency and amplitude results for a repeatability test as well as the frequency and amplitude results at various supply pressures are presented and discussed in this chapter.

5.1: Leak Test Results

The leak constant and coefficient of determination for the least squares curve fit of the experimental data using Equation 8 for all supply pressures considered are shown in Table 5.1. Also included are the values of the percentage leak determined using Equations 9 and 10. The coefficient of determination values indicate a very good fit while the percentage leak increases with supply pressure as indicated in Figure 5.1.

Table 5.1: Leak Test Results

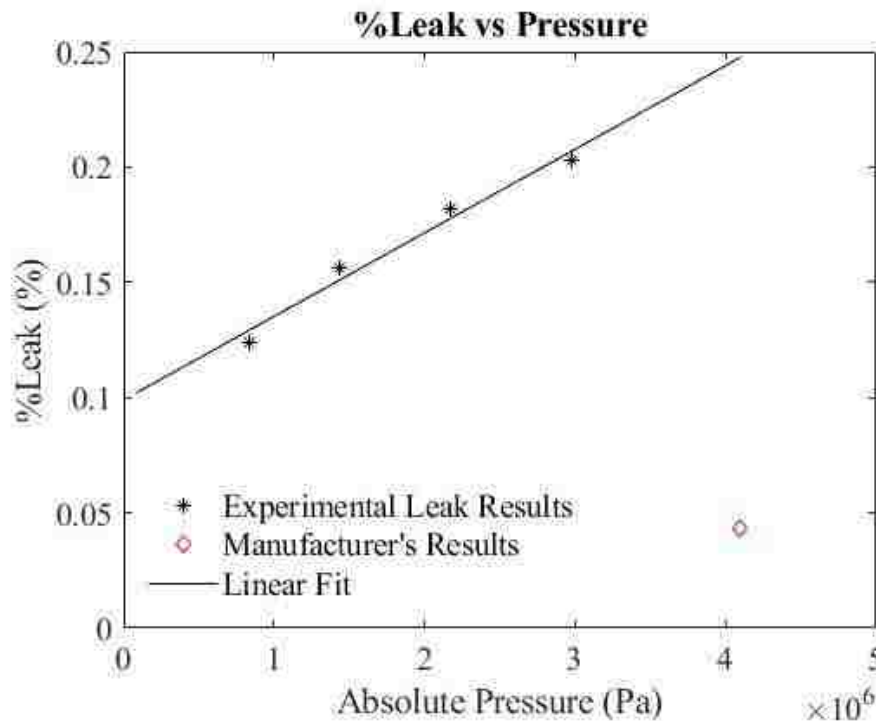| P_o MPa abs	$\beta\, x10^{+5}$ (1/s)	R^2	% Leak
0.830	-4.822	0.9994	0.124
1.439	-6.066	0.9998	0.156
2.177	-7.086	0.9999	0.182
2.979	-7.872	0.9998	0.203

Figure 5.1: Leak test results; %Leak vs pressure

The manufacturer of the Oil-Resistant Aramid/Buna-N Gasket provided a leak rate of 0.05 cc/min at 4 MPa gauge (580 psig) with a gasket thickness of 1/16" [30]. Using this information, the manufacturer's percentage leak rate is 0.043 %; significantly lower than the results from the experimental leak test. This is likely due to the difference in the pre-compressed loads prior to pressurizing the system. Although the estimated maximum percentage leakage of approximately 0.2% is greater than the manufacturer's specification, this is not likely to affect the results and hence, is acceptable. An example of the MATLAB program used to calculate the percentage leak is presented in Appendix C.3.

5.2: Non-dimensional Parameters

In order to generalize the pressure and frequency results it is necessary to present the results in a non-dimensional manner. A non-dimensional analysis was conducted that resulted in the following parameters: non-dimensional back pressure, non-dimensional SPF chamber pressure amplitude, non-dimensional feedback tank amplitude and the non-dimensional frequency given by Equations 15, 16, 17 and 18, respectively.

$$P_r = \frac{P_{b,abs}}{P_{s,abs}} \tag{15}$$

$$\wp_{amp} = \frac{P_{amp}}{P_{s,abs}} \tag{16}$$

$$\wp_{Fb} = \frac{P_{Fb}}{P_{s,abs}} \tag{17}$$

$$\mathcal{F} = \frac{\rho V_{fb} f}{\dot{m}} \tag{18}$$

The uncertainty analyses for all non-dimensional equations are shown in Appendix B.6.

5.3: Repeatability Study

In order to investigate the repeatability of the measurements a repeatability study is conducted at supply pressures of approximately 3.969 MPa (576 psig) using four trials. The actual values of supply pressures tested are given in Table 5.2 and will be referred to as the nominal value of 3.971 MPa (576 psig) for convenience. These results are displayed non-dimensionally for fifteen evenly spaced non-dimensional back pressure values in the range from 0.18 to 0.34 to account for discrepancies in the actual supply pressures and temperatures. Figure 5.2 shows the non-dimensional feedback tank pressure amplitudes versus the non-dimensional SPF chamber pressures for the

repeatability test as well as the mean values for each non-dimensional SPF chamber pressure. The mean value of this test is used to compare with the other supply pressure cases. All feedback tank amplitudes are within uncertainties, shown with the error bars, for their corresponding SPF chamber pressures.

Table 5.2: Gauge Supply Pressures for the Repeatability Test

Trial #	P_s
1	3.985 MPa (574 psig)
2	3.971 MPa (576 psig)
3	3.978 MPa (577 psig)
4	3.971 MPa (576 psig)
Nominal (Mean)	3.970 MPa (575.8 psig)
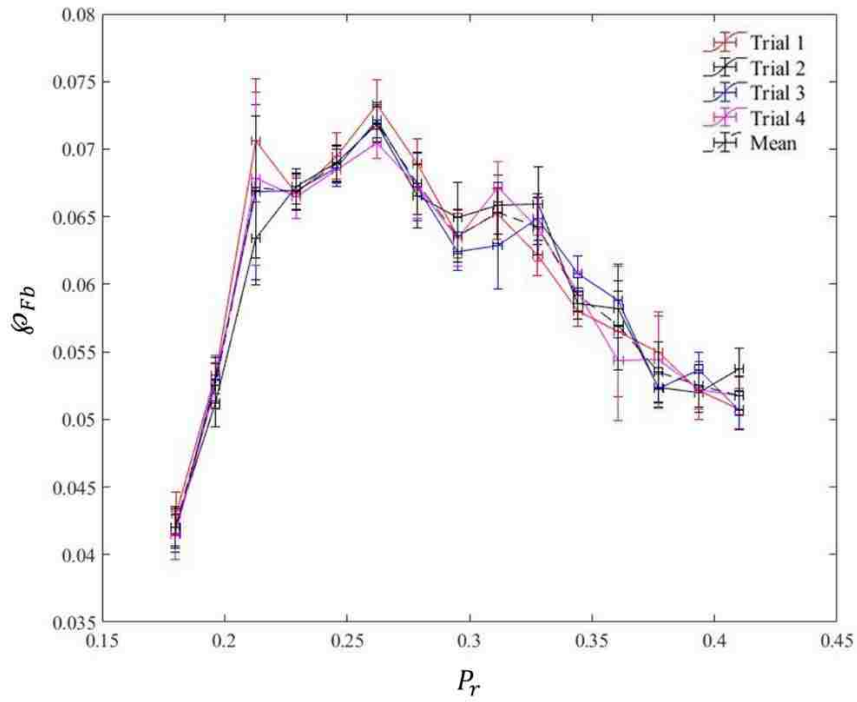
Figure 5.2: Non-dimensional feedback tank amplitudes for the repeatability test at an

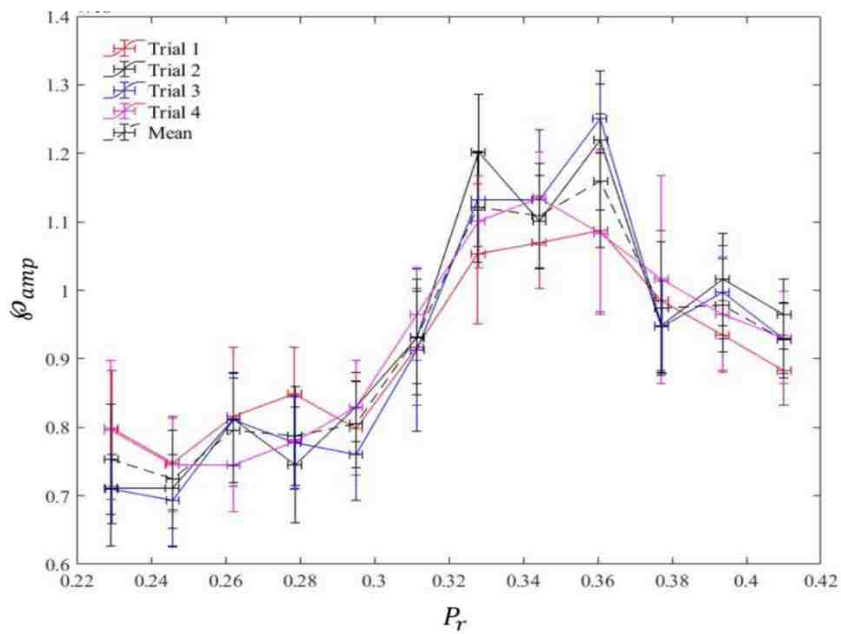average supply pressure of 3.971 MPa (576 psig)

Figure 5.3: Non-dimensional SPF Amplitudes for the Repeatability Test at Mean Supply

Pressures of 3.971 MPa (576 psig)

Figure 5.4 shows the non-dimensional frequency versus the non-dimensional SPF chamber pressures for the repeatability test. All frequencies are obtained using the feedback tank results, however, all the dimensional frequency results obtained in the SPF chambers are shown in tabular form in Appendix C.4 and Appendix C.5 to compare with the results obtained with the feedback tanks. The maximum percentage difference between the two values is always less than 2. Similar to the prior cases displayed in Figures 5.2 and 5.3, there is a strong agreement in the non-dimensional frequencies for all non-dimensional SPF chamber pressures.
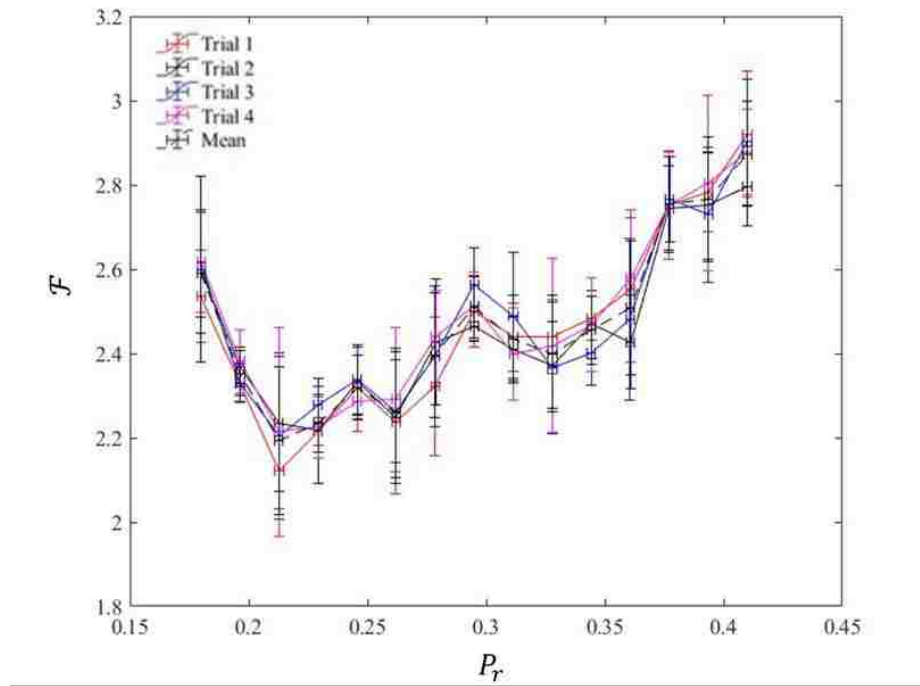

Figure 5.4: Non-dimensional Frequency for the Repeatability Test at Mean Supply Pressures of 3.971 MPa (576 psig)

5.4: Effect of Varying the Supply Pressure

The experimental results, including the mean values from the repeatability test, are compared non-dimensionally for four supply pressures: 2.110 MPa (306 psig), 2.772

MPa (402 psig), 3.440 (499 psig) and 3.971 MPa (576 psig). The significance of 2.110

MPa (306 psig) being the lowest pressure is that it is the lowest supply pressure that

contains SPF chamber amplitudes great enough to be captured with the PCB 113B28

piezoresistive pressure sensors with reasonable uncertainties relative to the magnitudes

while capturing the full range of SPF chamber pressure ratios chosen.

Figure 5.5 shows the comparison of the non-dimensional feedback tank

amplitudes for the four cases discussed above. Like the results shown in Chapter 5.3, all

feedback tank amplitudes are within the uncertainties for all cases. The low-pressure case

yields the lowest average value for all cases considered.
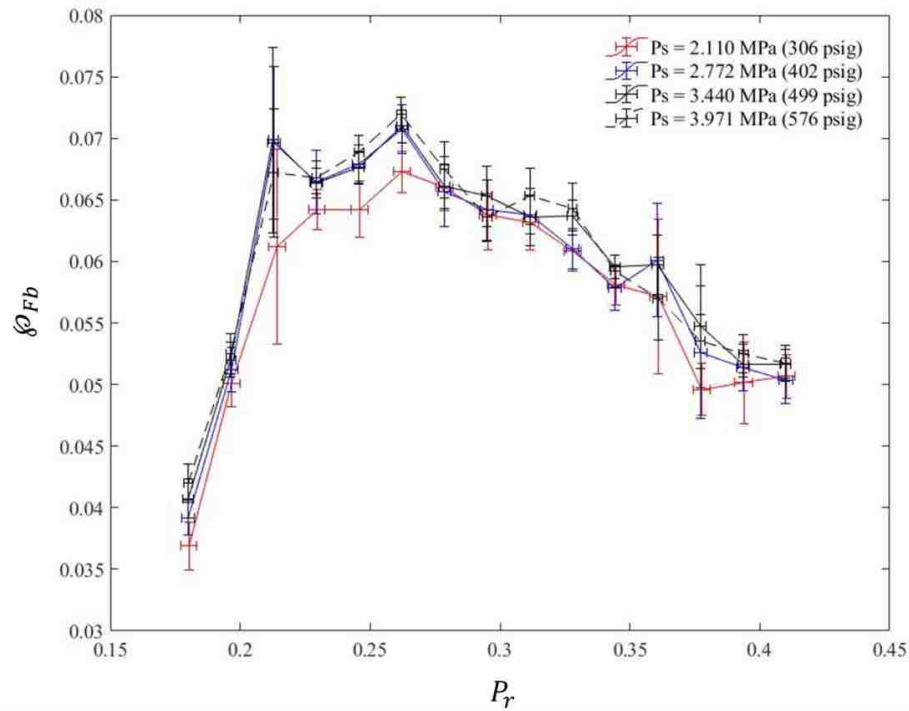
Figure 5.5: Effect of Supply Pressure on Non-dimensional Feedback Tank Pressure

Amplitude

Figure 5.6 shows the results of the non-dimensional SPF chamber amplitudes for

all supply pressure cases. All values are again seen to be within the uncertainties. Similar

to the results in the feedback tanks, the low-pressure case also yields the lowest average results. Figure 5.7 shows the results of the non-dimensional frequency for all supply pressure cases of interest. All frequencies are within the uncertainties, similar to the SPF chamber amplitudes.
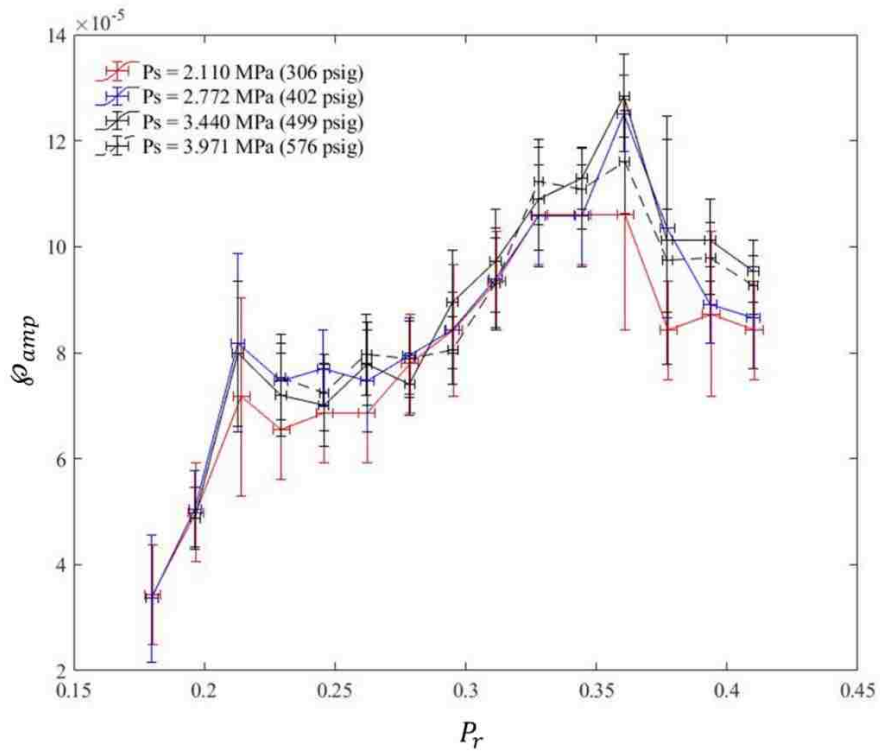

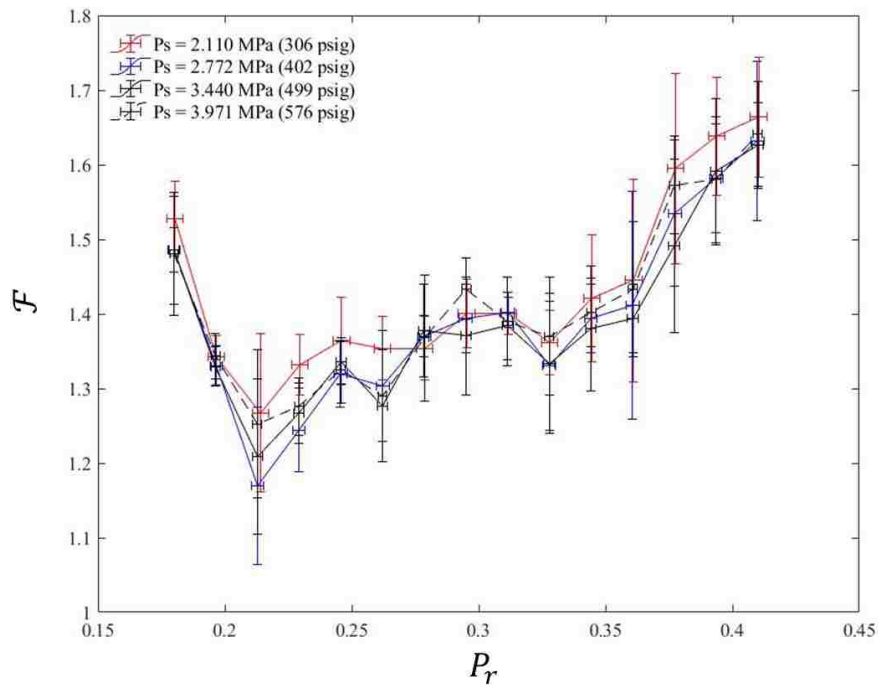Figure 5.6: Effect of Supply Pressure on Non-dimensional SPF Chamber Amplitude

Figure 5.7: Effect of Supply Pressure on Non-dimensional Frequency

The fact that each of the above non-dimensional variable plots collapsed the data for all supply pressures considered is significant in that it shows that these are the correct non-dimensional quantities. The dimensional values of the pressure amplitudes, mean SPF pressure variation values, and frequencies for the cases discussed in this chapter are displayed in tabular form in Appendix C.5.

5.5: Temperature Results

The measured variation of temperature in the right and left SPF chambers and supply chamber are presented and discussed for supply pressures of 0.400 MPa (58 psig) and 2.758 MPa (400 psig), that are chosen to represent the wide range of supply pressures considered. Figure 5.8 include graphs of the temperature and pressure increase for a supply pressure of 0.400 MPa (58 psig) in the left column and a supply pressure of 2.772

MPa (402 psig) in the right column. The supply chamber pressures and temperatures are also shown in each case. Once the pilot valves are actuated and the SFO begins to fill, rapid increases in temperature are present in the left and right SPF chambers for both supply pressure cases. As the SFO continues to fill, there is an obvious decay in the slope of temperature. Eventually, at relatively high pressures, the temperatures in both SPF chambers approach constant values. In the beginning stages of the filling process, the temperature difference between the SPF chambers and the ambient atmosphere and hence the rate of heat transfer to the ambient air is small and the temperature rise process is approximately isentropic. As the temperature difference between the SFO and ambient becomes great enough, the rate of heat transfer is sufficient to maintain an approximately constant temperature. The kinetic energy of the jet flow being converted to internal energy causes the temperature in the SPF chambers to increase. The lower pressure case does not exhibit as great of a value due to a lower mass flow rate and thus, does not reach a constant peak temperature before the system is no longer in the choked condition (indicated by the increase in the supply pressure curve). This implies that at the beginning of the filling process, the system more closely resembles that of an isentropic process and then transforms into an approximately isothermal one near the end of filling.

It can also be seen that the supply temperatures are essentially constant in the supply chambers during the filling process for both cases. The slight decrease in the temperature for the 2.770 MPa (402 psig) case, which is 0.56% of the initial temperature, is likely due to slight changes in the supply chamber temperature due to the gas expansion process from the higher pressure N_2 tanks and the SFO's large thermal time constant. It is also noted that the supply temperature for the supply pressure case of

2.758 MPa (400 psig) is approximately 10°C lower than the 0.400 MPa (58 psig) case. It is speculated that this is due to the fact that lower pressure N_2 tanks are used to provide the lower supply pressures. The low supply pressure also corresponds to a lower inlet ass flow rate which allows the supply flow more time to transfer heat to the surroundings and hence, remain closer to the atmospheric temperature.
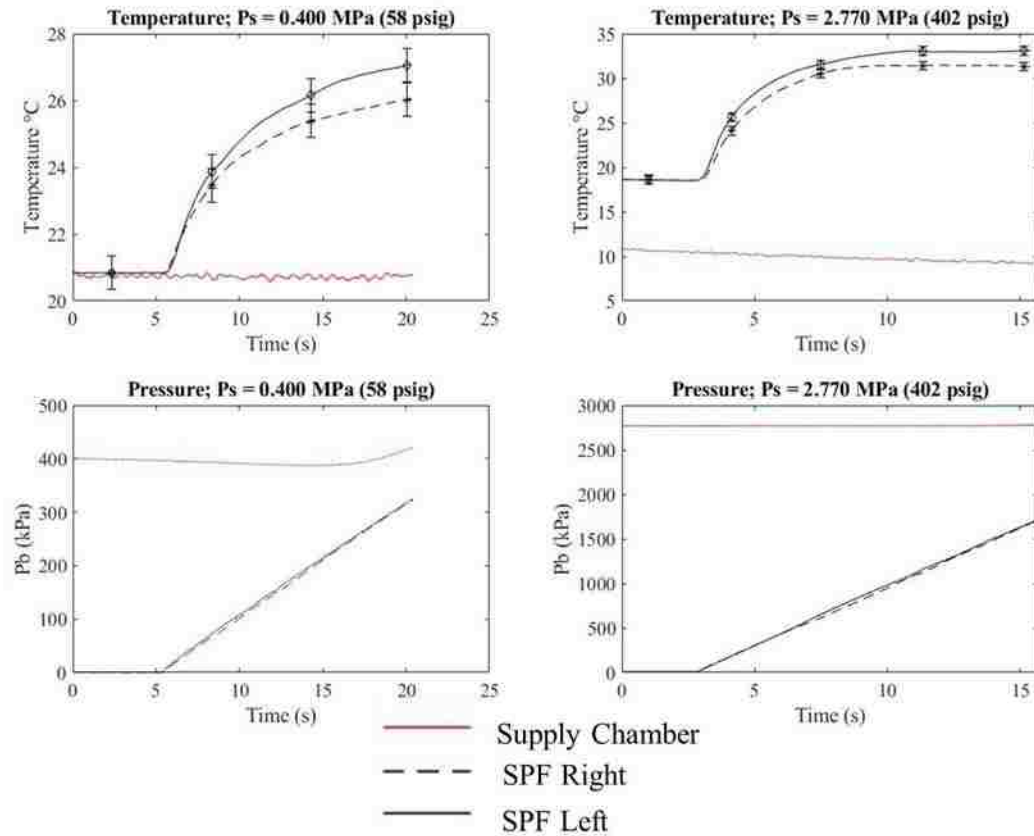

Figure 5.8: Variation of SPF Chamber Temperature and Pressures with Time for Two Supply Pressures

In both cases, the right SPF chamber temperatures experience slightly lower temperatures than the left SPF chamber and the difference is not within the uncertainties for the high-pressure case. This is believed to be due to the slightly lower pressures in the

right SPF chambers which are the result of an extremely low secondary frequency of oscillation that will be discussed later.

5.6: Analysis of Results Compared to Numerical Solution

Figure 5.9 shows the non-dimensional SPF chamber amplitudes, the non-dimensional feedback tank amplitudes and the non-dimensional frequencies versus the non-dimensional SPF chamber pressure for the cases at the supply pressures considered.
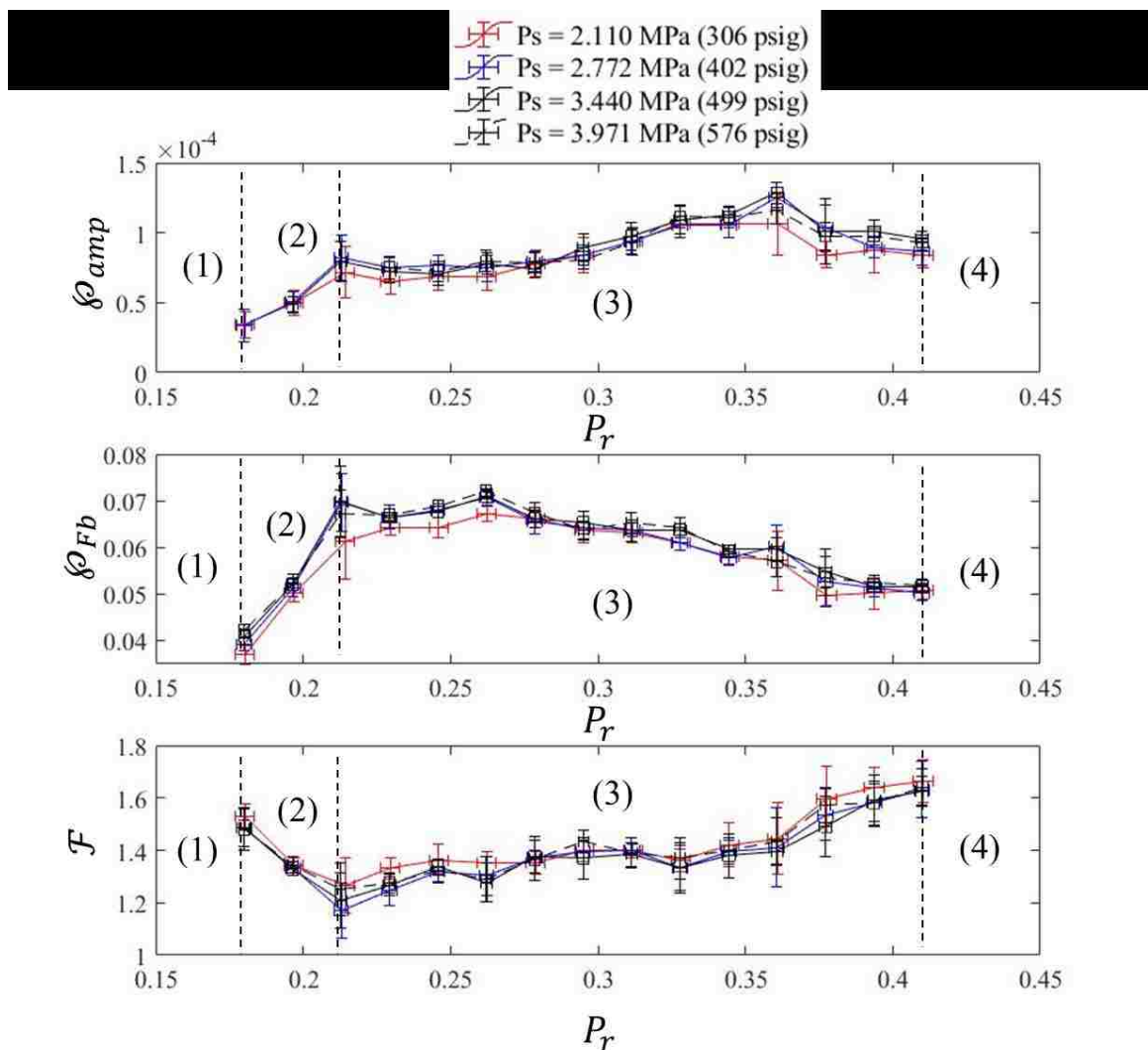
Figure 5.9: Non-dimensional Parameters at Various Supply Pressures versus Non-dimensional SPF Chamber Pressures

Four regions have been identified on the graph for comparison with the numerical results of Sidhu [17]. For ease of comparison, Sidhu's results for a supply pressure are presented in Figure 5.10.
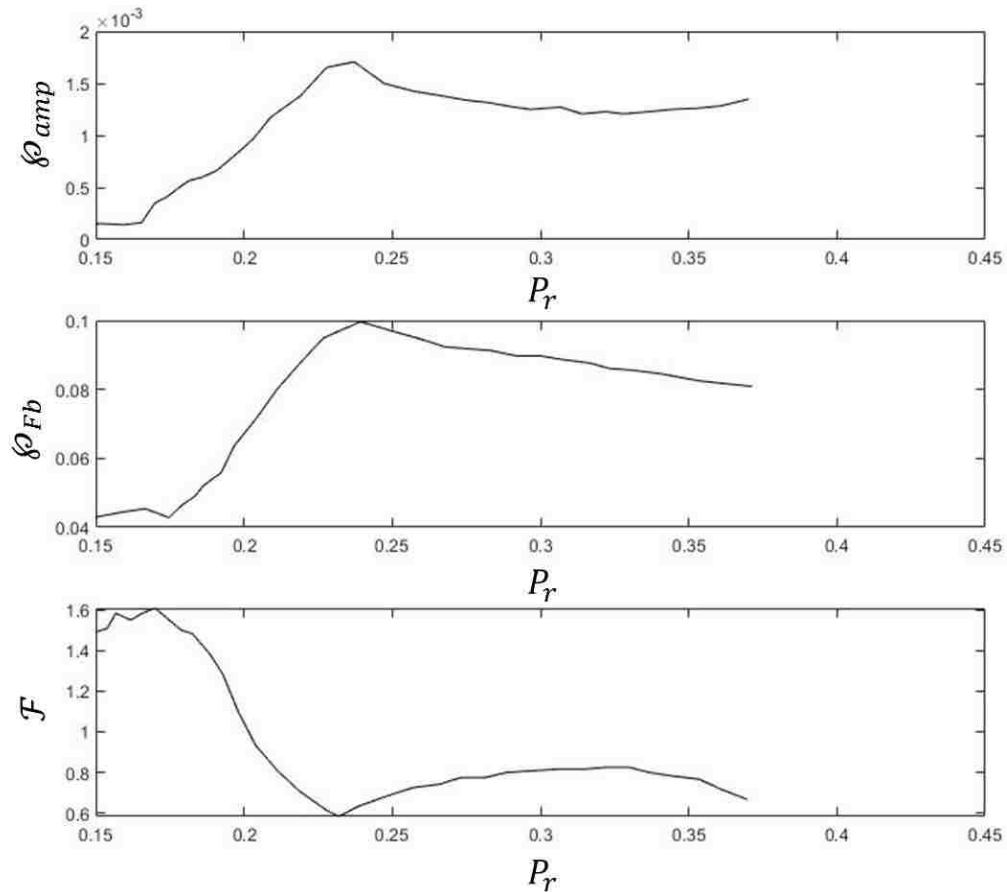
Figure 5.10: Sidhu's [17] Non-dimensional Parameters at a Supply Pressure of 3.65 MPa (530 Psig) versus Non-dimensional SPF Chamber Pressure

Sidhu [17] found no oscillation for non-dimensional SPF chamber pressures less than 0.13. In this case, the jet momentum is such that the jet split is stable into the two channels. Very small oscillations of approximately constant frequency occur for values between 0.13 and 0.175. The numerical solution reveals that the slightly smaller momentum supersonic jet experiences small oscillations about the splitter and the Coanda

59

Effect is not strong enough to influence the jet. These ranges approximately correspond to region (1) in Figure 5.9 ($P_r < 0.18$). In the current study, it was not possible to obtain reliable experimental results for the SPF chamber amplitudes in this range due to the limitations of the equipment, hence a fair comparison is not possible. The SPF chamber pressure range of approximately 0.18 to 0.215, region (1), the feedback tanks and SPF chamber pressure amplitudes experience an approximately linear increase while the frequency decreases in an approximately linear manner. This is in agreement with Sidhu's results as well as the experimental results of Xu [15]. In this region the jet momentum reduces as the SPF chamber pressure increases. This allows the Coanda Effect to have a greater influence and the jet oscillation amplitude increases resulting in a lower frequency and larger feedback tank and SPF chamber amplitudes [31].

In the range of $0.215 \leq P_r \leq 0.38$, Sidhu found that 1) the non-dimensional frequency remains relatively constant while the current experimental results increase slightly, 2) the non-dimensional feedback tank amplitude decreases slightly, which is consistent with the current findings and 3) the non-dimensional SPF chamber amplitude remains approximately constant with a slight decrease and then increase whereas the current curve includes a change in character at a value of non-dimensional SPF chamber pressure of about 0.38. In all cases the experimental results indicated oscillations up to P_r values of approximately 0.41, which are greater than the numerical prediction.

Although the trends found experimentally are similar to those predicted by the numerical method, the experimental frequencies are considerably higher and the feedback tank and SPF chamber amplitudes lower.

It is also noticed from the current results, that the variation of the mean feedback tank pressures exhibits a low frequency variation. This can easily be seen in the plot of mean feedback tank and SPF chamber pressures versus non-dimensional time given in Figure 5.11. These non-dimensional quantities are defined in Equations 19, 20 and 21. The pressure in the feedback tank (P_{Fb} in Equation 19) is filtered using a moving average of 500 points; the smallest value that filtered out the primary oscillations but did not affect the secondary oscillations. Furthermore, the SPF chamber pressure (P_{EC}) is filtered using a three-point moving average.

$$\bar{\wp}_{Fb} = \frac{P_{Fb}}{P_S} \tag{19}$$

$$\bar{\wp}_{EC} = \frac{P_{EC}}{P_S} \tag{20}$$

$$\mathcal{T} = \frac{t - t_{min}}{t_{max} - t_{min}} \tag{21}$$
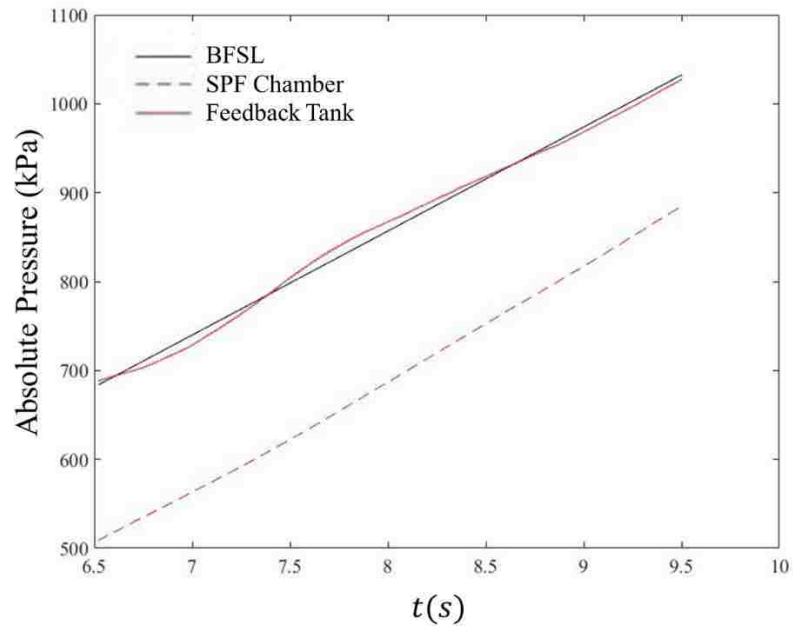
Figure 5.11: Mean feedback tank pressure and mean SPF chamber pressure for the duration of section (2) Ps = 2.772 MPa (402 psig)

It is possible that this low frequency oscillation is due to the fact that the SPF chambers connect the exhaust port to the control ports of the oscillator creating a feedback path that allows recirculation switching to occur as well as load switching. Due to the large size of this volume, a low frequency would be expected although it was not noticed in Sidhu's numerical solution. This phenomenon certainly requires further investigation.

Chapter 6: Conclusions and Future Work

Conclusions from the results presented in Chapter 5 are listed in Chapter 6.1. Recommendations for future work are listed in Chapter 6.2.

6.1: Conclusions

A high pressure bi-stable supersonic fluidic oscillator has been designed, built and tested resulting in the following conclusions.

1) The tested device is capable of sustained oscillations for the four different supply pressures tested: 2.110 MPa (306 psig), 2.772 MPa (402 psig), 3.440 MPa (499 psig) and 3.971 MPa (576 psig) over a non-dimensional SPF chamber pressure range of approximately 0.18 to 0.41.

2) The experimental frequencies are considerably higher (59 Hz to 85 Hz) than those predicted using a 2D/0D numerical model (30 Hz to 57 Hz) and the experimental SPF chamber pressure amplitudes (76 Pa (0.011 psi) to 455 Pa (0.066 psi)) are considerably lower than the numerical results (137.9 Pa (0.02 psi) to 5171 Pa (0.75 psi))

3) The SPF chamber temperature measurements reveal that at the beginning of the filling process, the system is approximately isentropic and then eventually transforms to isothermal.

4) The stages of filling based on non-dimensional SPF chamber values are, with some minor differences, consistent with the explanation given using the numerical solution.

5) In addition to the primary oscillation due to load-switching, a secondary low frequency oscillation is observed which could be caused by the large SPF chambers acting as feedback paths associated with recirculation.

6.2: Future Work

Additional experimental research is required to:

1) study the effects that scaling have on frequency and amplitude,

2) study the effects that changing the feedback tank volumes have on frequency and amplitude for a given oscillator size,

3) study the effects that the SPF chamber volumes have on the amplitude and whether they have an effect on the frequency, and

4) test large scale, high temperature oscillator with varying SPF chamber volumes.

References

[1] Koehler, W., Plege, B., Sahm, K. F., and Padmapriya, N., 2017, "Metal Forming: Specialized Procedures for the Aircraft Industry," *Encyclopedia of Materials: Science and Technology*, Elsevier, Germany, pp. 5427–5433.

[2] Cullen, G. W., and Korkolis, Y. P., 2013, "Ductility of 304 Stainless Steel under Pulsed Uniaxial Loading," International Journal of Solids and Structures, **50**(10), pp. 1621–1633.

[3] Joyce, J. W., 1983, *Fluidics - Basic Components and Applications*, HDL-SR-83-9, U.S. Army Electronics Research and Development Command, Adelphi, Maryland.

[4] Jayamohan, H., Sant, H. J., and Gale, B. K., 2013, "Applications of Microfluidics for Molecular Diagnostics," *Microfluidic Diagnostics*, G. Jenkins, and C.D. Mansfield, eds., Humana Press, Totowa, NJ, pp. 305–334.

[5] Smith, T., 2014, "Coanda Effect," Coanda Effect [Online]. Available: http://www.thermofluids.co.uk/effect.php. [Accessed: 15-Sep-2018].

[6] Hiroki, F., Masuda, T., and Yamamoto, K., 1989, "Supersonic Fluidic Oscillator," Proceedings of the JFPS International Symposium on Fluid Power, Tokyo Institute of Technology, **1**, pp. 345–351.

[7] Bobusch, B., Woszidlo, R., Bergada, J., Nayeri, C., and Paschereit, C., 2013, "Experimental Study of the Internal Flow Structures inside a Fluidic Oscillator," Experiments in Fluids, **54**(6), pp. 1–12.

[8] Raghu, S., 2013, "Fluidic Oscillators for Flow Control," Exp Fluids, **24**(2), pp. 1–11.

[9] Guyot, D., Paschereit, C. O., and Raghu, S., 2009, "Active Combustion Control Using a Fluidic Oscillator for Asymmetric Fuel Flow Modulation," International Journal of Flow Control, **1**(2), p. 12.

[10] Gregory, J. W., Sullivan, J. P., Raman, G., and Raghu, S., 2007, "Characterization of the Microfluidic Oscillator," AIAA Journal, **45**(3), pp. 568–576.

[11] Simoes, E. W., Furlan, R., Bruzetti Leminski, R. E., Gongora-Rubio, M. R., Pereira, M. T., Morimoto, N. I., and Santiago Aviles, J. J., 2005, "Microfluidic Oscillator for Gas Flow Control and Measurement," Flow Measurement and Instrumentation, **16**(1), pp. 7–12.

[12] John, J. E. A., and Keith, T. G., 2006, *Gas Dynamics*, Pearson Prentice Hall, Upper Saddle River, N.J.

[13] Thompson, R., 1970, "Supersonic Fluidics Empirical Design Data," *Fourth Cranfield Fluidics Conference*, British Hydromechanics Research Association, Turin, Italy, pp. 17–39.

[14] Hiroki, F., Yamamoto, K., and Nasuda, T., 1993, "Fluidic Oscillator Using a Supersonic Bistable Device and Its Oscillation Frequency," Journal of Fluid Control, **21**(4), pp. 28–47.

[15] Xu, S., 2018, "Experimental Investigation of a Bi-Stable Supersonic Fluidic Oscillator," M.A.Sc. Thesis - Mechanical Automotive and Materials Engineering, University of Windsor.

[16] "9470K47 Oil-Resistant Aramid/Buna-N Gasket Material, 30" x 60" Sheet, 1/64" Thick | IBS Electronics," IBS Store Component Division [Online]. Available:

http://www.ibselectronics.com/ibsstore/9470k47-mcmaster-oil-resistant-aramid-buna-n-gasket-material-30-x-60-sheet-1-64-thick.html. [Accessed: 24-Mar-2019].

[17] Singh Sidhu, L., 2019, "Comparison of Hybrid Multi-Dimensional Models of a Bi-Stable Load-Switched Supersonic Fluidic Oscillator Application," M.A.Sc. Thesis - Mechanical Automotive and Materials Engineering, University of Windsor.

[18] "High Accuracy Pressure Transducers | Liquid Pressure and High Accuracy" [Online]. Available: https://www.omega.com/pptst/PX409_Series.html. [Accessed: 24-Mar-2019].

[19] Lindstrom, M., 2016, "How Impedance Relationships Influence Measurement Results, Document."

[20] "Introduction to Piezoelectric Force Sensors," Introduction to Piezoelectric Force Sensors [Online]. Available: http://www.pcb.com/Resources/Technical-Information/Tech_Force. [Accessed: 02-May-2019].

[21] "Field Wiring and Noise Considerations for Analog Signals - National Instruments, 2008," National Instruments Support [Online]. Available: http://www.ni.com/product-documentation/3344/en/. [Accessed: 14-May-2019].

[22] ElectronicsTutorials, 2019, "Active Band Pass Filter - Op-Amp Band Pass FilterBasic Electronics Tutorials," Active Band Pass Filters [Online]. Available: https://www.electronics-tutorials.ws/filter/filter_7.html. [Accessed: 03-May-2019].

[23] Young, H. D., Freedman, R. A., Ford, A. L., Sears, F. W., and Zemansky, M. W., 2014, *Sears and Zemansky's University Physics: With Modern Physics : Technology Update*, Pearson, 1301 Sansome Street, San Francisco, CA, 94111.

[24] "Quick Disconnect Thermocouples with Miniature Connectors | Omega Engineering," OMEGA [Online]. Available: https://www.omega.com/en-us/sensors-and-sensing-equipment/temperature/sensors/thermocouple-probes/jmqss/p/TMQSS-125E-6. [Accessed: 14-May-2019].

[25] "Type T Thermocouple - Type T Thermocouples - T Type Thermocouple - T Type Thermocouples" [Online]. Available: https://www.thermocoupleinfo.com/type-t-thermocouple.htm. [Accessed: 25-May-2019].

[26] "What Is a Thermocouple and How Does It Work? | Omega Engineering | Omega Engineering, 2018," Thermocouple Sensors [Online]. Available: https://www.omega.ca/en/resources/thermocouples. [Accessed: 14-May-2019].

[27] "Thermocouple Response Time," Thermocouple Response Time [Online]. Available: https://www.omegaeng.cz/temperature/Z/ThermocoupleResponseTime.html. [Accessed: 14-May-2019].

[28] "NI 6356 Device Specifications - National Instruments, 2016" [Online]. Available: http://www.ni.com/pdf/manuals/374452c.pdf.

[29] "USB-TC01 Specifications - National Instruments" [Online]. Available: http://www.ni.com/pdf/manuals/374918b.pdf.

[30] "Compressed Sheet - High Performance Compressed Aramid Fibre Blend With Buna-N Nitrile Binder," Phelps [Online]. Available: http://www.phelpsweb.com/phel7010.htm. [Accessed: 03-Mar-2019].

[31] Sidhu, L., Peirone, C., Xu, S., and Rankin, G., 2019, "Comparison of Hybrid Multi-Dimensional Numerical Models of a Bi Stable Load Switched Supersonic Fluidic

Oscillator Application," *Hefat_2019 Conference*, Hefat_2019 Conference Paper, Wicklow, Ireland, pp. 1–6.

[32] Mott, R. L., 2004, *Machine Elements in Mechanical Design,* Pearson/Prentice Hall, Upper Saddle River, N.J.

[33] "ANSI External Screw Threads Size Tolerances Chart - Engineers Edge" [Online]. Available: https://www.engineersedge.com/screw_threads_chart.htm. [Accessed: 17-Jul-2018].

[34] "NPT Thread Dimensions" [Online]. Available: http://www.amesweb.info/Screws/NPT_National_Taper_Pipe_Threads.aspx. [Accessed: 30-May-2018].

[35] "Torque vs Tension Bolts Table Chart SAE J429 Bolts | Engineers Edge, 2000" [Online]. Available: https://www.engineersedge.com/hardware/torque_vs_tension_bolts_13355.htm. [Accessed: 23-Mar-2019].

[36] "Loaded Flat Plates" [Online]. Available: http://www.roymech.co.uk/Useful_Tables/Mechanics/Plates.html. [Accessed: 23-Mar-2019].

[37] Rego Products, "Relief Valves for Gas and Cryogenic Systems 9400 Series Brass or Stainless Steel, Non-ASME," Rego Products [Online]. Available: http://www.regoproducts.com/cryoproductpdfs/9400.pdf.

[38] Doebelin, E. O., 2007, *Measurement Systems: Application and Design*, McGraw-Hill, India.

[39] Noether, G. E., 1955, "Use of the Range Instead of the Standard Deviation," Journal of the American Statistical Association, **50**(272), pp. 1040–1055.

Appendix A: SFO Test Facility Design Details

This section focuses on: the safety factors for mounting the SFO blocks together using UNC Grade 8 bolts, the safety factor of the thickness of the SFO to prevent rupture of the device upon pressurization, the flow capabilities of the pressure relief valves, the frequency responses for the piezoresistive and piezoelectric pressure sensors that are not flush mounted as well as the response times for the T-Type thermocouples.

A.1: Bolt Stress and Load Analysis:

A number of 3/8-16 UNC Grade 8 bolts are used to fasten the two SFO blocks. A necessary length of thread, determined by Equation A.1 is used when the nut material, in this case 6061-T6 Aluminum, is weaker than the bolt material [32–34].

$$L_e = \frac{S_{utB}(2A_{tB})}{S_{utN}\pi OD_{Bmin}[0.5+0.57735n(OD_{Bmin}-PD_{Nmax})]} \tag{A.1}$$

where:
S_{utB} = Ultimate tensile strength of the bolt material
S_{utN} = Ultimate tensile strength of the nut material
OD_{Bmin} = Minimum outside diameter of the bolt threads
PD_{Nmax} = Maximum pitch diameter of the nut threads
n = Number of threads per inch

If the values are as follows: S_{utB} = 150 ksi, S_{utN} = 45 ksi, OD_{Bmin} = 0.361", PD_{Nmax} = 0.3401", n = 16, and A_{tB} = 0.0775 in². A thread length of 16.69 mm (0.657") will ensure that the thread strengths for the aluminum will equal that of the bolt strength. The actual value used in the experiment is 19.05 mm (0.750").

A bolt spacing of 29.96 mm (1.18 inches) around the perimeter of the SFO is chosen to prevent leaking between the bolts. 131 bolts are placed around the perimeter of the SFO. The overall front view surface area of the SFO is 1492 cm² (231 in²). With a maximum pressure of 3.999 MPa (580 psig), the force exerted on the surface area,

attempting to pry the two blocks apart, is 596.0 kN (133980 lbf). A predetermined torque

for each bolt has been selected as 215 in-lbs. The preload from each bolt is determined

using Equation A.2 [35] where T is the torque in in-lbs, K is a constant (0.20) for plain

and dry conditions and D is the nominal diameter of the bolts (3/8").

$$F = \frac{T}{KD} = 12.575 \; kN \; (2827 \; lbs) \qquad \qquad (A.2)$$

Balancing the forces in the vertical direction is shown in Figure A.1.
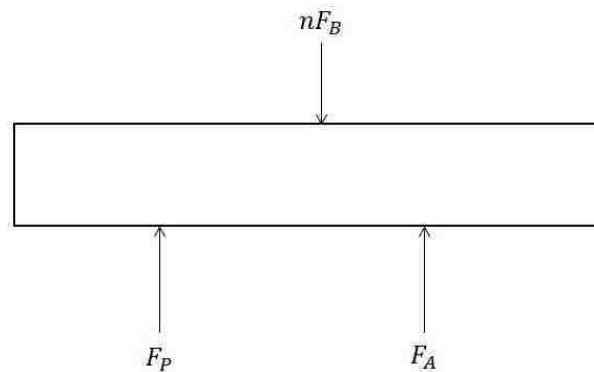
Figure A.1: Free body diagram of a plate used to determine bolt loads

where:
n = Number of bolts (131)
F_B = The preload on each bolt (lbs)
F_P = The force due to the pressure (lbs)
F_A = The resulting load between the two blocks (lbs)

Balancing the forces in the vertical direction and setting them to zero yields a

value of $F_A = 10514 \; kN \;\; (236357 \; lbs)$. When the SFO is fully pressurized, a

compressive load of 1051.4 kN (236357 lbf) is present which is expected to prevent

excessive leaking. The allowable stress (σ_a) on each bolt is 75% of the proof load [32].

The proof load for grade 8 bolts is 120 ksi [32] therefore $\sigma_a = 6205 \; MPa \; (90\,000 \; psi)$.

The actual stress on each bolt (σ_B) is:$\sigma_B = \frac{F_B}{A_{tB}} = 252 \; MPa \; (36477 \; psi)$ and the safety

factor for each bolt while assuming an evenly distributed load is therefore $SF = \frac{\sigma_a}{\sigma_B} =$

2.47.

A.2: Determining the Allowable Thickness of the SFO

The minimum thickness of the aluminum is the thickness of the sides at the SPF chambers. Two methods of estimation are used assuming different connections: edge clamped connection and simply supported [36]. For edge clamped, Figure A.2 depicts the dimensions of interest and the formula for stress is Equation A.3. The "a" is the largest length of the surface area exposed to the uniform load "P", "b" is the smallest length, "t_r" is the minimum required thickness of the plate and "σ_y" is the yield strength of 6061 T6 aluminum [32].
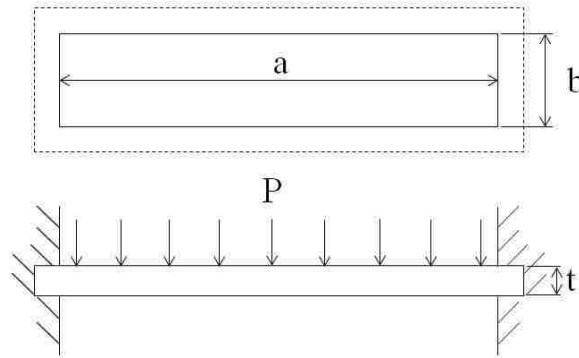
Figure A.2: Free body diagram of a plate bending with an edged clamp support

$$\sigma_y = \frac{Pb^2}{2t_r{}^2 \left[0.623\left(\frac{b}{a}\right)^6 + 1\right]} \tag{A.3}$$

Rearranging Equation A.3 to solve for the required thickness gives:

$$t_r = \sqrt{\frac{Pb^2}{2\sigma_y \left[0.623\left(\frac{b}{a}\right)^6 + 1\right]}} \tag{A.4}$$

The SPF chambers are not rectangular shaped, thus, the largest edge to edge dimensions are used for "a" and "b". With $a = 358.4x10^{-3}m$, $b = 236.1x10^{-3}m$, $P = 3.999 * 10^6 Pa$, and $\sigma_y = 276x10^6 Pa$, the thickness is $t_r = 0.0196m = 19.6\ mm$

Using a thickness of 43.07 mm in the SFO experiment gives the actual stress is determined from Equation A.3. This gives $\sigma_a = 24.6 * 10^6\ Pa$ and the safety factor, using the edged clamp assumption, as $SF = \frac{\sigma_y}{\sigma_a} = 11.2$.

Figure A.3 shows the edged clamped assumption with the same variables "a" and "b". Equation A.5 is used to determine the yield stress.
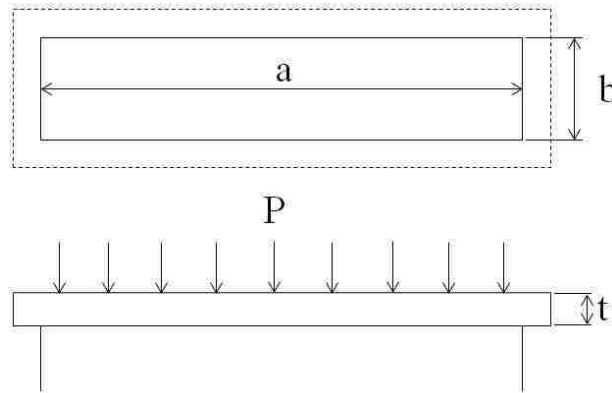
Figure A.3: Free body diagram of simply supported beam

$$\sigma_y = \frac{0.75Pb^2}{t_r{}^2\left[1.61\left(\frac{b}{a}\right)^3+1\right]} \tag{A.5}$$

Solving for the thickness from Equation A.5 gives $t_r = 0.0203\ m = 20.3\ mm$

Using the actual thickness in Equation A.4 gives the actual stress as $= 61.7x10^6\ Pa$ and a safety factor of $SF = \frac{\sigma_y}{\sigma_a} = 4.47$.

The actual thickness is acceptable for both assumptions. The smallest safety factor of 4.47 is for the simply supported assumption.

A.3: Verification of the PRV9434 450 PSI Pressure Relief Valves

The pressures in the SPF chambers are regulated by relief valves set at a pressure of 3.403 MPa (450 psig). The maximum supply pressure used in the experiment is 3.971 MPa (576 psig). The mass flow rate is calculated using the choked nozzle condition given by Equation A.6 [12]:

Operating conditions:

$P_o = 590.7\ psia = 3.971\ x\ 10^6\ Pa$
$R = 297\ \frac{J}{kgK}$
$T_o = 22°C = 295\ K$
$A^* = 3.2\ x\ 10^{-6}m^2$
$k = 1.4$
$P_{atm} = 101325\ Pa$

$$\dot{m} = P_o A^* \sqrt{\frac{k}{RT_o}} \left[\frac{k+1}{2}\right]^{\frac{k+1}{2(1-k)}} \tag{A.6}$$

For air or Nitrogen, Equation A.6 gives $\dot{m} = 0.0294\ \frac{kg}{s}$ and a required volume flow rate

of $Q_{req} = \frac{\dot{m}RT_o}{P_{atm}} = 0.0254\ \frac{m^3}{s} = 53.82\ SCFM$.

The PRV 9434 relief valve has been selected for the experiment. The volume flow rate capability of the relief valves are provided by the manufacturer [37] as being equal to 0.783 SCFM Air/PSIA at 110% of set pressure. For our case this is 400 $SCFM$. Since $Q_{valve} \gg Q_{req}$ the selected relief valves are acceptable for r the maximum pressure in the SPF chambers.

A.4: Error in the Feedback Tank Pressure Readings Due to Non-Flush Mounting

The non-flush mounting of the feedback tank pressure transducers consists of a cross-sectional geometry shown in Figure A.4. The volume of the channel and gap, shaded in grey, are $V_{gap} = 854\ mm^3$ and $V_{ch} = 434.5\ mm^3$. Since the volume of the channel is not small relative to the volume of the gap, compressibility in the channel is significant and the following analysis applies [38].
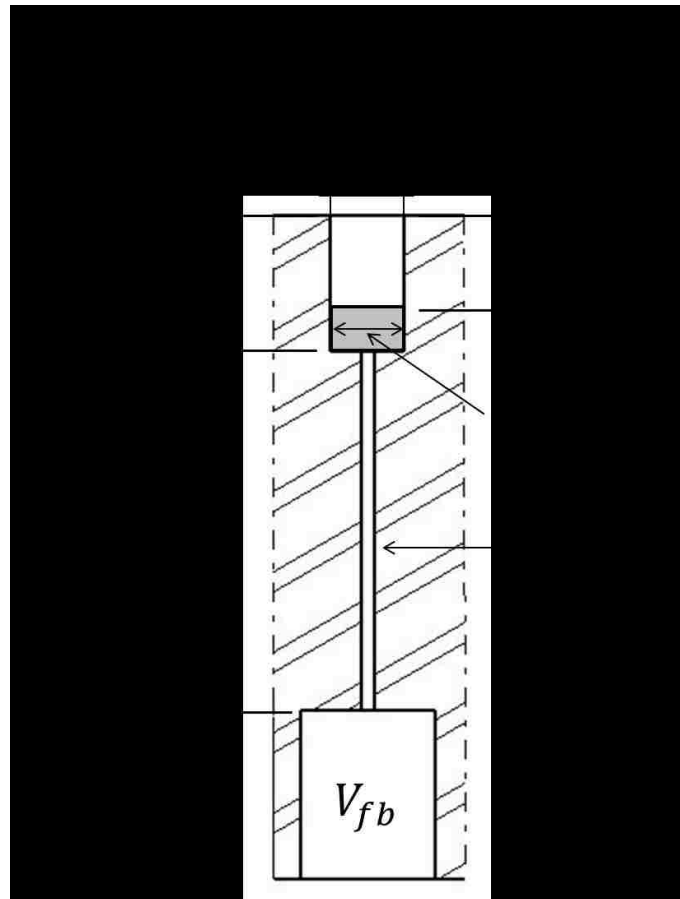
Figure A.4: Cross-sectional profile of the non-flush mounted pressure transducers in the feedback tanks

The standard form of the second order system is,

$$\frac{1}{\omega_n^2} \ddot{P}_m + \frac{2\xi}{\omega_n} \dot{P}_m + P_m = P_{fb}(t) \tag{A.7}$$

where:

ω_n = the natural frequency $(rads/s)$,
ξ = the damping factor,
P_m = the measured pressure, and
$P_{fb}(t)$ = the pressure in the feedback tanks.

For a sine input wave, the exact solution to Equation A.7 is given by

$$\frac{P_m}{P_{fb}} = \frac{1}{\sqrt{\left[1-\left(\frac{\omega}{\omega_n}\right)^2\right]^2 + \left(2\xi\frac{\omega}{\omega_n}\right)^2}} \tag{A.8}$$

where the natural frequency is given as

$$\omega_n = \frac{a}{L\sqrt{(1/2) + \left(V_{gap}/V_{ch}\right)}} \tag{A.9}$$

and the damping factor is

$$\xi = \frac{16\mu L}{d^2 \rho a} \sqrt{(1/2) + \left(V_{gap}/V_{ch}\right)} \tag{A.10}$$

In these equations, a = speed of sound, μ = dynamic viscosity and ρ = density. If $\gamma = 1.4$, $R = 297 \frac{J}{kg \cdot K}$ and $T = 295\ K$ the speed of sound $a = 350\ \frac{m}{s}$. Further, using these values along with d=0.0032 m, L=0.0549 m, $\mu = 1.76x10^{-5}\ \frac{N \cdot s}{m^2}$ and $\rho = 1.162\ \frac{kg}{m^3}$.

From Equations A.9 and A.10, it is found that, $\omega_n = 4060\ \frac{rad}{s} = 646$ Hz, and $\xi = 0.0055$. Using these values in Equation A.8 gives the ratio of the actual amplitude to the measured amplitude as 1.0015 for a frequency of 25 Hz, and 1.025 for 100 Hz. The amplitudes measured are slightly higher than the actual amplitudes with a maximum difference of 2.5% at a frequency of 100 Hz, which is considered to be acceptable.

A.5: Fundamental Frequency for Mounting the PCB® 113B28 Sensors

Figure A.5 shows the relevant geometric parameters used for this analysis. Since the face of the pressure sensor is at the top of the 24 mm dimension, the system acts as a closed-end tube in which only odd numbered harmonics are possible [23]. For the first harmonic, the fundamental frequency is proportional to the velocity over the wave length [23]. The velocity is the speed of sound and the wavelength is always 4 times the length of the channel for a stopped tube [23]. The fundamental frequency can then be written as

$$f_1 = \frac{a}{4L} = \frac{\sqrt{\gamma RT}}{4L} \qquad . \tag{A.11}$$
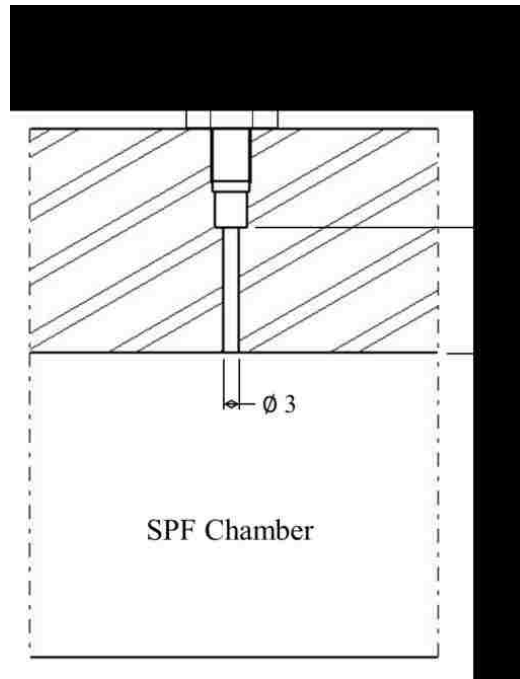
Figure A.5: Non-flush mounted PCB pressure sensors

For a length of 0.024 meters, room temperature and N_2 as the medium, the fundamental frequency is then equal to 3648 Hz. The mounting technique is acceptable for capturing the expected frequencies of oscillation.

A.6: Verification of T-Type Thermocouple Response Time

The T-Type thermocouples provide an accuracy of +/- 0.5 $^{\circ}$C, thus, they are not capable of measuring the small temperature fluctuations caused by the small pressure fluctuations. However, the thermocouples are sufficiently accurate for capturing the temperature increase due to the overall pressure increase during the filling process. A graph of the thermocouple time responses is provided by OMEGA^{TM} [27] which shows the time constant is a function of the bare wire diameters. In addition, the thermocouple bare wires are measured with a vernier caliper and the diameters found to be approximately 0.76 mm (0.03") in diameter, which results in a time constant of approximately 1.7 seconds. This time constant is small compared to the times required to fill the SPF chambers and hence is acceptable.

Appendix B: Uncertainty Analysis

This section covers the uncertainties due to the A/D converter, the piezoresistive pressure transducers, the piezoelectric pressure sensors, an example of the method to determine the pressure amplitudes measured by the piezoresistive pressure sensors as well their precision errors, the uncertainty in the temperature measurements and the uncertainties for all non-dimensional parameters. This section refers to the right and left sides of the SFO as shown in Figure B.1.
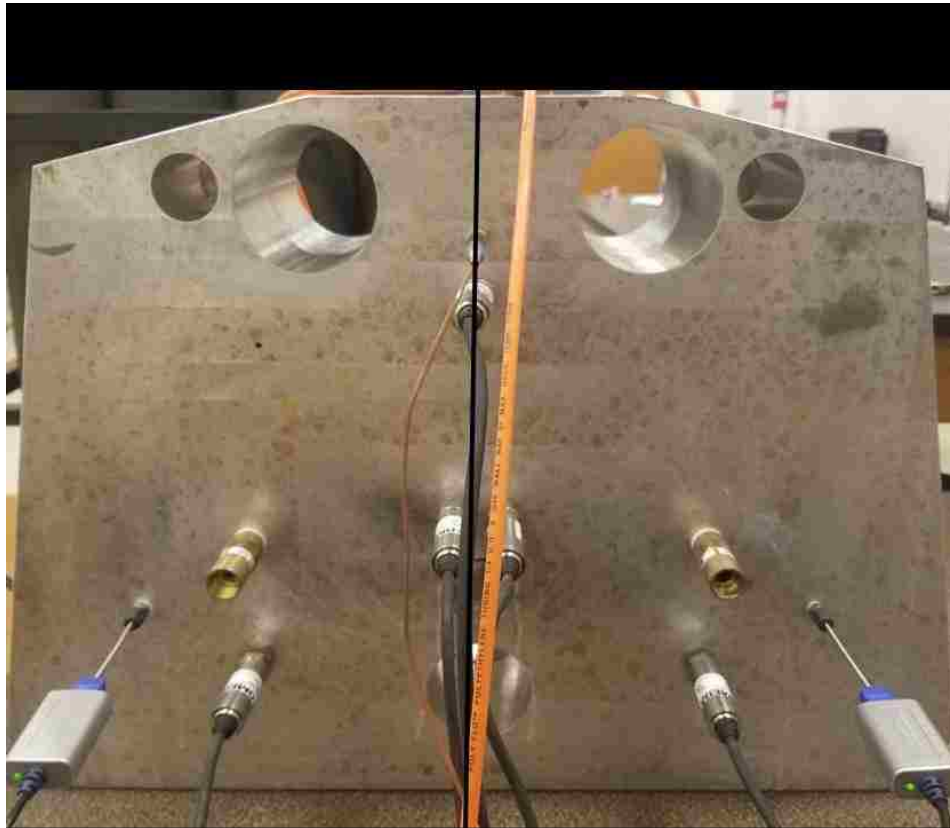
Figure B.1: Left and right side of the SFO

B.1: NI 6356 A/D Converter:

The following information regarding uncertainty determination is obtained from the NI

6356 A/D converter manual available on the National Instruments website [28]. The

nomenclature is provided as follows, for convenience.

Nomenclature for Analog Input:
A_{cc} = Absolute accuracy
GE = Gain error
GT = Gain Output-voltage temperature coefficient
INL_{err} = Least significant bit error
OE = Offset error
OT = Offset temperature coefficient
RA = Range
RD = Reading
RT = Reference Output-voltage coefficient due to temperature change
RGE = Residual gain error
ROE = Residual offset error
ΔT_{LEC} = Temperature change from last external calibration
ΔT_{LIC} = Temperature change from last internal calibration
Absolute Accuracy:

$$A_{cc} = RD * GE + RA * OE \qquad (B.1)$$

where:

$$GE = RGE + GT * \Delta T_{LIC} + RT * \Delta T_{LEC} \qquad (B.1.1)$$

$$OE = ROE + OT * \Delta T_{LIT} + INL_{err} \qquad (B.1.2)$$

Constants provided by national instruments are [28]: $GT = 8\ ppm/°C$, $RT =$

$5\ ppm/°C$, $ROE = 15\ ppm\ of\ RA$, $INL_{err} = 46\ ppm\ of\ RA$, $number\ of\ bits = 16$.

Assumptions provided by the manufacturer are $\Delta T_{LEC} = 10°C$ and $\Delta T_{LIC} = 1°C$.

B.2: Piezoresistive Pressure Transducers

The five piezoresistive pressure transducers use a nominal full-scale range of $(0V)$ – $(+5V)$ and the following absolute accuracy analysis applies. As mentioned previously, the variables provided by National Instruments for the data acquisition are $RGE = 120 \frac{ppm}{RD}, RA = 5\,V, OT = 36ppm * RA, GE = 178\,\frac{ppm}{RD}, OE = 97\,\frac{ppm}{RA}, A_{cc} = (178 * RD + 485)\mu V$ and $\frac{EMS}{2^{bits}} = 0.76\,\mu V = $ resolution.

Since the $Resolution \ll A_{cc}$, resolution is neglected in determining the uncertainty contribution of the A/D converter to the piezoresistive pressure transducer readings.

The sensitivities $(\partial P/\partial V)$ for all of the piezoresistive pressure transducers are represented in $psi/Volts$, thus, the uncertainty for the piezoresistive pressure transducers due to the A/D converter, in psi, is $U_{A/D} = \left(\frac{\partial P}{\partial V}\right) * A_{cc} = \left(\frac{\partial P}{\partial V}\right)(178 * RD + 485V)x10^{-6}$.

DAQ Accuracy for Supply Pressure:

For Part #: PX409-1.0kG5V-XL, Model #: 487682 $\frac{\partial P}{\partial V} = 199.96\,\frac{psi}{V}$.

At full scale, the uncertainty of the supply pressure readings, due to the A/D converter is $U_{FS} = \frac{\partial P}{\partial V} A_{cc} = 199.96\frac{psi}{V} * (178 * 5V + 485V)x10^{-6} = \pm0.275psi$.

Converting all voltage into psi via the sensitivity gives the following:

$U_{A/D} = 178 * 10^{-6} * RD^* + 0.097psi$ where $RD^* = \frac{\partial P}{\partial V} * RD$.

Thus, RD^* is the reading in psig obtained via LabVIEW.

Table B.1 below shows the uncertainty for all piezoresistive pressure transducers due to the uncertainty in the A/D converter corresponding to their location on the SFO.

The sensitivity is in psi/V, U_{FS} is the uncertainty at full-scale in psi and $U_{A/D}$ is the overall uncertainty equations used for each measurement observed.

Table B.1: Uncertainty in Piezoresistive Transducers due to the A/D converter

Location	Full scale reading (V)	$\partial P/\partial V$	U_{FS}	$U_{A/D}$
Supply Chamber	5V	199.96	0.276	$178x10^{-6} * RD^* + 0.097\ psi$
Right Feedback	5V	201.65	0.278	$178x10^{-6} * RD^* + 0.098\ psi$
Left Feedback	5V	201.01	0.277	$178x10^{-6} * RD^* + 0.097\ psi$
Right Exhaust	5V	100	0.138	$178x10^{-6} * RD^* + 0.049\ psi$
Left Exhaust	5V	99.98	0.138	$178x10^{-6} * RD^* + 0.049\ psi$

The design stage uncertainty of the piezoresistive pressure transducers also includes a contribution due to its manufacturer's specifications. The following is a description of how that information is included for the transducers located in the supply pressure tank. Values for the other transducers are tabulated for ease of the reader. All variables used are provided by the manufacturer and $\frac{\partial P}{\partial V} = \frac{1000\ psi}{5.001\ V} = 199.96\ \frac{psi}{V}$.

The resolution of the sensor is 0.001 psi. Recalling that the uncertainty from the A/D converter is represented by the following equation for the supply chamber pressure: $U_{A/D} = 178x10^{-6} * RD^* + 0.097\ psi$.

For linearity: $e_L = 0.0003$ and $U_L = \pm \frac{\partial P}{\partial V} FSO * e_L = \pm 0.300\ psi$.

For accuracy: $U_{Acc} = \pm \frac{\partial P}{\partial V} FSO * Acc = \pm 0.500\ psi$

For repeatability: $U_{rep} = \pm 0.08\%\ FSO = \pm 0.800\ psig$

The instrumentation uncertainty is then $U_c = \pm \sqrt{(U_{A/D})^2 + (U_L)^2 + (U_{acc})^2 + (U_{rep})^2}$

or $U_c = \pm \sqrt{(178x10^{-6} * RD^* + 0.097\ psi)^2 + 0.98\ psi^2}$.

The zero order uncertainty is $U_o = \pm\frac{1}{2}(0.001\ psi) = \pm0.0005\ psi$ which gives the

overall design uncertainty as $U_d = \sqrt{(U_c)^2 + (U_o)^2}$

or $U_d = \pm\sqrt{(178x10^{-6} * RD^* + 0.097\ psi)^2 + 0.98\ psi^2}$.

Table B.3 includes the overall design uncertainties for all piezoresistive pressure

transducers corresponding to their locations placed on the SFO.

Table B.2: Overall Design Uncertainties for the Piezoresistive Transducers

Location	U_d
Supply Chamber	$\sqrt{(178x10^{-6} * RD^* + 0.097\ psi)^2 + 0.980\ psi^2}$
Right Feedback	$\sqrt{(178x10^{-6} * RD^* + 0.098\ psi)^2 + 0.980\ psi^2}$
Left Feedback	$\sqrt{(178x10^{-6} * RD^* + 0.097\ psi)^2 + 0.980\ psi^2}$
Right Exhaust	$\sqrt{(178x10^{-6} * RD^* + 0.049\ psi)^2 + 0.245\ psi^2}$
Left Exhaust	$\sqrt{(178x10^{-6} * RD^* + 0.049\ psi)^2 + 0.245psi^2}$

B.3: Piezoelectric Pressure Sensors

To obtain the best accuracy using the DAQ a voltage range of (-1V) to (+1V) is

selected for the two piezoelectric pressure sensors, due to the low range use of expected

pressure readings. The following absolute accuracy analysis applies with $RGE =$

$138\frac{ppm}{RD}$, $RA = 1V$, $OT = 50ppm * RA$, $GE = 196\frac{ppm}{RD}$, $OE = 111\frac{ppm}{RA}$ and $A_{cc} =$

$(196 * RD + 111\ \mu V)$. RD is the dynamic reading of the pressure sensors in Volts. The

following example is for the right SPF chamber. After which, a conclusion is made for

the uncertainty of the left SPF chamber due to the A/D converter. With $\frac{\partial P}{\partial V} = 9.833\ \frac{psi}{V}$

, at full scale, the uncertainty of right SPF chamber pressure amplitude reading, due to the

A/D converter is $U_{A/D} = \frac{\partial P}{\partial V}A_{cc} = 0.003\ psi$. This accuracy applies to an amplitude

pressure reading of 9.833 psi. The high end pressure amplitude predicted by the

numerical model is 0.75 psi, which would result in a voltage reading of 0.076 V. The

accuracy of the predicted maximum pressure amplitude is then, $U_{A/D} = \frac{\partial P}{\partial V} A_{cc} =$

$0.001\ psi$

The low end pressure amplitude predicted by the numerical model is 0.02 psi, which

would result in a voltage reading of 0.002 V. The accuracy of the predicted minimum

pressure amplitude is then $U_{A/D} = \frac{\delta P}{\delta V} A_{cc} = 0.001\ psi$. In conclusion, for the expected

range of pressure amplitudes in the right SPF chamber, the accuracy of the A/D converter

remains approximately at 0.001 psi since $U_{A/D} \approx 0.001\ psi$ as $RD \to 0V$.

The left SPF chamber piezoelectric sensor has a sensitivity of 9.434 psi/V and the

uncertainty due to the A/D converter is the same as the right SPF chamber's piezoelectric

sensor. If the amplitudes captured are greater than 5.17 kPa (0.75 psi), the A/D

converter's uncertainty will be revaluated accordingly.

The SPF chamber pressure amplitude measurements are obtained using the piezoelectric

pressure sensors. The uncertainty due to the A/D converter is the same for all cases,

$U_{A/D} = \pm 0.001\ psi$.

The following information is provided from the calibration data sheets for the sensors

with a full scale reading of 5.0 psig: $\frac{\partial P}{\partial V} = 9.434\ \frac{psi}{V}$, $FSO = 5\ psi$, $e_L = 0.004$ and $U_L =$

$\pm e_L FSO = 0.02\ psi$.

The linearity for the range of 0-5V is provided with a resolution of 0.01 psig (2 decimal

places in the calibration data sheet). As a result, considering a resolution of 0.001psig, an

uncertainty of ± 0.005 must be considered, thus the error due to linearity is $U_L =$

$\pm \sqrt{(0.02\ psi)^2 + (0.005\ psi)^2} = 0.021\ psi$.

Since $U_o = \pm 0.0005\ psi$, $U_{A/D} = \pm 0.001\ psi$ and $U_c = \pm\sqrt{U_L{}^2 + U_{A/D}{}^2} = \pm 0.021$ psi.

For all piezoelectric sensors, the calibration data sheet states that the accuracy is 1% of each individual reading. Thus, $Z_{v,95}P = \pm 0.01 * RD^*$ and since, $U_d =$

$$\pm\sqrt{U_c{}^2 + U_o^2 + \left(Z_{v,95}P\right)^2} = \pm\sqrt{(0.021\ psi)^2 + (0.01 * RD^*)^2}.$$

For the left SPF chamber, the linearity is given as 0.1% for a full scale reading of 5 psi and the uncertainty is $U_L = \pm\ 0.0071\ psi$. Therefore, it can be shown that $U_c =$

$$\sqrt{(0.0071\ psi)^2 + (0.001\ psi)^2} = \pm 0.0071\ psi \text{ and hence } U_d =$$

$$\pm\sqrt{(0.0071\ psi)^2 + (0.01 * RD^*)^2}.$$

The uncertainty in the right SPF chamber is significantly greater than the uncertainty in the left SPF chamber. The sensor in the left SPF chamber is used but a comparison of the right and SFO measurements is shown in Appendix C.2.

All the design uncertainties are for single measurements. The method for determining the amplitudes for a given SPF chamber pressure and supply pressure are determined as a mean over N number of cycles. Each cycle contains two maximums and one minimum peak point. The example shown here is for the piezoelectric pressure sensor on the left side of the SFO. The same method is used for the feedback tank amplitudes; however, each reading is evaluated at the true pressure reading due to the characteristics of the piezoresistive pressure transducers. The amplitude for each cycle is determined using Equation B.3.1 for a cycle "k".

$$\bar{P}_{amp,k} = \frac{P_{i,max} - P_{i,min} + P_{i+1,max} - P_{i,min}}{2} \tag{B.3.1}$$

Figure B.3 provides a pictorial description of the measurements. The process leading up to the figure below is shown using a MATLAB code in Appendix C.1.
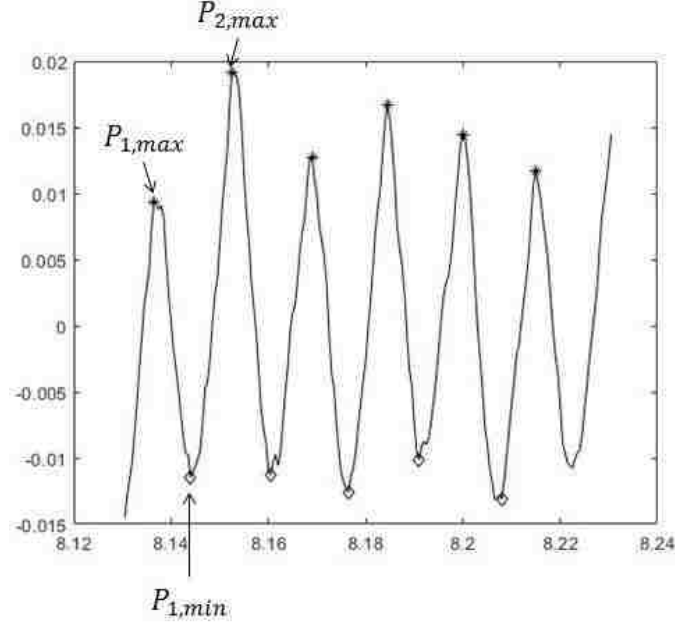
Figure B.2: Determining the average amplitude of each cycle

The uncertainty in the average amplitudes of each cycle is Equation B.4:

$$U_{\bar{P}_{amp,k}} = \sqrt{\left(\frac{\partial \bar{P}_{amp,k}}{\partial P_{i,max}} U_P\right)^2 + \left(\frac{\partial \bar{P}_{amp,k}}{\partial P_{i+1,max}} U_P\right)^2 + 2\left(\frac{\partial \bar{P}_{amp,k}}{\partial P_{i,min}} U_P\right)^2} \tag{B.4}$$

For all cases:

$$\frac{\partial \bar{P}_{amp,k}}{\partial P_{max\,or\,min}} = \frac{1}{N}$$

where N is always 2 and the uncertainty in each average is thus:

$$U_{\bar{P}_{amp,k}} = \sqrt{\left(\frac{U_{P_{max,i}}}{2}\right)^2 + \left(\frac{U_{P_{max,i+1}}}{2}\right)^2 + 2\left(\frac{U_{P_{min,i}}}{2}\right)^2} \tag{B.5}$$

As stated above, several cycles are being evaluated for each back pressure; the ranges of cycles are determined over a 0.1 second interval where the midpoint is the time at the SPF chamber pressure. The average pressure amplitudes for each pressure then becomes Equation B.6:

$$\bar{\bar{P}}_{amp} = \frac{1}{N_{cycles}} \sum_{k=1}^{N_{cycles}} \bar{P}_{amp,k} \tag{B.6}$$

84

The uncertainty of the pressure amplitudes is Equation B.7:

$$U_{\bar{\bar{P}}_{amp}} = \sqrt{\sum_{k=1}^{N_{cycles}} \left(\frac{\partial \bar{\bar{P}}_{amp}}{\partial \bar{P}_{amp,k}} U_{\bar{P}_{amp,k}} \right)^2} \tag{B.7}$$

For all cases:

$$\frac{\partial \bar{\bar{P}}_{amp}}{\partial \bar{P}_{amp,k}} = \frac{1}{N_{cycles}}$$

Thus Equation B.8 is the uncertainty for the average of all average pressure amplitudes:

$$U_{\bar{\bar{P}}_{amp,cycles}} = \sqrt{\sum_{k=1}^{N_{cycles}} \left(\frac{U_{\bar{P}_{amp,k}}}{N_{cycles}} \right)^2} \tag{B.8}$$

In addition to the above uncertainty, a precision error must be taken into account for the variance of the average pressure readings for the back pressure. For small data sets Equation B.9 [39] shows the precision uncertainty of the mean amplitudes and Equation B.10 is the overall uncertainty all amplitudes displayed in the results section:

$$U_{\bar{\bar{P}}_{t,95\%}} = \frac{Range}{\sqrt{N_{cycles}}} \tag{B.9}$$

$$U_{P_{amp}} = \sqrt{\left(U_{\bar{\bar{P}}_{amp,cycles}} \right)^2 + \left(U_{\bar{\bar{P}}_{t,95\%}} \right)^2} \tag{B.10}$$

B.4: Frequency Determination

There is an uncertainty in each frequency measurement due to the time step, zero order uncertainty, and is proportional to the ratio of the time step over the period of oscillation:

$$\frac{W_{f_i}}{f_i} = \frac{W_t}{T_i} \tag{B.11}$$

$$W_{f_i} = f_i \frac{W_T}{T_i} = W_T \cdot f_i^2 \tag{B.12}$$

The time step is the inverse of the sampling frequency thus:

$$W_{f_i} = \frac{f_i^2}{f_s} \qquad \text{(B.13)}$$

Similar to the pressure amplitudes, the frequency calculated will be an average for a number of cycles.

$$\bar{f} = \frac{1}{N}\sum_{i=1}^{N} f_i \qquad \text{(B.14)}$$

$$W_{\bar{f}} = \sqrt{\sum_{i=1}^{N}\left(\frac{\partial \bar{f}}{\partial f_i} W_{f_i}\right)^2} \qquad \text{(B.15)}$$

For all cases:

$$\frac{\partial \bar{f}}{\partial f_i} = \frac{1}{N}$$

Thus, the uncertainty in the average frequencies measured is Equation (B.16):

$$W_{\bar{f}} = \sqrt{\sum_{i=1}^{N}\left(\frac{W_{f_i}}{N}\right)^2} \qquad \text{(B.16)}$$

The precision error and overall uncertainties is shown in Equations B.17 and B.18:

$$U_{\bar{f}_{t,95\%}} = \frac{Range}{\sqrt{N}} \qquad \text{(B.17)}$$

$$U_f = \sqrt{\left(W_{\bar{f}}\right)^2 + \left(U_{\bar{f}_{t,95\%}}\right)^2} \qquad \text{(B.18)}$$

B.5: Thermocouples

The T-Type thermocouple is connected to the NI 6356 A/D converter and the two T-Type thermocouples in the SPF chambers are connected to USB-TC01 A/D converters. The uncertainty analysis of the temperature readings follows:

86

B.5.1: Supply Temperature Measurements

The repeatability of the T-Type thermocouples is either $\pm0.5°C$ or 0.4% of the temperature in Celsius, whichever is the greater of the two [25]. The temperature ranges which are expected are approximately $10\ °C\ \leq T\ \leq 40°C$. Using the manufacturer's table [25], to obtain the sensitivity of the predicted reading yields the graph with a line of best fit shown in Figure B.3.
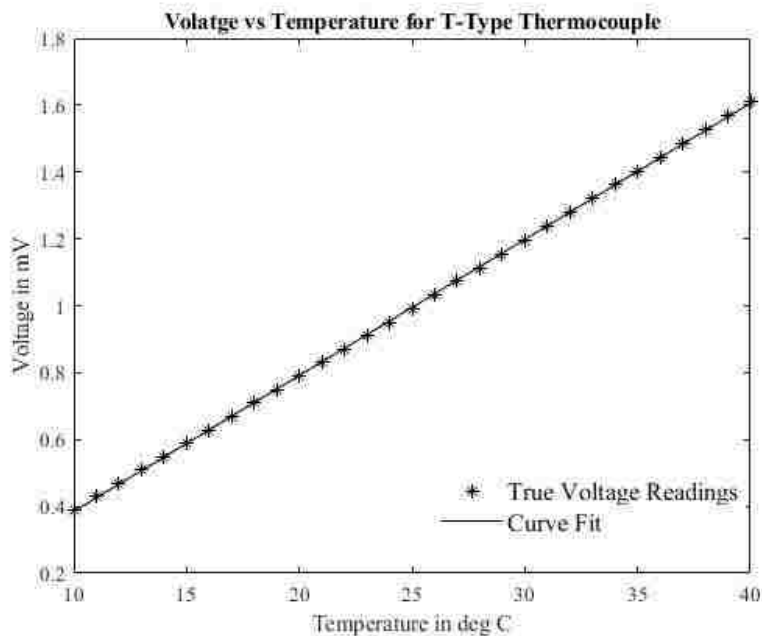
Figure B.3: Voltage vs Temperature for T-type thermocouples

The sensitivity for the thermocouples is:

$$\frac{\partial V}{\partial T} = \frac{4.069x10^{-6}V}{1°C}$$

or:

$$\frac{\partial T}{\partial V} = 24576\frac{°C}{V}$$

This will be used to determine the uncertainty for the T-Type thermocouple which is connected to the NI 6235 A/D converter, used to measure the supply temperature. For +/- 1V a reading, the possible temperatures measured range between -100 °C to 100 °C, the uncertainty is:

$$U_{A/D} = \left(\frac{\partial T}{\partial V}\right) * A_{cc} = \left(\frac{\partial T}{\partial V}\right)(178 * RD + 101.02V)x10^{-6} \qquad (B.19)$$

Where (RD) is the reading in volts and since the reading obtained in LabVIEW is in °C, similar to what was done with pressure let:

$$RD^* = \frac{\partial T}{\partial V} * RD = T \qquad (B.20)$$

For the range of expected temperatures, the repeatability of +/- 0.5°C is the largest and the design uncertainty becomes:

$$U_d = \pm\sqrt{\left(U_{A/D}\right)^2 + (U_r)^2} \qquad (B.21)$$

$$U_d = \pm\sqrt{\left(\frac{\partial T}{\partial V}(178 * RD + 101.02V)x10^{(-6)}\right)^2 + (0.5)^2}$$

Temperature readings of 10°C and 40°C result in voltage readings of 0.000790 Volts and 0.001612 Volts, thus:

$$U_{D/10°C} = \pm0.5°C$$

$$U_{D/40°C} = \pm0.5°C$$

For the expected temperature ranges, the uncertainty for the supply temperature remains constant.

B.5.2: SPF Chamber Temperatures Measurements

The thermocouples in the chambers are connected to USB-TC01 A/D converters. The approximate error over the expected temperature ranges, provided by National Instruments for a T-Type thermocouple, is approximately $\pm 0.5°C$ [29]. Thus:

$$U_d = \pm 0.5°C$$

The temperature uncertainty in the chambers is the same as the uncertainty in the supply temperature.

B.6: Non-dimensional Parameters

The uncertainty of the non-dimensional mean SPF chamber pressure, the non-dimensional SPF chamber pressure amplitude, the non-dimensional feedback tank pressure and the non-dimensional frequencies are described in this subsection.

B.6.1: Variation of Mean SPF Chamber Pressures

$$P_r = \frac{P_{b,abs}}{P_{s,abs}}$$

$$U_{P_r} = \pm \sqrt{\left(\frac{\partial P_r}{\partial P_b} U_{P_b}\right)^2 + \left(\frac{\partial P_r}{\partial P_s} U_{P_s}\right)^2} \qquad (B.22)$$

Recall that the back pressure (SPF chamber pressure) and the supply pressure uncertainties are shown in Table B.2. The uncertainty for the SPF chamber pressure ratio, shown in Equation B.22, is used to determine the horizontal error bar for all non-dimensional comparisons.

$$U_{P_r} = \pm \sqrt{\left(\frac{U_{P_b}}{P_{s,abs}}\right)^2 + \left(\frac{(P_{b,abs})U_{P_s}}{(P_{s,abs})^2}\right)^2} \qquad (B.23)$$

B.6.2: SPF Chamber Pressure Ampltitudes

The non-dimensional SPF chamber pressure amplitude is defined as: $\wp_{amp} =$

$\frac{P_{amp}}{P_{s,abs}}$. Since $U_{\wp_{amp}} = \pm\sqrt{\left(\frac{\partial\wp_{amp}}{\partial P_{amp}}U_{P_{amp}}\right)^2 + \left(\frac{\partial\wp_{amp}}{\partial P_{s,abs}}U_{P_s}\right)^2}$, therefore $U_{\wp_{amp}} =$

$\pm\sqrt{\left(\frac{U_{P_{amp}}}{P_{s,abs}}\right)^2 + \left(\frac{(P_{amp})U_{P_s}}{(P_{s,abs})^2}\right)^2}$.

B.6.3: Feedback Pressure Ampltitudes

The non-dimensional feedback tank amplitude is defined as $\wp_{Fb} = \frac{P_{Fb}}{P_{s,abs}}$. Since

the uncertainty is $U_{\wp_{Fb}} = \pm\sqrt{\left(\frac{\partial\wp_{Fb}}{\partial P_{Fb}}U_{P_{Fb}}\right)^2 + \left(\frac{\partial\wp_{Fb}}{\partial P_{s,abs}}U_{P_s}\right)^2}$, it follows that $U_{\wp_{Fb}} =$

$\pm\sqrt{\left(\frac{U_{P_{Fb}}}{P_{s,abs}}\right)^2 + \left(\frac{(P_{Fb})U_{P_s}}{(P_{s,abs})^2}\right)^2}$.

B.6.4: Frequencies

The non-dimensional frequency is defined as $\mathcal{F} = \frac{\rho V_{fb}f}{\dot{m}}$, Taking into account for

the formulas for density and mass flow rate, it can be shown that $\mathcal{F} = \frac{V_{fb}f}{A_t\sqrt{\gamma R T_s}}$ and $\mathcal{F} \propto$

$\frac{f}{\sqrt{T_s}}$. Since the uncertainty is $U_{\mathcal{F}} = \pm\sqrt{\left(\frac{\partial\mathcal{F}}{\partial f}U_f\right)^2 + \left(\frac{\partial\mathcal{F}}{\partial T_s}U_{T_s}\right)^2}$, it follows that $U_{\mathcal{F}} =$

$\pm\sqrt{\left(\frac{(V_{fb})U_f}{A_t\sqrt{\gamma R T_s}}\right)^2 + \left(\frac{(V_{fb}f)U_{T_s}}{2A_t\sqrt{\gamma R T_s^{\left(\frac{3}{2}\right)}}}\right)^2}$.

Appendix C: Programs and Results

An example of the %Leak results, a comparison of the left and right SFO results, dimensioned results of the repeatability test and the dimensioned results of the tests at various supply pressures is presented in this section.

C.1: Example of Obtaining Feedback Tank and SPF Chamber Amplitudes and Frequencies; Ps = 2.110 MPa (306 psig), Pb = 0.406 MPa (58.9 psig)

Since the transducers read pressure in psig, the results are displayed in psig accordingly using the MATLAB program and converted to the metric units afterwards. The metric results for all cases are shown in Appendix C.4 and Appendix C.5. The following example is used to obtain the frequency and amplitude in the feedback tank at the supply and back pressure case of interest. The following is a step by step procedure of what the code does:

1. The user inputs the back pressure in psig to analyze.

2. The code finds the index of that back pressure and this is used to find time and feedback pressures.

3. A time vector of 0.1 seconds is created with the time at the index stated above as the midpoint.

4. Feedback amplitudes are plotted versus time with initial max points. The user determines what, if any, max points should be eliminated.

5. A new graph of the final max points and initial min points is shown and the user determines what min points to eliminate. A new graph is plotted with the final max and min points.

6. For loops are used to determine the frequencies and amplitudes as well as their uncertainties and displayed as final answers, accordingly, using fprintf.

```matlab
A=csvread('C:\SFO - Experiment\Post Processing\Programs\Ps = 300
psig\300psig.txt');


t=A(:,1); %Time vector (s)
Ps=A(:,2); % Supply pressure (psi)
FB_R=A(:,3); % Right feedback tank pressure (psi)
FB_L=A(:,4); % Left feedback tank pressure (psi)
Ch_L=A(:,5); % Left chamber pressure from piezoresistive transducers
(psi)
Ch_R=A(:,6); % Right chamber pressure from piezoresistive transducers
(psi)
PCB_R=A(:,7); % Right chamber pressure from piezoelectric sensors (psi)
PCB_L=A(:,8); % Left chamber pressure from piezoelectric sensors (psi)



fs=(t(4)-t(3))^(-1); %Sampling Frequency

% fprintf('The sampling frequency is %2.0f Hz \n\n',fs)

points=50; %50 point moving average for the mean chamber pressure

Ch_LS=movmean(Ch_L,points);

%Finding the time at which the back pressure reaches the pressure of
%interest
n=input('Type the back pressure in psig to investigate')
% Type the back pressure in psig to investigate58.9

count=0;
%Finding the index in which the back pressure is reached, which will
later
%be used to determine the time and index of the feedback tank results
k=1;
while Ch_LS(k)<(n+1)
    if Ch_LS(k)<n
        k=k+1;
    else
        fprintf('%2.0fn is the index in the column vector where the
back pressure just reaches %2.0f psig\n\n',k,n);
        break
    end
end
%The time at which the back pressure is reached
t_n=t(k,1);

%Finding a time vector in which 0.05 seconds is before and after the
%selected back pressure is reached

%Finding a time interval of 0.05 seconds
points_05=fs*0.05;
```

```
%Time vector of 0.1 seconds with the time the back pressure is reached
as
%the midpoint
tv_n=t(k-points_05:k+points_05);

%Feedback vector resulting in the time vector discussed above
FB_Ln=FB_L(k-points_05:k+points_05);%Corresponding Feedback Tank
Amplitude

%Provides visual of the feedback tank ampltitude to ensure oscillation
is
%present
plot(tv_n,FB_Ln,'-k')
title(['Feedback Tank Pressure vs Time: Pb = ',num2str(n),' psig'])
xlabel('Time (s)')
ylabel('Feedback Tank Pressure (psig)')

%Finding the max peak locations
[Max,loc_Max]=findpeaks(FB_Ln,'MinPeakDistance',20);

%Using true or false logic to identify minimum peak locations
[Min_logical]=islocalmin(FB_Ln,'MinSeparation',20)';
%Finding the location and values for the true statements discussed
above
[Min_z,loc_Min]=find(Min_logical);

%Finding the times of the maximum and minimum peaks
tv_max=tv_n(loc_Max,1);
tv_min=tv_n(loc_Min,1);
Min=FB_Ln(loc_Min,1);

%Taking an initial look at the max peak points obtained above
plot(tv_n,FB_Ln,'-k',tv_max,Max,'*k')
title('Verifying Max and Min Points are Correct')
xlabel('Time (s)')
```

Verifying Max and Min Points are Correct
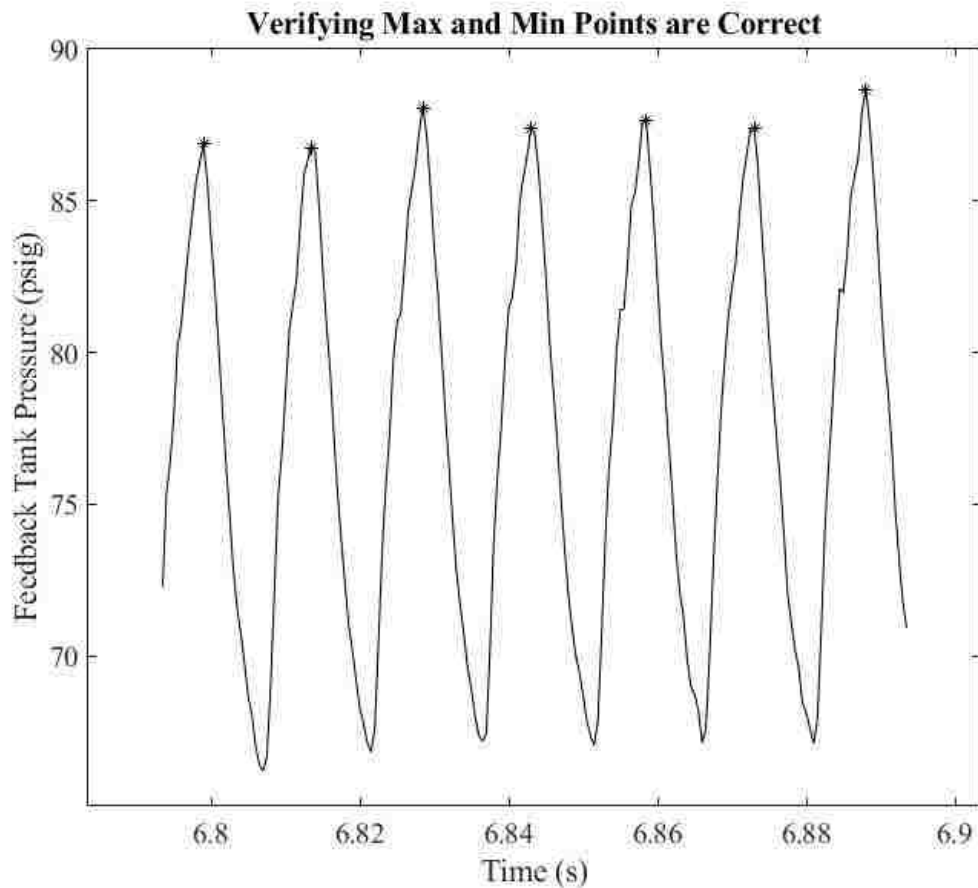
```
ylabel('Feedback Tank Pressure (psig)')

%The user is to determine the starting max point to use
n1=input('Type the starting max point to use');
% Type the starting max point to use1

%The user is to determine whether or not to eliminate any undesired max
%points from right to left
n2=input('The amount of points from right to left you want to omit');
% The amount of points from right to left you want to ommit0

%Determining the final max points to use
Max_n=Max(n1:length(Max)-n2,1);
%Times cooresponding to the max points above
tv_maxn=tv_max(n1:length(tv_max)-n2,1);
```

Verifying Max and Min Points are Correct
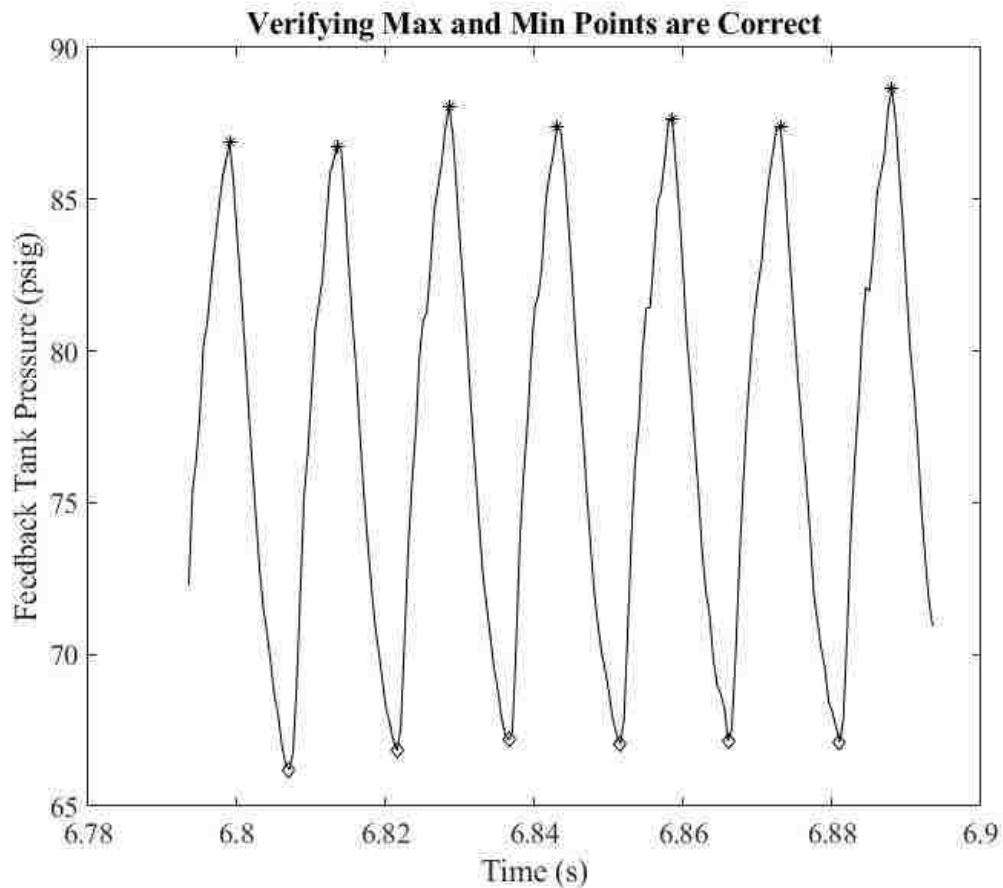
```matlab
%Taking a look at the final max peak points as well as the initial
minimum
%peak points
plot(tv_n,FB_Ln,'-k',tv_maxn,Max_n,'*k',tv_min,Min,'dk')
title('Verifying Max and Min Points are Correct')
xlabel('Time (s)')
ylabel('Feedback Tank Pressure (psig)')

%User determines what starting min peak point to use
n3=input('Type the starting min point to use');
% Type the starting min point to use1

%User determines min peak points to eliminate from right to left
n4=input('The amount of points from right to left you want to omit');
% The amount of points from right to left you want to ommit0

%Final min peak points
Min_n=Min(n3:length(Min)-n4,1);
%Time for minimum peak points
tv_minn=tv_min(n3:length(tv_min)-n4,1);

%Final look at the minimum and maximum points used to determine the
%ampltitude and frequencies
plot(tv_n,FB_Ln,'-k',tv_maxn,Max_n,'*k',tv_minn,Min_n,'dk')
```

```
title('Verifying Max and Min Points are Correct')
xlabel('Time (s)')
ylabel('Feedback Tank Pressure (psig)')
pause
```


Verifying Max and Min Points are Correct
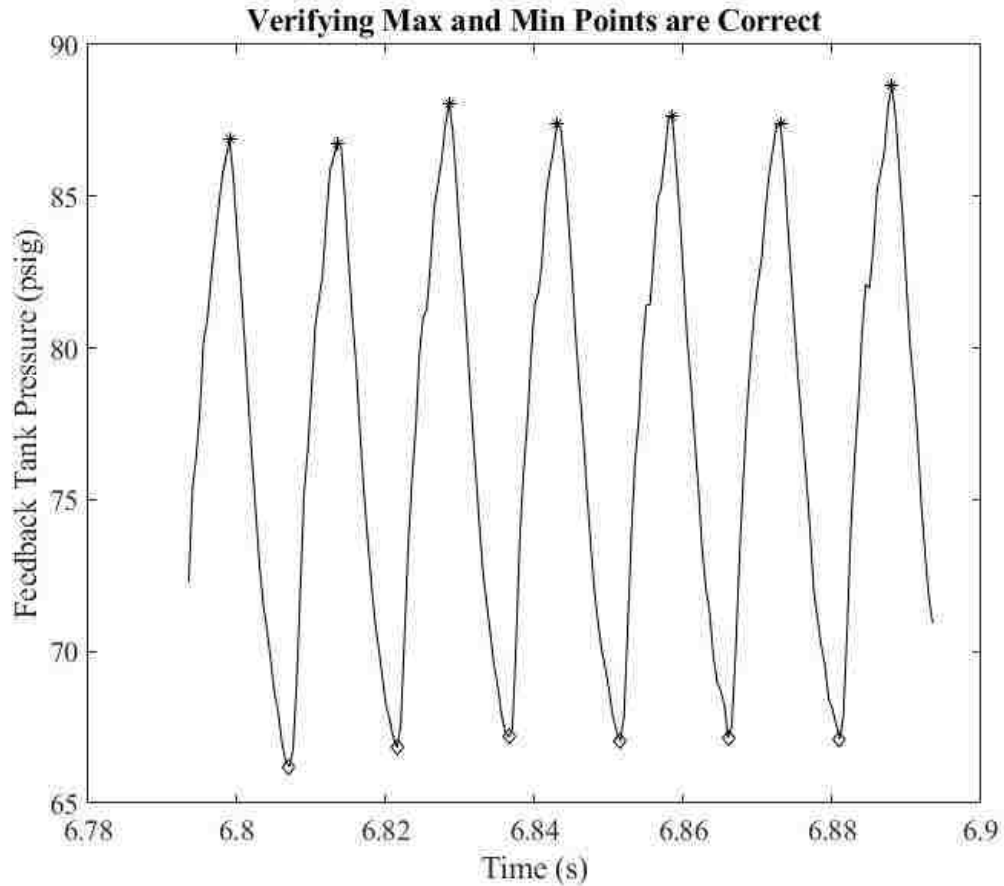
```
%finding the average amplitudes for each cycle
k=1;
for k = 1:(length(Min_n))
    Pfb_amp(k)=(Max_n(k)-Min_n(k)+Max_n(k+1)-Min_n(k))/2;
    Pamp_V(k,:)=Pfb_amp(k);
    k=k+1;
end

%finding the average of all cycles
Pamp_avg=mean(Pamp_V);

% fprintf('The average amplitudes over the selected span is %2.3f psi
\n\n',Pamp_avg)

%finding the degree of freedom
DOF=length(Min_n)-1;

%finding the frequency for each cycle
k=1;
```

```matlab
for k = 1:(length(tv_maxn)-1)
    Freq(k)=(tv_maxn(k+1)-tv_maxn(k))^(-1);
    Freq_V(k,:)=Freq(k);
    k=k+1;
end

%Finding the average frequency of all cycles
Freq_avg=mean(Freq_V);

DOF_f=length(Min_n)-1;
Samp_Dev_F=std(Freq_V);

%Uncertainty for each frequency due to the zero order uncertainty
Wfi=Freq_V.^2/fs;
Wfis=(Wfi./(DOF+1)).^2;
% Overall uncertainty in the frequency readings due to the sampling
% frequency
Wf=sqrt(sum(Wfis));

fprintf('The sample deviation is %2.3f Hz with %2.0f degrees of freedom
\n\n',Samp_Dev_F,DOF_f)

%Random Noise Uncertainty with no pressure in psig
Un=0.632;
```

The figure below shows the results used to obtain the random noise with
no supply pressure in the left feedback tank. This is used in the
analysis for all cases. The results were averaged over the duration
shown below and the uncertainty was obtained using six sigma to obtain
a 99% confidence interval.

Random Noise at 0 psig Supply Pressure; Left Feedback
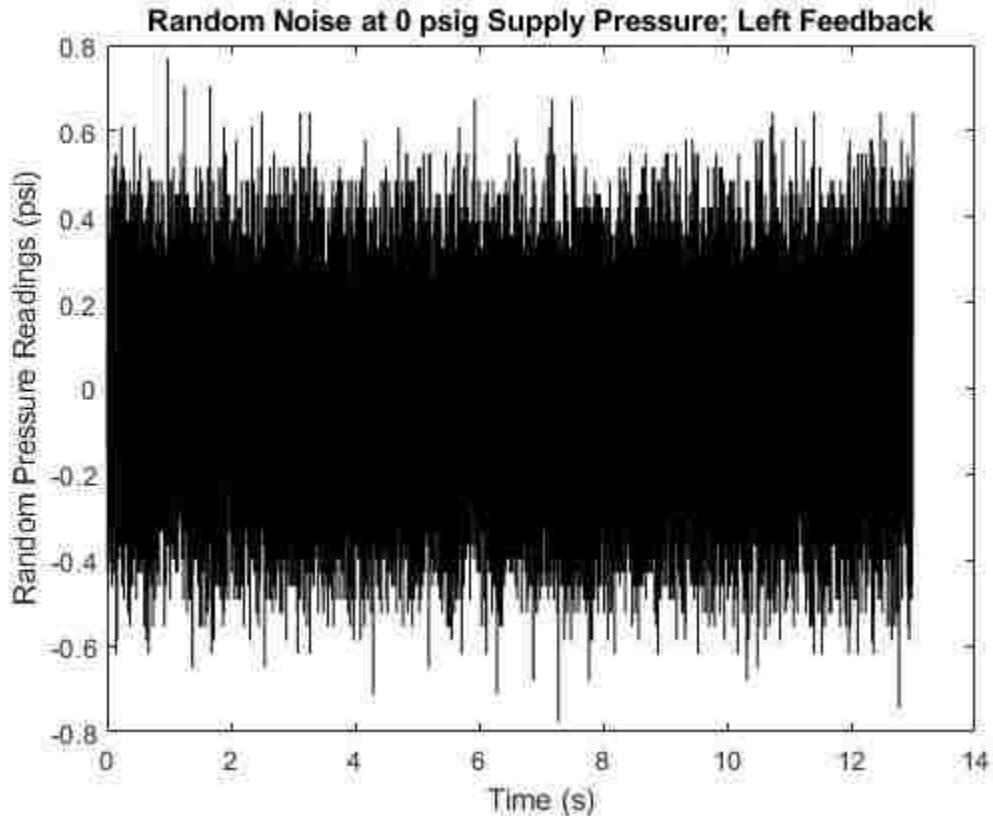
```matlab
%Finding the amplitude uncertainty of each cycle for k number of cycles
k=1;
for k = 1:(length(Max_n)-1)
    U_cycle(k)=sqrt((sqrt((178*10^(-
6)*Max_n(k)+0.097)^2+Un^2+0.98)/2)^2+(sqrt((178*10^(-
6)*Max_n(k+1)+0.097)^2+Un^2+0.98)/2)^2+2*(sqrt((178*10^(-
6)*Min_n(k)+0.097)^2+Un^2+0.98)/2)^2);
    Uc_V(k,:)=U_cycle(k);
    k=k+1;
end

Ucs=(Uc_V./(DOF+1)).^2;%Taking the square of each cycle uncertainty
over
%the number of cycles
Uc=sqrt(sum(Ucs));% Overall design uncertainty for all cycles
Up_t=range(Pamp_V)/sqrt(DOF+1);
Uamp=sqrt(Uc^2+Up_t^2);%overall uncertainty of the feedback tank
pressure
%amplitude

%Displaying the final results
fprintf('Pfb = %2.3f psi\n',Pamp_avg)
fprintf('Ufb = %2.3f psi\n',Uamp)
fprintf('Frequency = %2.1f Hz \n',Freq_avg)
Ut=range(Freq_V)/sqrt(DOF+1);%Uncertainty of frequency due to averaging
Uf=sqrt(Ut^2+Wf^2);
fprintf('Uf = %2.2f Hz\n',Uf)
```

```
Results:
% Pfb = 20.587 psi
% Ufb = 20.529 psi
% Frequency = 67.5 Hz
% Uf = 2.04 Hz
```

The following is a step by step explanation of what the code for determining the

SPF chamber variables are:

1. The user inputs what back pressure in psig to analyze.

2. The code finds the index of that back pressure and this is used to find time and
   feedback pressures.

3. A time vector of 0.1 seconds is created with the time at the index stated above as
   the midpoint.

4. The signal is smoothed with a moving average and plotted versus the raw data as
   well as the line of best fit. The line of best fit is then subtracted from the
   oscillation signal to obtain an oscillation about a mean of zero.

5. Exhaust amplitudes, relative to the line of best fit, are plotted versus time with
   initial max points. The user determines what, if any, max points should be
   eliminated.

6. A new graph of the final max points and initial min points is shown and the user
   determines what min points to eliminate. A new graph is plotted with the final
   max and min points.

7. For loops are used to determine the frequencies and amplitudes as well as their
   uncertainties and displayed as final answers, accordingly, using fprintf.

   The following example is to obtain the frequency and amplitude in the SPF

chamber for the SPF chamber pressure case of 54 psig.

```matlab
A=csvread('C:\SFO - Experiment\Post Processing\Programs\Ps = 300 psig\300psig.txt');

%time at which flow is no longer choked
t_c=11.5;

t=A(1:fs.*t_c,1); %Time vector (s)
Ps=A(1:fs.*t_c,2); % Supply pressure (psi)
FB_R=A(1:fs.*t_c,3); % Right feedback tank pressure (psi)
FB_L=A(1:fs.*t_c,4); % Left feedback tank pressure (psi)
Ch_L=A(1:fs.*t_c,5); % Left chamber pressure from piezoresistive
transducers (psi)
Ch_R=A(1:fs.*t_c,6); % Right chamber pressure from piezoresistive
transducers (psi)
PCB_R=A(1:fs.*t_c,7); % Right chamber pressure from piezoelectric
sensors (psi)
PCB_L=A(1:fs.*t_c,8); % Left chamber pressure from piezoelectric
sensors (psi)

points=50; %Initial number of points in the moving average

Ch_LS=movmean(Ch_L,points);

n=input('Type back pressure in psig')

n=input('Type back pressure in psig')
% Type back pressure in psig58.9

count=0;
%Finding index for back pressure
k=1;
while Ch_LS(k)<(n+1)
    if Ch_LS(k)<n
        k=k+1;
    else
        fprintf('%2.0fn is the index in the column vector where the
back pressure just reaches %2.0f psig\n\n',k,n)
        break
    end
end
t_n=t(k,1);

points_05=fs*0.05;

tv_n=t(k-points_05:k+points_05);%time interval 0.05 seconds before and
after back pressure is reached
PCB_Ln=PCB_L(k-points_05:k+points_05);%Corresponding Chamber Pressure
Amplitude

PCB_LSn=movmean(PCB_Ln,4);%Filters PCB curve with a three point moving
average

%taking a look at raw data vs filtered
plot(tv_n,PCB_Ln,'-k',tv_n,PCB_LSn,'-r')
```

```
title(['Filtered and Raw Chamber Amplitude Pressure for Pb =
',num2str(n),' psig'])
xlabel('Time (s)')
ylabel('Chamber Pressure')
legend('Raw Chamber Pressure','Filtered Chamber Pressure')
pause
```


Filtered and Raw Chamber Amplitude Pressure for Pb = 58.9 psig
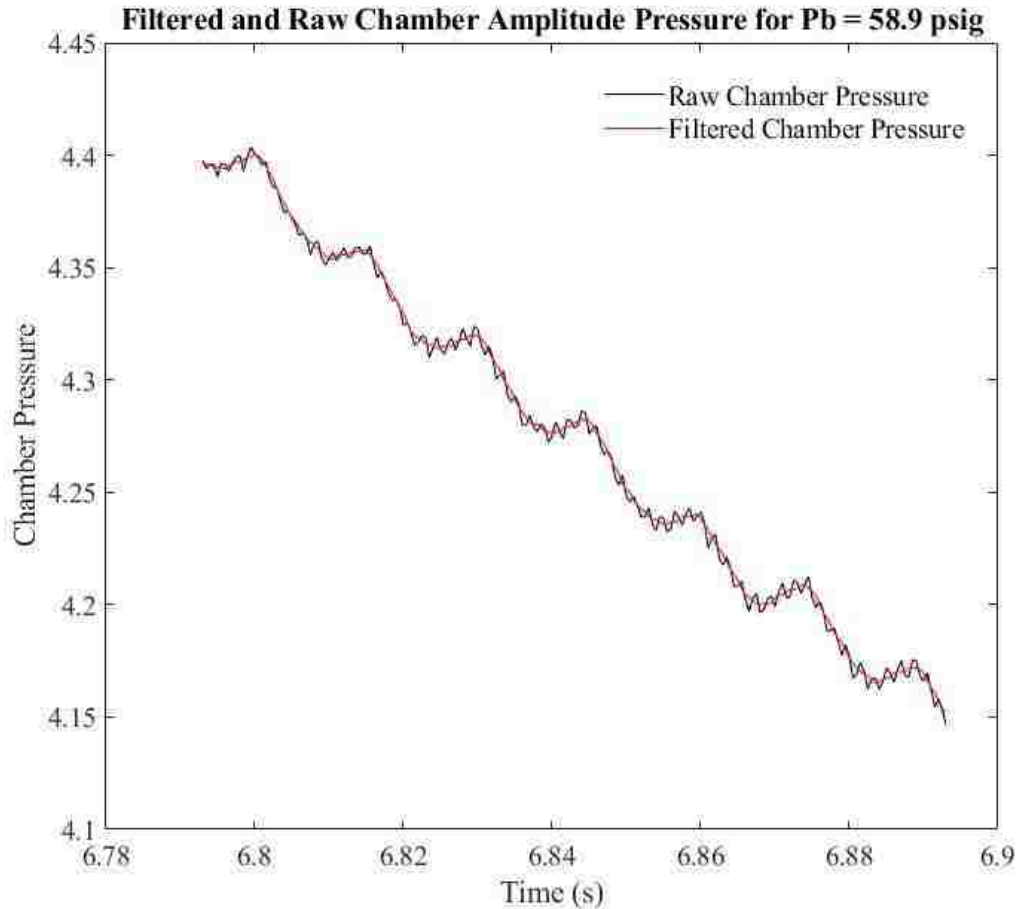
```
%Finding the line of best fit for the chamber pressure amplitudes

Pamp_L=polyfit(tv_n,PCB_LSn,1);% Slope and Intercept for BFSL

PL_n=Pamp_L(1)*tv_n+Pamp_L(2);% Equation of BFSL

%Plotting the filtered PCB curve vs the BFSL
plot(tv_n,PCB_LSn,'-k',tv_n,PL_n,'-r')
title(['Filtered Chamber Pressure vs BFSL for Pb = ',num2str(n),'
psig'])
xlabel('Time (s)')
ylabel('Chamber Pressure(psig)')
legend('Filtered Pamp','BFSL')
pause
```

Filtered Chamber Pressure vs BFSL for Pb = 58.9 psig
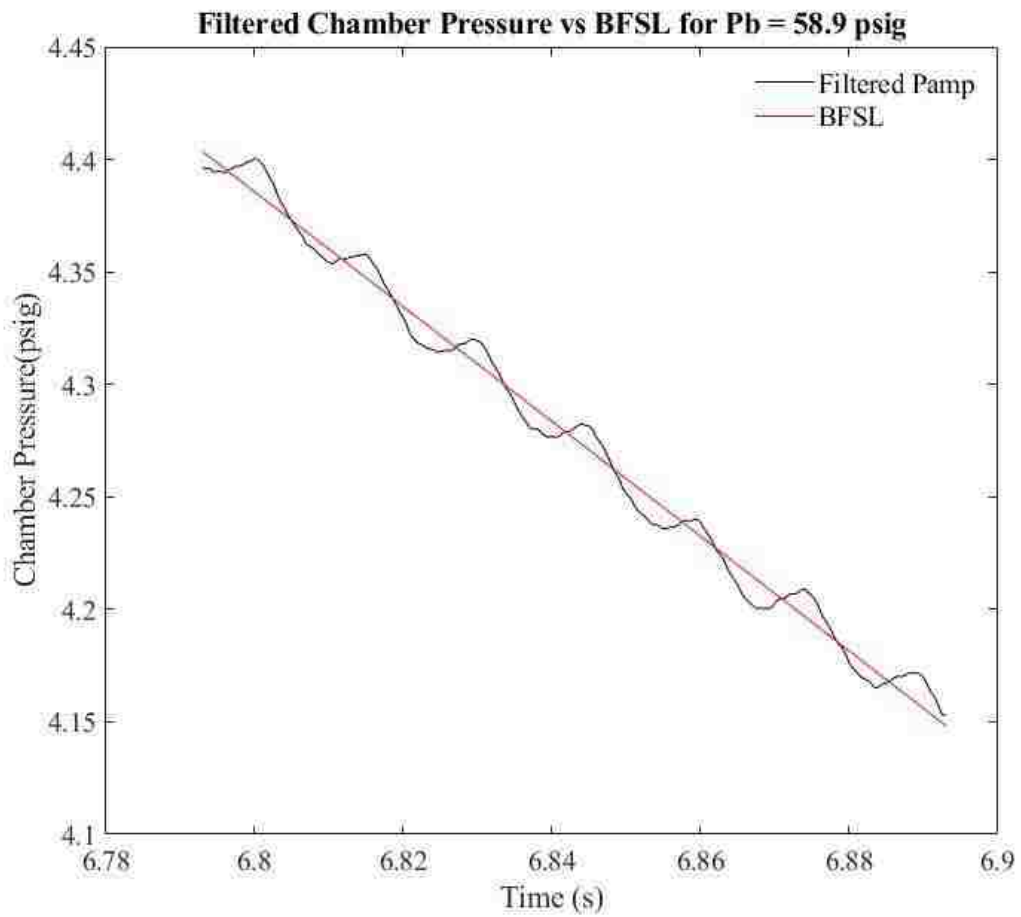
```
%Finding the chamber pressure readings relative to the BFSL

Pamp_n=PCB_LSn-PL_n;

plot(tv_n,Pamp_n,'-k')
title(['Left Chamber Pressure Amplitudes for Pb = ',num2str(n),'
psig'])
xlabel('Time (s)')
ylabel('Pressure Amplitudes (psi)')
pause
```

Left Chamber Pressure Amplitudes for Pb = 58.9 psig
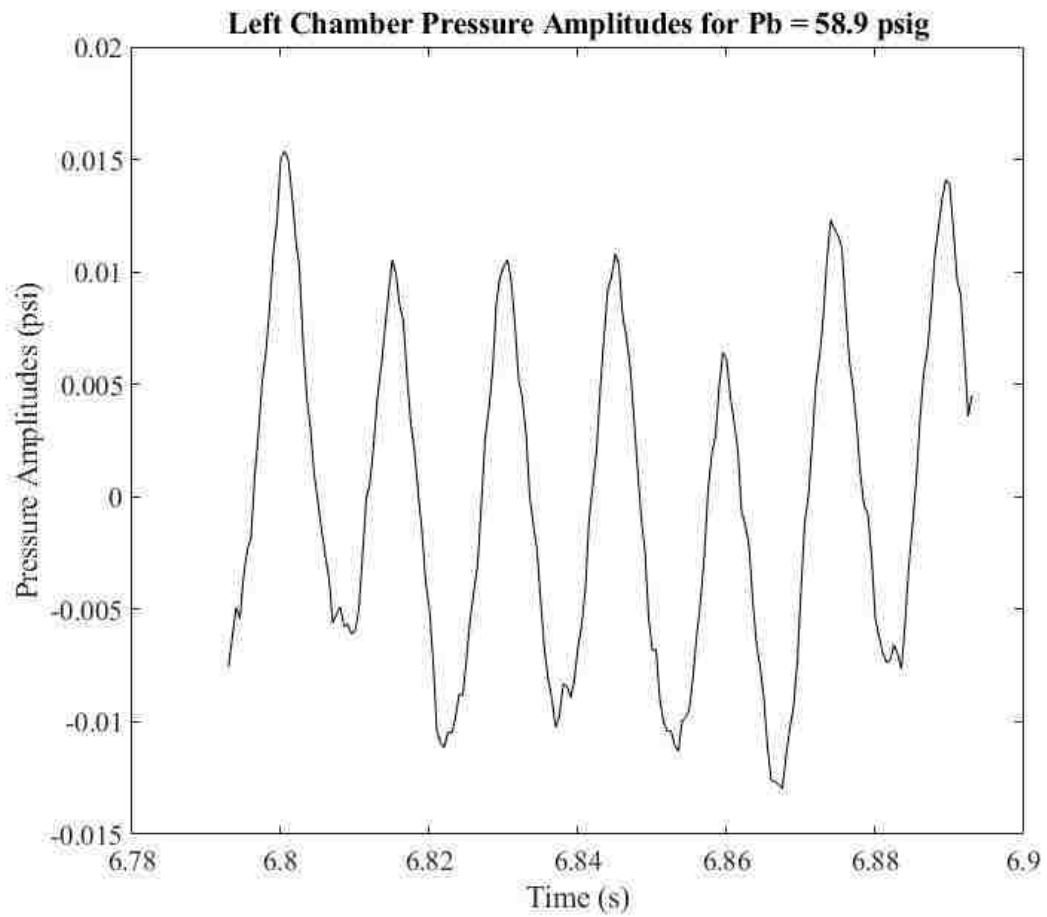

```
[MaxVal,MaxLoc]=findpeaks(Pamp_n(:,1),'MinPeakDistance',20);

t_max=tv_n(MaxLoc,1);

plot(tv_n,Pamp_n,'-k',t_max,MaxVal,'*k')
```
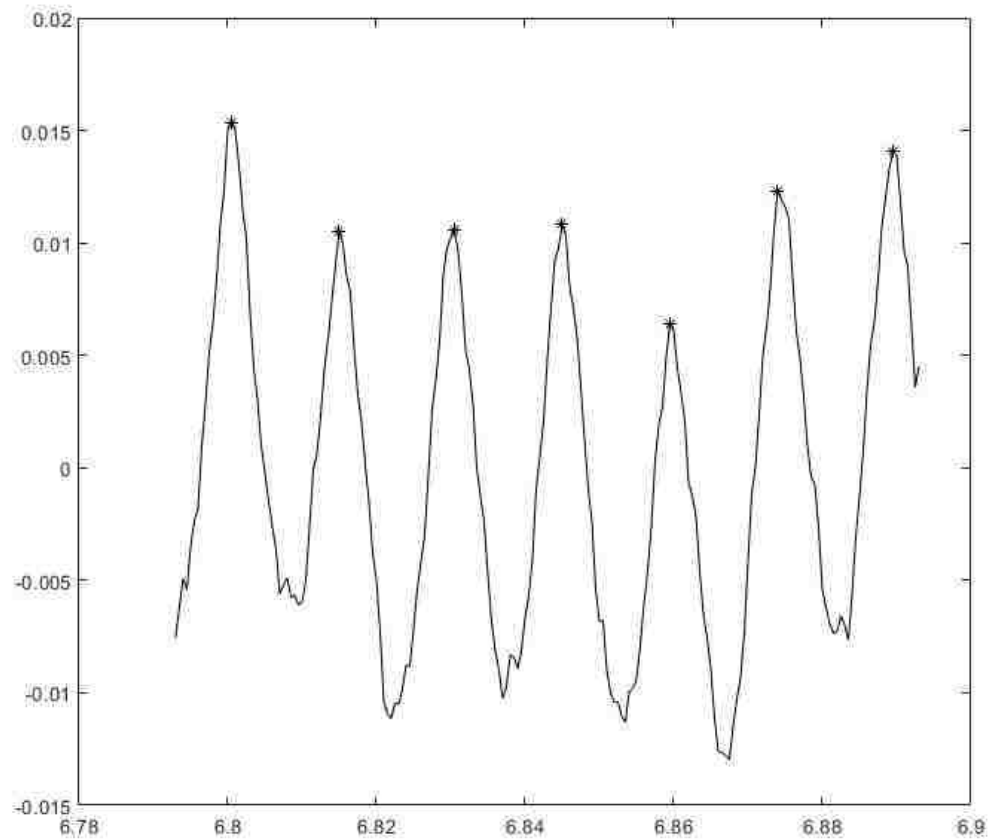
```matlab
n1=input('First max peak point to use');
% First max peak point to use2

n2=input('Number of discarded points from right to left');
% Number of discarded points from right to left0


Max_n=MaxVal(n1:length(MaxVal)-n2);
t_maxn=t_max(n1:length(t_max)-n2);

n3=input('First min peak point to use');
% First min peak point to use2
n4=input('Number of discarded points from right to left');
% Number of discarded points from right to left0

Min_n=MinVal(n3:length(MinVal)-n4,1);
t_minn=t_min(n3:length(t_min)-n4,1);

plot(tv_n,Pamp_n,'-k',t_maxn,Max_n,'*k',t_minn,Min_n,'dk')
```
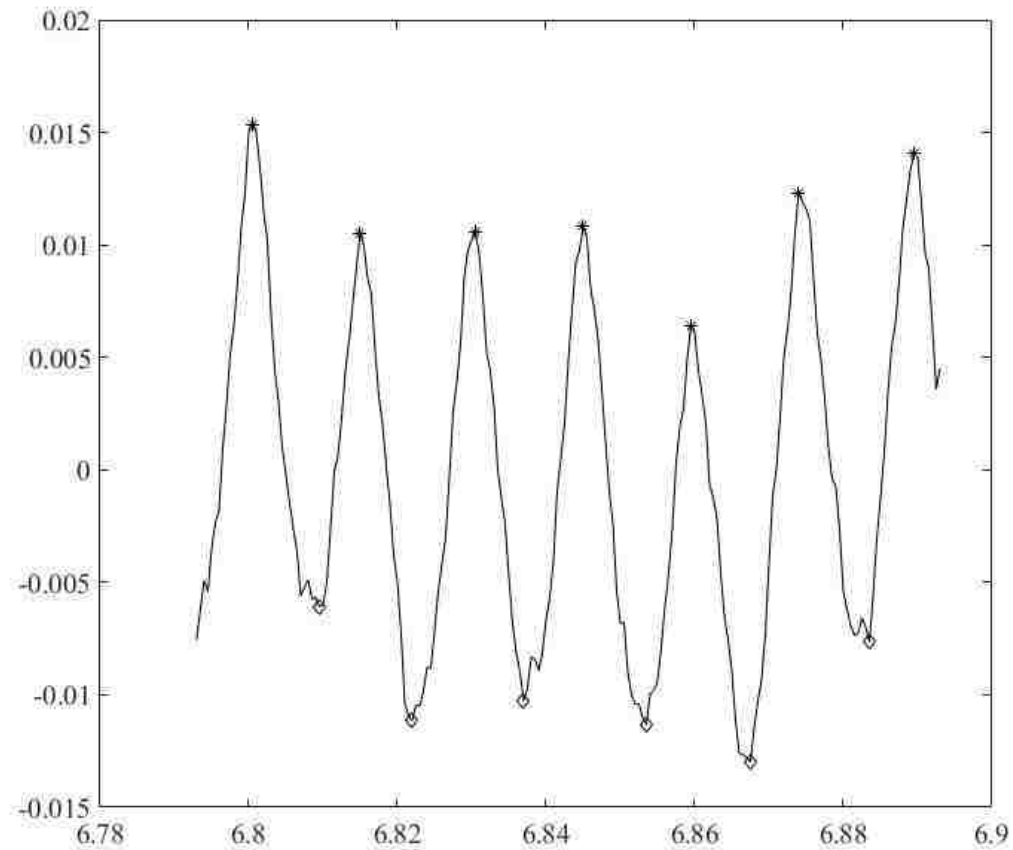
```matlab
%finding average amplitude for each cycle
k=1;
for k = 1:(length(Min_n)-1)
    Pamp(k)=(Max_n(k)-Min_n(k)+Max_n(k+1)-Min_n(k))/2;
    Pamp_V(k,:)=Pamp(k);
    k=k+1;
end

%finding average ampltitude over all cycles
Pamp_avg=mean(Pamp_V);

%finding average frequency over all cycles
Freq_avg=mean(Freq_V);
%finding the degree of freedom
DOF_f=length(Min_n)-1;

%Uncertainty for each frequency due to the zero order uncertainty
Wfi=Freq_V.^2/fs;
Wfis=(Wfi./(DOF+1)).^2;
% Overall uncertainty in the frequency readings due to the sampling
% frequency
Wf=sqrt(sum(Wfis));
```

```matlab
Ud=0.0071; %Design uncertainty (Constant for all cases)


%Finding the uncertainty of each cycle for k number of cycles
k=1;
for k = 1:(length(Max_n)-1)

U_cycle(k)=sqrt((sqrt(Ud^2+(0.01*Max_n(k))^2)/2)^2+(sqrt(Ud^2+(0.01*Max
_n(k+1))^2)/2)^2+2*(sqrt(Ud^2+(0.01*Min_n(k))^2)/2)^2);
    Uc_V(k,:)=U_cycle(k);
    k=k+1;
end

Ucs=(Uc_V./(DOF+1)).^2;%Taking the square of each cycle uncertainty
over the number of cycles
Uc=sqrt(sum(Ucs));% Overall design uncertainty for all cycles

Up_t=range(Pamp_V)/sqrt(DOF+1); %95% confidence for the average
amplitudes using range instead of standard deviation due to the lack of
sample size

Uamp=sqrt(Uc^2+Up_t^2); %overall uncertainty in the pressure amplitude
Ut=range(Freq_V)/sqrt(DOF+1);%Uncertainty of frequency due to averaging
Uf=sqrt(Ut^2+Wf^2);
%displaying all results
fprintf('Pamp = %2.3f psi\n',Pamp_avg)
fprintf('Uamp = %2.3f psi\n',Uamp)
fprintf('Frequency = %2.1f Hz\n',Freq_avg)
fprintf('Uf = %2.2f Hz\n',Uf)

Results:
% Pamp = 0.021 psi
% Uamp = 0.003 psi
% Frequency = 67.5 Hz
% Uf = 2.04 Hz
```

C.2: Comparison of the Right and Left SPF Chambers and Feedback Tank Results

To verify the pressure amplitudes measured in the left SPF chambers and the feedback tanks, a comparison between the left and right side of the SFO is shown in Figure C.1 for a supply pressure of 2.772 MPa gauge (402 psig).
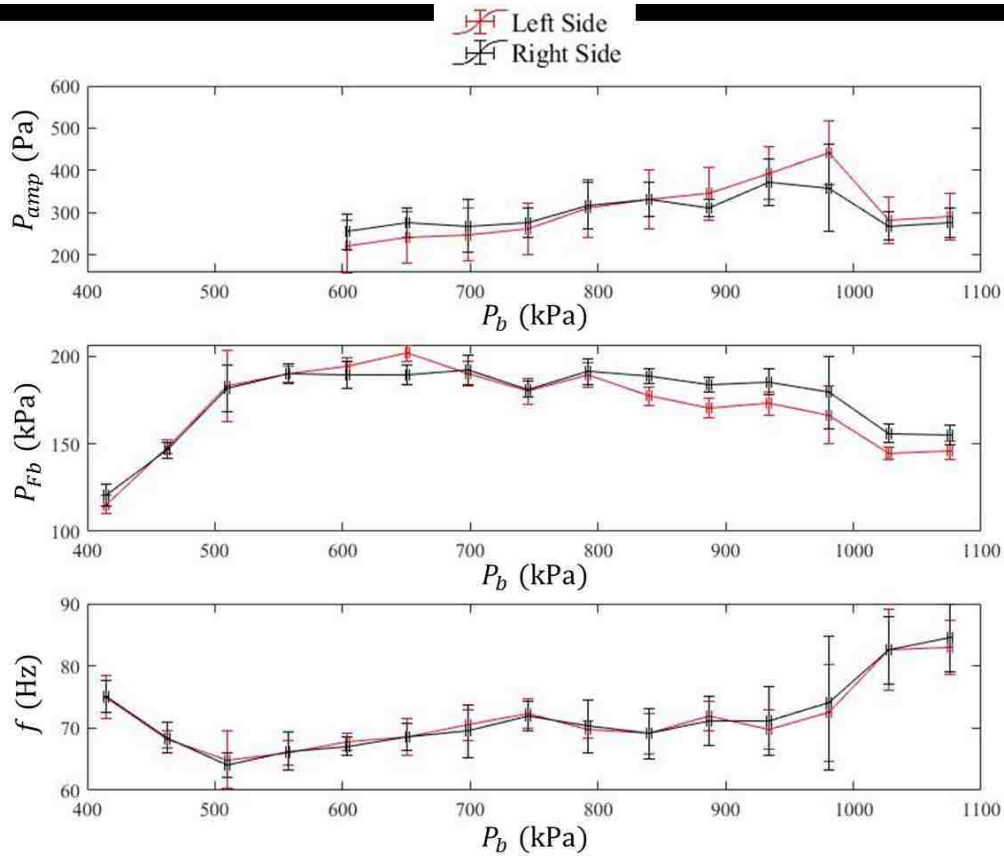
Figure C.1 Comparing results of the left and right side of the SFO; Ps = 2.772 MPa (402 psig)

All points of measurements correspond to pressure in the left SPF chamber. All of the frequencies and SPF chamber amplitudes are within the uncertainties for all points. There are several points that are not within the uncertainties for the feedback tank pressures. When the left feedback tanks have larger amplitudes than the right, the left SPF chamber amplitudes are smaller than the right SPF chambers and vice versa. Figure C.2 shows the amplitudes and average pressure readings in the feedback tanks and the SPF chambers. There is a secondary low frequency oscillation in the mean pressure readings. This is because of the volumes of the SPF chambers. If these volumes are decreased, the secondary frequency is expected to be larger. The result of this secondary frequency is the reasoning behind the feedback tank amplitudes being within the

uncertainties for all back pressure points. This secondary frequency is a result of either the momentum switching mechanism discussed in Chapter 1.2.1 or the recirculation switching mechanism discussed in Chapter 1.2.2. The latter is likely the case since there is no direct pathway for the return flow to impinge on the main jet flow at a high momentum.
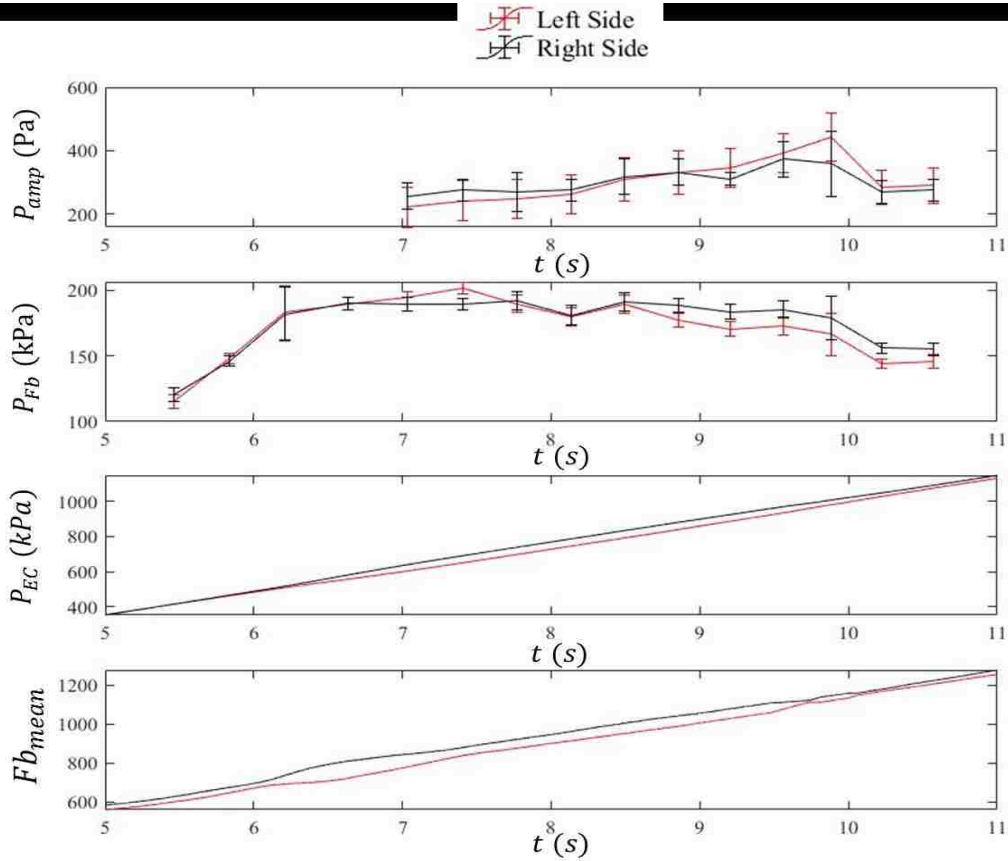
Figure C.2: Comparing amplitudes vs mean pressures

C.3: Calcuation of Percentage Leak

An example MATLAB program for obtaining the % Leak for a supply pressure of 0.731 MPa gauge (106 psig) is shown below:

```
clear
clc
format short
```

```
%Results for the leak test using Nitrogen at a starting pressure of
175psig

%Text file for N2 at a starting pressure of 106 psig
A=csvread('C:\SFO - Experiment\Post Processing\Programs\Leak Test\100
psig\100psig-LT.txt');
t_1=A(:,1); %Time of the experiment
P_1=A(:,5); %Chamber pressure in psig
P_knot=max(P_1);


P_Pa=(P_1+14.7).*6894.76; %Converting pressure from psig to Pa absolute

plot(t_1,P_Pa,'-k')
title('Chamber Pressure vs Time')
xlabel('Time (s)')
ylabel('Chamber Pressure Pa abs')
pause
```
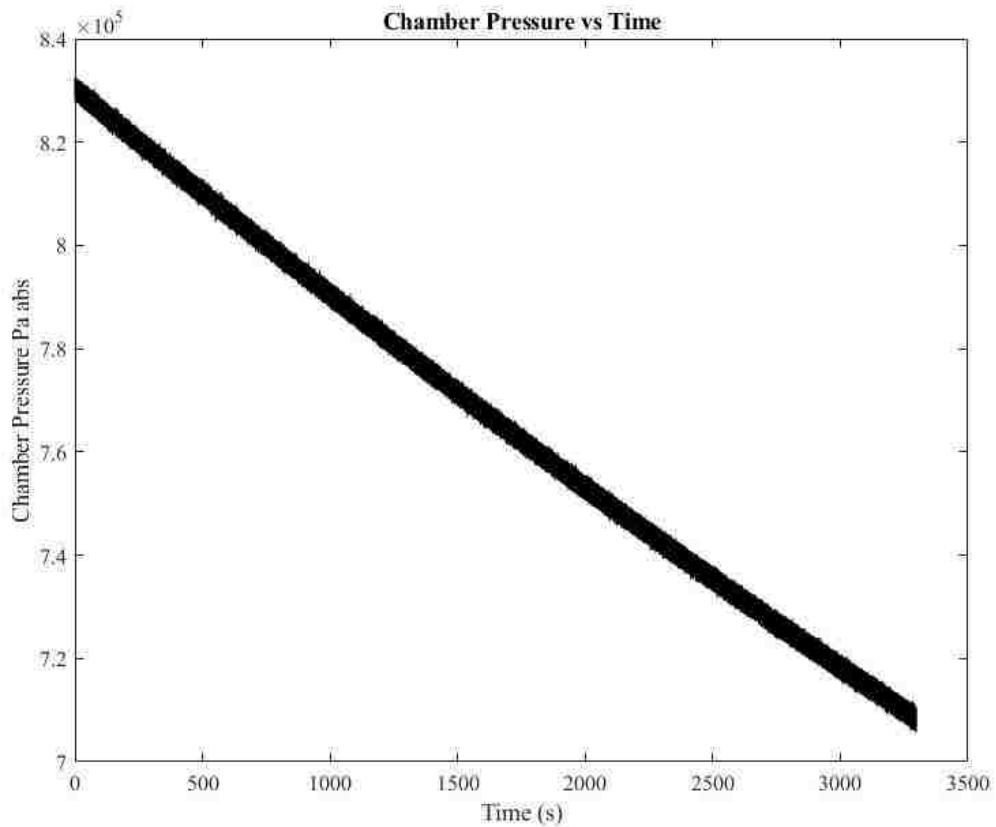

Using the data above, built-in MATLAB curve fit tool
"cftool" was used to obtain the parameters of Equation C.1

General model Exp1:
    f(x) = a*exp(b*x)
Coefficients (with 95% confidence bounds):
    a = 8.296e+05 (8.296e+05, 8.296e+05)
    b = -4.822e-05 (-4.823e-05, -4.822e-05)

Goodness of fit:
  SSE: 4.566e+12
  R-square: 0.9994
  Adjusted R-square: 0.9994
  RMSE: 832
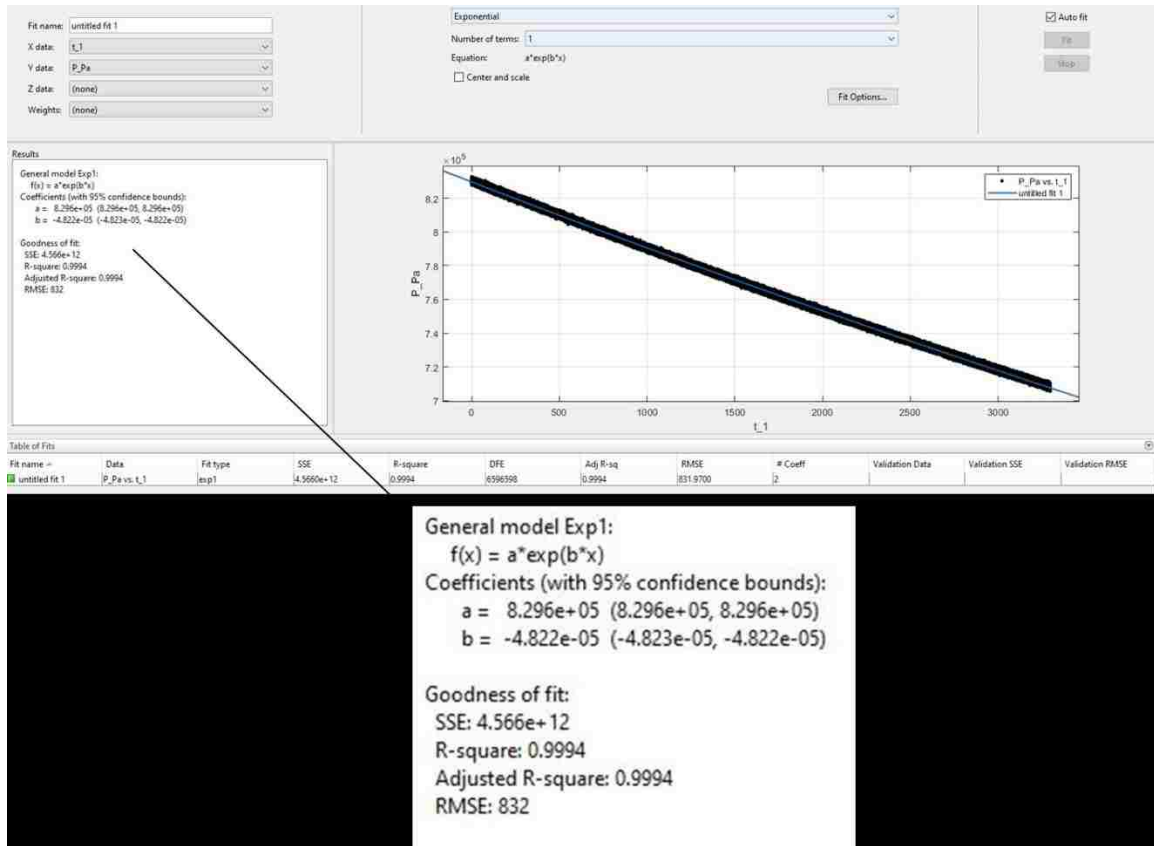
```matlab
%leaking at larger pressures - R-squared for the fit is 0.9994 -
constant
%"a" refers to the initial pressure in Pa (abs)
a=8.296*10^(5); %initial pressure obtained via curve fitting
b=-4.822*10^(-5); %Leak constant (beta)

%Curve fit pressure with a plot versus time to follow
P=a*exp(b.*t_1);
plot(t_1,P_Pa,'-k',t_1,P,'-r')
    title('Chamber Pressure vs Time')
    xlabel('Time(s)')
    ylabel('Absolute Pressure(Pa)')
    legend('Raw Pressure','Curve Fit Pressure')
pause
```

Chamber Pressure vs Time
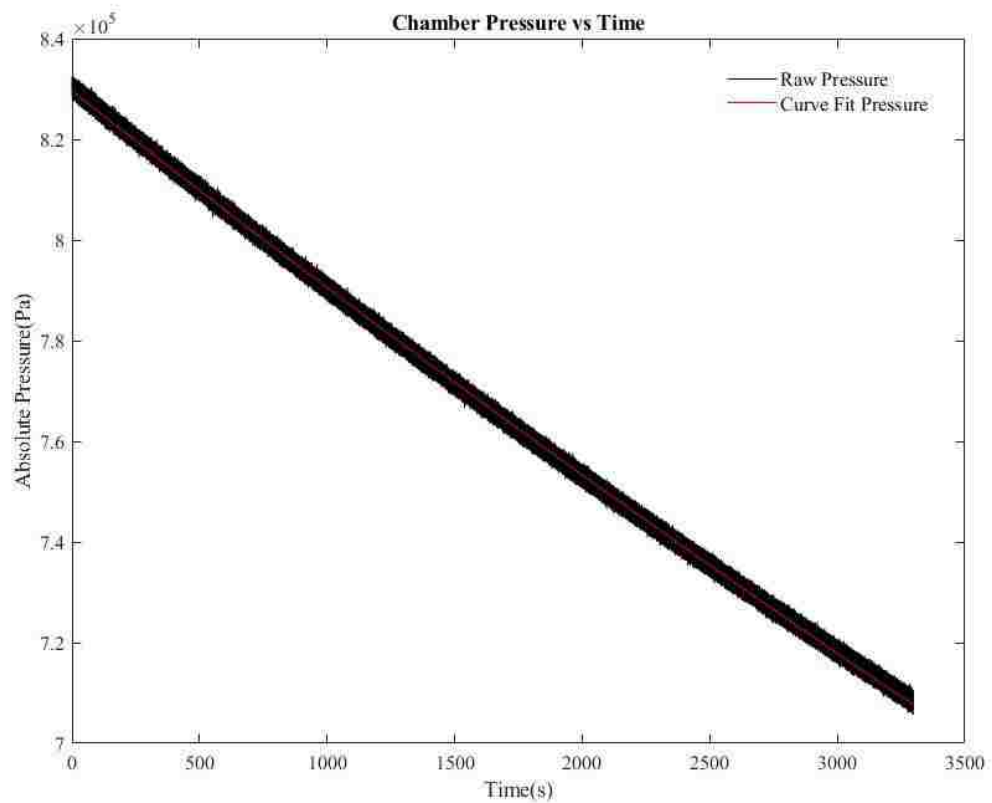
```
% %To determine an approximation of the mass flow rate leaking as a
function
% %of pressure with the use of the gas law in the form
dm/dt=V(dP(t)/dt)/RT
R=297; %Gas constant for Nitrogen in (J/kgK)
T=295; %Temperature in K
V=0.0167; %Volume of the oscillator in cubic meters
m_dot=V*b.*P/(R*T);

%Plot of mass flow rate leaking vs absolute pressure
plot(P,m_dot,'-k')
    title('Predicted Mass Flow Rate Leakage vs Pressure')
    xlabel('Absolute Pressure (Pa)')
    ylabel('Mass Flow Rate Leaking (kg/s)')
pause
```

Predicted Mass Flow Rate Leakage vs Pressure
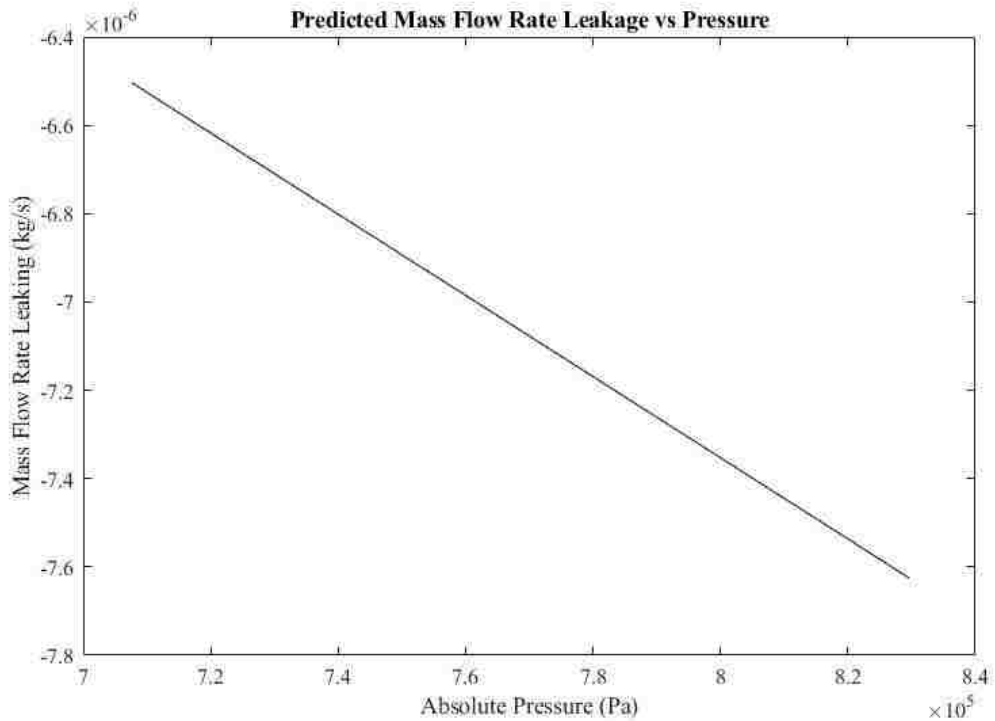
```
%Calculating the percent leakage for the initial pressure supply
%pressure case
P_in=a; %Supply Pressure
At=3.2*10^(-6); %Throat area in meters squared
m_dot_in=0.685*P_in*At/sqrt(T*R); %Supplied mass flow rate in kg/s
fprintf('The mass flow rate entering the system for a supply pressure
of %2.1f psig is %2.5f kg/s\n\n',P_knot,m_dot_in)
m_dot_leak=abs(min(m_dot)); %Mass flow rate leaking for 0.832 MPa abs
in kg/s
fprintf('The mass flow rate leaking when the pressure in the SFO is
%2.1f psig is %2.8f kg/s\n\n',P_knot,m_dot_leak)
Percent_leak=m_dot_leak/m_dot_in*100;%Calculating the % leak of mass
flow rate to the mass flow rate entering
fprintf('The percent leak for %1.1f psig is %3.3f
%s\n\n',P_knot,Percent_leak,'%')

% the mass flow rate entering the system for a supply pressure of 106.1
psig is 0.00614 kg/s

% the mass flow rate leaking when the pressure in the SFO is 106.1 psig
is 0.00000762 kg/s

% the percent leak for 106.1 psig is 0.124%
```

112
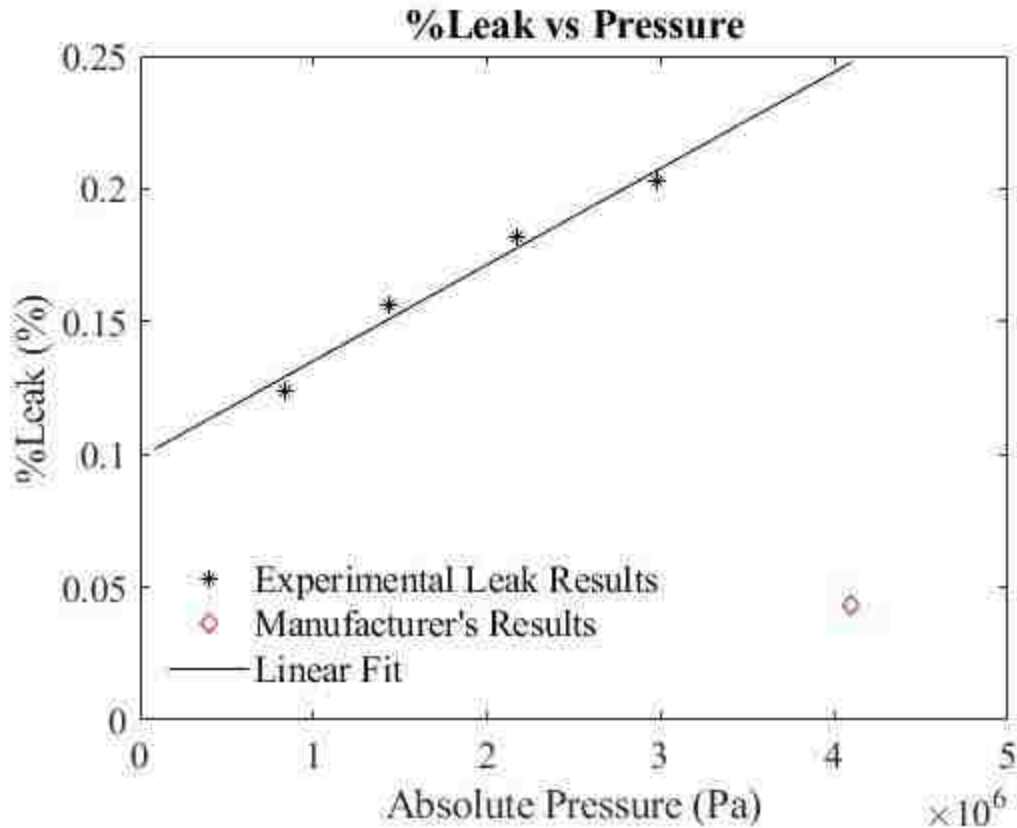
%Leak vs Pressure

Figure C.3: %Leak versus absolute supply pressure

C.4: Repeatability Test Results; Ps ≈ 3.971 MPa (576 psig)

The non-dimensional results for the repeatability test are shown in Chapter 5.3. The dimensioned results are shown in the tables below. All of the frequency results shown non-dimensionally are measured from the feedback tank readings. The frequencies are also obtained in the SPF chambers and compared with the feedback tank frequencies in the tables below. Additionally, a percent difference of the frequencies is calculated for a direct comparison between feedback tanks and SPF chambers using Equation C.6. This is also shown in the tables provided in Appendix C.5 for the various supply pressure cases.

$$\%_{DIFF} = \left| \frac{f_{Fb} - f_{EC}}{f_{Fb}} \right| x100\% \qquad (C.6)$$

Table C.1: Pressure Amplitude Results for Repeatability Trial 1; Ps = 3.958 MPa

P_b (MPa)	P_{Fb} (kPa)	U_{Fb} (kPa)	U_{Fb} (%)	P_{amp} (Pa)	U_{amp} (Pa)	U_{amp} (%)
0.629	174.6	6.4	4%	N/A	N/A	N/A
0.696	216.3	5.8	3%	N/A	N/A	N/A
0.763	286.8	18.5	6%	N/A	N/A	N/A
0.829	270.8	4.6	2%	324	34	11%
0.896	282.0	7.0	2%	303	28	9%
0.963	297.5	7.4	2%	331	41	13%
1.029	297.7	7.7	3%	345	28	8%
1.096	258.0	6.7	3%	324	28	9%
1.162	264.7	7.6	3%	372	34	9%
1.229	252.3	6.1	2%	427	41	10%
1.296	235.4	4.7	2%	434	28	6%
1.363	229.4	19.5	9%	441	48	11%
1.429	223.1	11.0	5%	400	41	10%
1.496	211.6	8.6	4%	379	21	5%
1.563	206.1	6.2	3%	359	21	6%

Table C.2: Frequency Results for Repeatability Trial 1; Ps = 3.958 MPa

P_b (MPa)	f_{Fb} (Hz)	$U_{f_{Fb}}$ (Hz)	$U_{f_{Fb}}$ (%)	f_{EC} (Hz)	$U_{f_{EC}}$ (Hz)	$U_{f_{EC}}$ (%)	$\%_{Diff}$ (%)
0.629	73.8	3.18	4%	N/A	N/A	N/A	N/A
0.696	67.8	1.33	2%	N/A	N/A	N/A	N/A
0.763	61.8	2.69	4%	N/A	N/A	N/A	N/A
0.829	64.5	0.93	1%	64.3	3.52	5%	0.31%
0.896	67.5	2.97	4%	66.4	2.79	4%	1.63%
0.963	65.1	4.93	8%	65.4	3.05	5%	0.46%
1.029	67.6	4.82	7%	68.6	2.17	3%	1.48%
1.096	72.8	2.49	3%	73.7	3.43	5%	1.24%
1.162	71.0	2.33	3%	70.6	1.43	2%	0.56%
1.229	71.0	2.55	4%	70.2	1.42	2%	1.13%
1.296	72.3	1.52	2%	71.9	2.34	3%	0.55%
1.363	74.3	4.99	7%	73.9	4.30	6%	0.54%
1.429	80.1	3.71	5%	79.2	2.53	3%	1.12%
1.496	81.0	2.72	3%	82.1	5.04	6%	1.36%
1.563	85.0	4.35	5%	84.2	6.09	7%	0.94%

Table C.3: Pressure Amplitude Results for Repeatability Trial 2; Ps = 3.971 MPa

P_b (MPa)	P_{Fb} (kPa)	U_{Fb} (kPa)	U_{Fb} (%)	P_{amp} (Pa)	U_{amp} (Pa)	U_{amp} (%)
0.632	171.1	5.5	3%	N/A	N/A	N/A
0.698	208.5	7.1	3%	N/A	N/A	N/A
0.765	258.3	14.2	5%	N/A	N/A	N/A
0.832	273.8	5.4	2%	290	34	12%
0.899	280.9	5.4	2%	290	34	12%
0.966	292.6	5.3	2%	331	28	8%
1.034	270.9	9.5	4%	303	34	11%
1.100	264.3	10.7	4%	338	21	6%
1.167	268.3	8.9	3%	379	28	7%
1.234	268.7	10.9	4%	490	34	7%
1.301	238.6	4.6	2%	448	28	6%
1.368	237.1	5.3	2%	496	41	8%
1.435	213.4	5.9	3%	386	28	7%
1.502	211.7	6.0	3%	414	28	7%
1.569	218.7	6.5	3%	393	21	5%

Table C.4: Frequency Results for Repeatability Trial 2; Ps = 3.971 MPa

P_b (MPa)	f_{Fb} (Hz)	$U_{f_{Fb}}$ (Hz)	$U_{f_{Fb}}$ (%)	f_{EC} (Hz)	$U_{f_{EC}}$ (Hz)	$U_{f_{EC}}$ (%)	$\%_{Diff}$ (%)
0.632	75.3	6.39	8%	N/A	N/A	N/A	N/A
0.698	68.6	1.34	2%	N/A	N/A	N/A	N/A
0.765	64.7	4.63	7%	N/A	N/A	N/A	N/A
0.832	64.2	3.63	6%	64.6	2.77	4%	0.62%
0.899	67.6	2.36	3%	67.2	2.23	3%	0.59%
0.966	65.1	4.50	7%	66.0	2.02	3%	1.38%
1.034	70.3	4.31	6%	70.4	5.17	7%	0.14%
1.100	71.4	1.04	1%	72.8	3.43	5%	1.96%
1.167	69.8	2.18	3%	70.3	4.31	6%	0.72%
1.234	68.7	2.98	4%	68.6	3.27	5%	0.15%
1.301	71.5	2.33	3%	71.6	4.00	6%	0.14%
1.368	70.3	3.19	5%	71.0	5.98	8%	1.00%
1.435	79.5	2.92	4%	79.1	1.66	2%	0.50%
1.502	79.7	3.70	5%	80.1	2.71	3%	0.50%
1.569	81.0	2.72	3%	81.5	2.73	3%	0.62%

Table C.5: Pressure Amplitude Results for Repeatability Trial 3; Ps = 3.978 MPa

P_b (MPa)	P_{Fb} (kPa)	U_{Fb} (kPa)	U_{Fb} (%)	P_{amp} (Pa)	U_{amp} (Pa)	U_{amp} (%)
0.633	169.6	5.7	3%	N/A	N/A	N/A
0.700	216.1	6.7	3%	N/A	N/A	N/A
0.767	272.6	26.4	10%	N/A	N/A	N/A
0.834	273.0	5.5	2%	290	21	7%
0.901	280.0	5.7	2%	283	28	10%
0.968	294.3	5.2	2%	331	28	8%
1.035	274.1	10.2	4%	317	28	9%
1.102	254.7	5.9	2%	310	28	9%
1.169	256.5	13.1	5%	372	48	13%
1.236	264.5	7.8	3%	462	28	6%
1.303	248.0	5.3	2%	462	41	9%
1.370	239.8	11.0	5%	510	21	4%
1.438	213.3	4.3	2%	386	28	7%
1.504	219.0	5.2	2%	407	28	7%
1.571	206.6	5.7	3%	379	21	5%

Table C.6: Frequency Results for Repeatability Trial 3; Ps = 3.978 MPa

P_b (MPa)	f_{Fb} (Hz)	$U_{f_{Fb}}$ (Hz)	$U_{f_{Fb}}$ (%)	f_{EC} (Hz)	$U_{f_{EC}}$ (Hz)	$U_{f_{EC}}$ (%)	$\%_{Diff}$ (%)
0.633	75.6	3.69	5%	N/A	N/A	N/A	N/A
0.700	67.4	1.32	2%	N/A	N/A	N/A	N/A
0.767	63.7	5.71	9%	N/A	N/A	N/A	N/A
0.834	65.9	1.25	2%	65.3	2.78	4%	0.91%
0.901	67.6	2.36	3%	68.6	3.27	5%	1.48%
0.968	65.4	3.52	5%	64.9	1.91	3%	0.76%
1.035	69.2	4.83	7%	69.8	3.18	5%	0.87%
1.102	74.1	2.51	3%	74.2	3.68	5%	0.13%
1.169	72.0	4.32	6%	72.0	4.63	6%	0.00%
1.236	68.4	4.52	7%	67.6	3.76	6%	1.17%
1.303	69.4	2.18	3%	69.5	2.99	4%	0.14%
1.370	71.7	5.55	8%	71.9	3.42	5%	0.28%
1.438	80.0	2.93	4%	80.2	5.42	7%	0.25%
1.504	78.9	4.65	6%	78.8	3.69	5%	0.13%
1.571	83.9	4.33	5%	83.4	2.75	3%	0.60%

Table C.7: Pressure Amplitude Results for Repeatability Trial 4; Ps = 3.971 MPa

P_b (MPa)	P_{Fb} (kPa)	U_{Fb} (kPa)	U_{Fb} (%)	P_{amp} (Pa)	U_{amp} (Pa)	U_{amp} (%)
0.632	168.9	7.3	4%	N/A	N/A	N/A
0.698	213.8	7.1	3%	N/A	N/A	N/A
0.765	276.3	26.1	9%	N/A	N/A	N/A
0.832	270.7	6.4	2%	324	41	13%
0.899	278.8	4.2	2%	303	28	9%
0.966	286.9	4.6	2%	303	28	9%
1.034	273.9	9.8	4%	317	28	9%
1.100	258.2	8.5	3%	338	28	8%
1.167	273.6	7.8	3%	393	28	7%
1.234	261.1	9.7	4%	448	28	6%
1.301	242.1	6.2	3%	462	28	6%
1.368	221.5	18.3	8%	441	48	11%
1.435	221.5	14.4	6%	414	62	15%
1.502	212.5	5.8	3%	393	34	9%
1.569	210.9	5.6	3%	379	28	7%

Table C.8: Frequency Results for Repeatability Trial 4; Ps = 3.971 MPa

P_b (MPa)	f_{Fb} (Hz)	$U_{f_{Fb}}$ (Hz)	$U_{f_{Fb}}$ (%)	f_{EC} (Hz)	$U_{f_{EC}}$ (Hz)	$U_{f_{EC}}$ (%)	$\%_{Diff}$ (%)
0.632	75.4	3.42	5%	N/A	N/A	N/A	N/A
0.698	68.6	2.17	3%	N/A	N/A	N/A	N/A
0.765	63.8	7.16	11%	N/A	N/A	N/A	N/A
0.832	64.1	2.08	3%	64.1	2.08	3%	0.00%
0.899	65.9	1.25	2%	66.8	3.76	6%	1.37%
0.966	66.0	4.94	7%	66.4	4.11	6%	0.61%
1.034	70.3	3.19	5%	69.8	2.18	3%	0.71%
1.100	72.4	2.35	3%	71.8	2.16	3%	0.83%
1.167	69.1	3.18	5%	69.0	2.99	4%	0.14%
1.234	69.7	5.97	9%	68.8	4.82	7%	1.29%
1.301	71.1	3.20	5%	71.1	2.15	3%	0.00%
1.368	74.3	4.65	6%	75.2	4.65	6%	1.21%
1.435	79.3	3.70	5%	78.4	3.69	5%	1.13%
1.502	80.8	6.00	7%	82.1	2.73	3%	1.61%
1.569	82.9	2.93	4%	83.5	4.02	5%	0.72%

C.5: Dimensioned Results at Various Supply Pressures

This section covers the dimensioned results for all supply pressure cases that are not included in Appendix C.4. Furthermore, a comparison of the frequencies measured in the feedback tanks and the SPF chambers are shown. The frequencies measured in the feedback tanks are used in the Chapter 5.

Table C.9: Pressure Amplitude Results for Ps = 2.110 MPa

P_b (MPa)	P_{Fb} (kPa)	U_{Fb} (kPa)	U_{Fb} (%)	P_{amp} (Pa)	U_{amp} (Pa)	U_{amp} (%)
0.297	81.6	4.2	5%	76	21	28%
0.333	110.8	4.2	4%	110	21	19%
0.372	135.3	17.8	13%	159	48	30%
0.406	141.9	3.6	3%	145	21	14%
0.442	142.1	5.0	4%	152	21	14%
0.479	148.7	3.8	3%	152	21	14%
0.515	145.9	4.1	3%	172	21	12%
0.552	141.0	6.3	4%	186	28	15%
0.588	139.7	5.0	4%	207	21	10%
0.624	134.6	3.6	3%	234	21	9%
0.661	128.4	3.7	3%	234	21	9%
0.697	126.3	13.8	11%	234	48	21%
0.733	109.7	4.6	4%	186	21	11%
0.770	110.9	7.4	7%	193	34	18%
0.806	112.0	3.9	3%	186	21	11%

Table C.10: Frequency Results for Ps = 2.110 MPa

P_b (MPa)	f_{Fb} (Hz)	$U_{f_{Fb}}$ (Hz)	$U_{f_{Fb}}$ (%)	f_{EC} (Hz)	$U_{f_{EC}}$ (Hz)	$U_{f_{EC}}$ (%)	$\%_{Diff}$ (%)
0.297	77.4	2.51	3%	77.5	4.64	6%	0.13%
0.333	68.0	1.46	2%	68.7	4.13	6%	1.03%
0.372	64.2	5.37	8%	64.7	8.34	13%	0.78%
0.406	67.5	2.04	3%	67.5	2.04	3%	0.00%
0.442	69.1	2.99	4%	68.7	2.98	4%	0.58%
0.479	68.6	2.17	3%	68.2	2.16	3%	0.58%
0.515	68.6	2.17	3%	69.4	2.18	3%	1.17%
0.552	71.0	2.33	3%	70.3	3.19	5%	0.99%
0.588	71.0	1.44	2%	70.6	1.43	2%	0.56%
0.624	69.0	2.17	3%	68.3	2.98	4%	1.01%
0.661	72.0	4.32	6%	72.3	1.52	2%	0.42%
0.697	73.2	6.89	9%	72.8	7.76	11%	0.55%
0.733	80.8	6.49	8%	81.0	2.72	3%	0.25%
0.770	83.0	4.01	5%	82.9	1.81	2%	0.12%
0.806	84.3	4.06	5%	84.3	2.76	3%	0.00%

Table C.11: Pressure Amplitude Results for Ps = 2.772 MPa

P_b (MPa)	P_{Fb} (kPa)	U_{Fb} (kPa)	U_{Fb} (%)	P_{amp} (Pa)	U_{amp} (Pa)	U_{amp} (%)
0.414	112.6	4.1	4%	97	34	35%
0.462	147.2	5.2	4%	145	21	14%
0.509	200.0	19.6	10%	234	28	12%
0.556	190.9	7.4	4%	214	21	10%
0.603	195.0	4.6	2%	221	21	10%
0.650	203.3	5.6	3%	214	28	13%
0.967	188.7	8.2	4%	228	21	9%
0.744	184.4	7.0	4%	241	21	9%
0.792	183.2	4.5	2%	269	28	10%
0.838	175.3	4.7	3%	303	28	9%
0.885	166.2	5.2	3%	303	28	9%
0.932	172.7	13.2	8%	359	21	6%
0.980	151.2	15.4	10%	296	48	16%
1.027	147.5	5.4	4%	255	21	8%
1.074	144.6	5.3	4%	248	28	11%

Table C.12: Frequency Results for Ps = 2.772 MPa

P_b (MPa)	f_{Fb} (Hz)	$U_{f_{Fb}}$ (Hz)	$U_{f_{Fb}}$ (%)	f_{EC} (Hz)	$U_{f_{EC}}$ (Hz)	$U_{f_{EC}}$ (%)	$\%_{Diff}$ (%)
0.414	75.7	1.53	2%	75.9	4.31	6%	0.26%
0.462	67.8	1.33	2%	67.1	2.04	3%	1.03%
0.509	59.6	3.39	6%	59.0	3.58	6%	1.01%
0.556	63.4	2.86	5%	63.3	1.27	2%	0.16%
0.603	67.2	2.23	3%	66.8	3.06	5%	0.60%
0.650	66.4	3.76	6%	66.8	2.97	4%	0.60%
0.967	69.8	1.41	2%	70.3	3.19	5%	0.72%
0.744	71.0	2.33	3%	71.5	3.41	5%	0.70%
0.792	71.4	1.04	1%	71.0	1.44	2%	0.56%
0.838	67.8	4.40	6%	68.1	2.13	3%	0.44%
0.885	71.0	2.33	3%	72.0	3.42	5%	1.41%
0.932	71.9	7.76	11%	70.6	2.32	3%	1.81%
0.980	78.2	5.02	6%	79.0	8.06	10%	1.02%
1.027	80.6	3.71	5%	80.5	2.72	3%	0.12%
1.074	83.1	5.45	7%	83.4	2.94	4%	0.36%

Table C.13: Pressure Amplitude Results for Ps = 3.440 MPa

P_b (MPa)	P_{Fb} (kPa)	U_{Fb} (kPa)	U_{Fb} (%)	P_{amp} (Pa)	U_{amp} (Pa)	U_{amp} (%)
0.536	144.3	5.7	4%	N/A	N/A	N/A
0.594	184.3	4.9	3%	172	21	12%
0.653	247.5	26.7	11%	283	48	17%
0.711	235.1	4.2	2%	255	28	11%
0.769	239.6	4.6	2%	248	28	11%
0.827	251.4	4.8	2%	276	28	10%
0.885	234.2	6.4	3%	262	21	8%
0.943	231.3	8.7	4%	317	34	11%
1.002	225.2	8.2	4%	345	34	10%
1.060	225.7	4.4	2%	386	34	9%
1.118	210.9	3.4	2%	400	21	5%
1.176	211.5	8.4	4%	455	28	6%
1.234	194.0	17.7	9%	359	83	23%
1.293	182.9	3.8	2%	359	28	8%
1.351	183.1	4.1	2%	338	21	6%

Table C.14: Frequency Results for Ps = 3.440 MPa

P_b (MPa)	f_{Fb} (Hz)	$U_{f_{Fb}}$ (Hz)	$U_{f_{Fb}}$ (%)	f_{EC} (Hz)	$U_{f_{EC}}$ (Hz)	$U_{f_{EC}}$ (%)	$\%_{Diff}$ (%)
0.536	76.2	3.70	5%	N/A	N/A	N/A	N/A
0.594	68.2	1.34	2%	68.3	2.98	4%	0.15%
0.653	62.0	5.36	9%	61.7	6.72	11%	0.48%
0.711	65.0	2.09	3%	65.5	4.11	6%	0.77%
0.769	68.5	1.47	2%	67.2	4.12	6%	1.90%
0.827	65.5	3.86	6%	66.4	2.03	3%	1.37%
0.885	70.7	3.19	5%	70.7	5.66	8%	0.00%
0.943	70.3	4.03	6%	70.2	1.42	2%	0.14%
1.002	71.0	2.33	3%	70.2	1.42	2%	1.13%
1.060	68.4	4.82	7%	67.6	3.26	5%	1.17%
1.118	70.8	4.31	6%	70.2	1.42	2%	0.85%
1.176	71.5	2.33	3%	71.9	3.42	5%	0.56%
1.234	76.5	5.96	8%	76.3	8.56	11%	0.26%
1.293	81.6	5.03	6%	80.6	3.71	5%	1.23%
1.351	83.4	2.94	4%	81.9	2.92	4%	1.80%

Vita Auctoris

NAME: Christopher Peirone

PLACE OF BIRTH: Windsor, Ontario, Canada

YEAR OF BIRTH: 1986

EDUCATION:

St. Clair College, Windsor, Ontario
2010-2013 Mechanical Engineering Technology – Automotive Product Design

University of Windsor, Windsor, Ontario
2013-2016 B.A.Sc.

University of Windsor, Windsor, Ontario
2016-2019 M.A.Sc.